**NOAA NESDIS
CENTER for SATELLITE APPLICATIONS and RESEARCH**

ALGORITHM THEORETICAL BASIS DOCUMENT

JPSS Enterprise Processing System Aerosol Detection Product

Pubu Ciren and Shobha Kondragunta

NOAA/NESDIS/STAR

Version 1.5
April 7, 2022

TABLE OF CONTENTS

LIST OF TABLES

LIST OF FIGURES

LIST OF ACRONYMS

Acronym/ Abbreviation	Definition
AAA	Aerosol, Air Quality, and Atmospheric Chemistry
AERONET	**AE**rosol **RO**botic **NET**work
ADP	Aerosol Detection Product
AAI	Absorbing Aerosol Index
AIT	Aerosol Integration Team
AOD	Aerosol Optical Depth
ATBD	Algorithm Theoretical Basis Document
ATIP	Algorithm and Test Implementation Plan
AVHRR	Advanced Very High Resolution Radiometer
AWG	Algorithm Working Group
BT	Brightness Temperature
BTD	Brightness Temperature Difference
CALIOP	Cloud-Aerosol Lidar with Orthogonal Polarization
CALIPSO	Cloud-Aerosol Lidar and Infrared Pathfinder Satellite Observation
CONUS	Continental United States
CRTM	Community Radiative Transfer Model
DSDI	Dust Smoke Discrimination Index
ECM	Enterprise Cloud Mask
EPS	Enterprise Processing System
FMW	Fine Mode Weight
F&PS	Functional and Performance Specification Document
GOES	Geostationary Operational Environmental Satellite
HIRS	Hyperspectral Infrared Sounder
HMS	Hazard Mapping System
IMS	Interactive Multisensor Snow and Ice Mapping System
IR	Infrared
JPSS	Joint Polar-orbiting Satellite Series
LHP	Loop Heat Pipe
LZA	Local Zenith Angle
MeanR	Mean of reflectance (in a box of 3 x 3 pixels)
MODIS	Moderate Resolution Imaging Spectroradiometer
MRD	Mission Requirements Document
NDVI	Normalized Difference Vegetation Index
NOAA	National Oceanic and Atmospheric Administration
R	Reflectance
RGB	True Color Imagery (Red-Green-Blue)
RTM	Radiative Transfer Model
SAAI	Scaled Absorbing Aerosol Index
SNPP	Suomi- National Polar-orbiting Partnership
SZA	Solar Zenith Angle
TOA	Top of the Atmosphere
VFM	Vertical Feature Mask
VIIRS	Visible Infrared Imaging Radiometer Suite
VZA	(Satellite) View Zenith Angle
UW	University of Wisconsin

ABSTRACT

This document describes the algorithm for Aerosol Detection Product (ADP) (including smoke/dust detection) over land and water from the multispectral reflectance measurements observed by the Visible Infrared Imaging Radiometer Suite (VIIRS) onboard JPSS satellites. It includes the description of theoretical basis, physics of the problem, validation of the product, and assumptions and limitations.

Episodic events, such as smoke and dust outbreaks, impact human health and economy. Therefore, it is desirable to have information on the time, location and coverage of these outbreaks for the monitoring and forecasting of air quality. JPSS VIIRS is designed to observe the globe with a spatial resolution of 750m at nadir in the visible, near-IR, and IR bands respectively. Taking advantage of the unique capability of JPSS VIIRS, ADP will be produced with an algorithm designed to take advantage of various spectral measurements.

The aerosol detection algorithm is based on the fact that smoke/dust exhibits features of spectral dependence and contrast over both the visible and infrared spectrums that are different from clouds, surface, and clear-sky atmosphere. The fundamental principle of the aerosol detection algorithm depends on threshold tests which separate smoke/dust from cloud and clear-sky over water and land.

By using Suomi National Polar-orbiting Partnership (SNPP) VIIRS observations as a proxy, the JPSS VIIRS EPS ADP algorithm has been tested for different scenarios such as wildfires, dust storms, and dust transport from Africa. Comparisons with RGB images, AERONET observations and other satellite products such as CALIPSO/CALIOP (Cloud-Aerosol Lidar and Infrared Pathfinder Satellite Observation/Cloud-Aerosol Lidar with Orthogonal Polarization) have been performed. In general, the algorithm requirements, i.e., 80% correct detection for dust over water and land, for smoke over land, and 70% correct detection for smoke over water, can be achieved.

1 INTRODUCTION

Aerosols perturb the Earth's energy budget by scattering and absorbing radiation and by altering cloud properties and lifetimes. They also exert large influences on weather, air quality, hydrological cycles, and ecosystems. Aerosols released into the atmosphere due to natural and anthropogenic activities lead to deteriorated air quality and affect Earth's climate. It is important to regularly monitor global aerosol distributions and study how they are changing, especially for those aerosols with large spatial and temporal variability, such as smoke, sand storms, and dust [IPCC, 2007]. Detection of these highly variable aerosols is challenging because of strong interactions with local surface and meteorological conditions.

Because atmospheric aerosols can directly alter solar and Earth radiation in both visible and infrared (IR) spectral regions through scattering and absorption processes, both visible, including deep-blue, and IR remote sensing techniques have been used for detection of aerosols in the atmosphere [e.g., Tanre and Legrand, 1991; Ackerman 1989, 1997; Kaufman et al., 1997; Verge-Depre et al., 2006; Ciren and Kondragunta, 2014]. Visible and IR images can be used for detecting episodic smoke and dust particles due to the fact that these aerosol particles display their distinctive spectral variations in the visible and IR spectral regions differently from those of cloud or clear-sky conditions. In practice, detection is based on the analysis of reflectance (or radiance) in visible bands or brightness temperature (BT) in IR bands. The magnitude of the difference in reflectance or BT in selected bands (or channels) can be used to infer the signature of dust and smoke. This is the basic idea of the IR-Visible path of our aerosol detection algorithm. In addition, smoke and dust, as absorbing aerosols, have significantly increasing absorptions with the decreasing wavelength in the short end of visible spectrum, such as the deep-blue region. This feature enables us to detect the presence of smoke/dust as a whole. Then, further separation between smoke and dust can be achieved by using observations from the shortwave-IR, owing the large difference in their particle size. This approach is used for the deep-blue path our aerosol detection algorithm. Both paths will be described in detail in this document.

1.1 Purpose of This Document

The aerosol detection Algorithm Theoretical Basis Document (ATBD) provides a high-level description of and the physical basis for the detection of smoke/dust contaminated pixels with images taken by the VIIRS flown on the JPSS series of next generation NOAA operational polar-orbiting meteorological satellites.   The algorithm provides an initial estimate of the presence or absence of smoke or dust within each VIIRS pixel.

1.2 Who Should Use This Document

The intended users of this document are those interested in understanding the physical basis of the algorithms and how to use the output of this algorithm to optimize the episodic aerosol detection for a particular application. This document also provides information useful to anyone maintaining or modifying the original algorithm.

1.3 Inside Each Section

This document is broken down into the following main sections.

- **System Overview**: Provides relevant details on VIIRS instrument characteristics and a detailed description of the products generated by the algorithm.

- **Algorithm Description**: Provides a detailed description of the algorithm including the physical basis, the required input, and the derived output. Examples from algorithm processing using proxy input data are also provided.

- **Test Data Sets and Outputs**: Provides a description of the test data sets used to characterize the performance of the algorithm and the quality of the output. Precision and accuracy of the end product is estimated and an error budget is calculated.

- **Practical Considerations**: Provides an overview of the issues involving numerical computation, programming and procedures, quality assessment and diagnostics and exception handling.

- **Assumptions and Limitations**: Provides an overview of the assumptions that the algorithm is based on and the current limitations of the approach. The plan for overcoming some limitations with further algorithm development is also given.

1.4 Related Documents

Besides the references given throughout, this document is related to documents listed as below:

(1) JPSS Program Level 1 Requirements Document (L1RD)
(2) JPSS Program Level 1 Requirements Document SUPPLEMENT (L1RDS)
(3) JPSS VIIRS Aerosol Detection Product Validation Plan Document

1.5 Revision History

This is the fourth version (Version 1.5) of this document. All the documents were created by the JPSS Risk Reduction ADP team led by Dr. Shobha Kondragunta of NOAA/NESDIS/STAR. The ADP team includes Dr. Pubu Ciren of IMSG, Inc., Maryland. Version 1.5 ATBD accompanies the delivery of the version 1.5 algorithm to the JPSS Risk Reduction Algorithm Integration Team (AIT). Version 1.1 is an update to Version 1.0 to include a detailed description on the Enterprise System of the JPSS Risk Reduction algorithm, as described in Version 1.3, and also some corrections. Version 1.2 includes some corrections to Version 1.1 to ensure the consistency between the algorithm code and ATBD. Version 1.3 includes some revisions of thresholds and confidence level determinations in Version 1.2 to ensure consistency between the algorithm code and ATBD. Version 1.4 includes some extra tests to remove false smoke detection over dry /river and lake beds and revisions of thresholds in Version 1.3 to ensure improved smoke and dust detection over land.

2 OBSERVING SYSTEM OVERVIEW

This section will describe the products generated by the JPSS EPS ADP algorithm including smoke and dust and the requirements it places on the sensor.

2.1 Products Generated

Table 1. JPSS mission requirements for Aerosol Detection Product

EDR Attribute	Threshold	Objective
ADP Applicable Conditions: 1. **ADP includes dust, volcanic ash, and smoke at any altitude.** 2. **Clear, for AOD greater than 0.2 daytime only.**		
Horizontal Cell Size	3 km	1 km
a. **Vertical Cell Size**	Total Column	0.2 km
b. **Mapping Uncertainty, 3 Sigma**	3 km	0.1 km
c. **Measurement Range**		
d. **Detect aerosols (dust, smoke, volcanic ash) (1)(2)**	Type: dust, volcanic ash, smoke	Dust, ash, smoke, sea salt
1. **Radioactive/smoke plumes**	0 to 150 µg/m^3 (smoke)	0 to 200 µg/m^3 (smoke)
2. **Probability of Correct Typing**		
e. **Aerosol Detection**	80%	100%
1. **Dust**	80%	100%
2. **Smoke**	70%	100%
3. **Volcanic Ash**	60%	100%
4. **Mixed Aerosol (2)**		80%
5.		
f. **Refresh**	At least 90% coverage (product retrieval is attempted regardless of sky condition) of the globe over 24 hours (monthly average)	3 hrs.

Notes:
1. The dust and volcanic ash categories were combined at the request of M. Pavalonis and supported by J. Gleason and H. Kilcoyne.   The current algorithm cannot distinguish between dust and volcanic ash and the intent of the EDR was to say that there was "something" in the atmosphere. The dust and volcanic ash are separated into two categories in this revision. Although some dust may be falsely identified as ash by the volcanic ash algorithm, the suspended matter algorithm will identify dust explicitly.
2. DOC has a responsibility for analyzing areas of volcanic ash, blowing dust, and smoke. There is therefore a requirement that the aerosol detection algorithm identifies instances of multiple types of aerosols at the same location and not merely provide a single aerosol type with the highest concentration or probability.

As described in Table 1, ADP measurement accuracy is defined as 80% of correct classification for dust over water and land, for smoke over land, and 70% correct classification for smoke over water with measurement range given as binary yes/no detection above a threshold of 0.2 aerosol optical depth, as stated in the JPSS Program Level 1 Requirements Document (L1RD) and JPSS Program Level 1 Requirements SUPPLEMENT (L1RDS). It should be noted that aerosol optical depth of 0.2 defines background atmospheric aerosol and is not computed within this algorithm or imported from the Aerosol Optical Depth (AOD) algorithm.

The purpose of the EPS ADP algorithm is to identify VIIRS pixels which are contaminated by either smoke or dust during daytime to facilitate the monitoring of occurrences and development of smoke/dust episodes. However, due to the relatively weak contribution of aerosols compared to reflection from the surface to the measured reflectances/brightness temperatures, the EPS ADP algorithm performs better for heavy smoke /dust episodes (with aerosol optical depth >0.2) over dark surfaces than over bright surfaces. Smoke detection over semi-arid and arid regions is less accurate due to lower contrast with the background.

The EPS ADP algorithm output is written in netCDF4 format. At the pixel level, there are 6 aerosol type flags (1/0 for yes/no): volcanic ash (passed down from volcanic ash product, currently), dust, smoke, cloud, none/unknown/clear, and snow/ice. All of the variables output from the EPS ADP algorithm are listed in Table 2. Details about the quality flags are listed in Table 3. In addition, diagnostic bit-wise flags are also generated, as listed in Tables 4-7.

2.2 Instrument Characteristics

The ADP will be produced for each VIIRS pixel. Table 6 summarizes the channels used by the current EPS ADP algorithm. Note that the EPS ADP algorithm is designed as an Enterprise System, which means the EPS ADP algorithm is able to handle multi-spectral observations from sensors which cover the wavelength range from deep-blue to IR, such as VIIRS and MODIS, or from visible to IR, such as AHI and ABI. In the following sections, VIIRS will be mainly used as an example. However, the mapping of channels or bands from different sensors to the channels used in the enterprise system algorithm is given in Table 8.

The backbone of the EPS ADP algorithm is the distinctive spectral and spatial signature of aerosol (smoke/dust). Like any other threshold-based algorithm, the EPS ADP algorithm requires optimal performance of the instrument. First, the EPS ADP algorithm is designed to work when only a sub-set of the expected channels are available. Missing channels, especially the crucial ones, will directly impact the performance of the algorithm. Second, the EPS ADP algorithm is sensitive to instrument noise and calibration error. Thresholds are required to be adjusted according to the status of instrument operation and performance. Third, calibrated observations are also critical, but since the algorithm does not compare the observed values to those from a forward radiative transfer model, uncertainties in calibration can be ameliorated by modifying thresholds post launch. The channel specifications for VIIRS are given in the Mission Requirements Document (MRD).

Table 2. Variables output from the EPS ADP algorithm.

Variable	Type	Description	Dim	Units	Range
Ash	Byte	Volcanic Ash Flag: 1 = yes, 0 = No	2	1	0,1
AshConfidHighPct	Float	Percent of high confidence ash	0	Percent	0, 100
AshConfidLowPct	Float	Percent of low confidence ash	0	Percent	0, 100
AshConfidMediumPct	Float	Percent of medium confidence ash	0	Percent	0, 100
AshPct	Float	Percent of good ash retrieval	0	Percent	0, 100
QC_Flag	Byte	Quality Flag for Ash, Smoke, Dust and NUC (see Table 3)	2	1	-128,127
PQI1	Byte	Product Quality Information (see Table 4)	2	1	-128,127
PQI2	Byte	Product Quality Information (see Table 5)	2	1	-128,127
PQI3	Byte	Product Quality Information (see Table 6)	2	1	-128,127
PQI4	Byte	Product Quality Information (see Table 7)	2	1	-128,127
Cloud	Byte	Cloud Flag: 1 = yes, 0 = no	2	1	0,1
SAAI	Float	Scaled Absorbing Aerosol Index	2	1	
Dust	Byte	Dust flag: 1 = yes, 0 = no	2	1	0,1
DustConfidHighPct	Float	Percent of high confidence dust	0	Percent	0, 100
DustConfidLowPct	Float	Percent of low confidence dust	0	Percent	0, 100
DustConfidMediumPct	Float	Percent of medium confidence dust	0	Percent	0, 100
DustPct	Float	Percent of good dust retrieval	0	Percent	0, 100
Latitude	Float	Pixel latitude in field latitude	2	° North	-90, 90
Longitude	Float	Pixel longitude in field longitude	2	° East	-180, 180
DSDI	Float	Dust Smoke Discrimination Index	2	1	
NUC	Byte	None, Unknown, Clear sky Flag: 1 = yes, 0 = no	2	1	0, 1
NUCConfidHighPct	Float	Percent of high confidence NUC	0	Percent	0, 100
NUCConfidLowPct	Float	Percent of low confidence NUC	0	Percent	0, 100
NUCConfidMediumPct	Float	Percent of medium confidence NUC	0	Percent	0, 100
NUCPct	Float	Percent of good NUC retrieval	0	Percent	0, 100
NoAshPct	Float	Percent of ash not determined (bad)	0	Percent	0, 100
NoDustPct	Float	Percent of dust not determined (bad)	0	Percent	0, 100
NoNUCPct	Float	Percent of NUC not determined (bad)	0	Percent	0, 100
NoSmokePct	Float	Percent of smoke not determined (bad)	0	Percent	0, 100
NumOfGoodAshRetrieval	Long	Number of Good Ash Retrievals	0	1	
NumOfGoodDustRetrieval	Long	Number of Good Dust Retrievals	0	1	
NumOfGoodNUCRetrieval	Long	Number of Good NUC Retrievals	0	1	
NumOfGoodSmokeRetrieval	Long	Number of Good Smoke Retrievals	0	1	
NumOfQualityFlag	Long	Number of quality flags	0	1	
NumOfSatZenAngLess60	Long	Number of pixels with satellite zenith angle < 60 degree	0	1	

Variable	Type	Description	Dim	Units	Range
NumOfSolZenAngLess60	Long	Number of pixels with solar zenith angle < 60 degree	0	1	
Smoke	Byte	Smoke Flag: 1 = yes, 0 = no	2	1	0, 1
SmokeCon	Float	Smoke Concentration	2	$\mu g/m^3$	
SmokeConfidHighPct	Float	Percent of high confidence smoke	0	Percent	0, 100
SmokeConfidLowPct	Float	Percent of low confidence smoke	0	Percent	0, 100
SmokeConfidMediumPct	Float	Percent of medium confidence smoke	0	Percent	0, 100
SmokePct	Float	Percent of good smoke retrieval	0	Percent	0, 100
SnowIce	Byte	Snow Ice Flag: 1 = yes, 0 = no	2	1	0, 1
StartColumn	Long	Start column index	0		
StartRow	Long	Start row index	0		
TotalPixel	Long	Total number of pixels where retrievals are attempted	0	1	

Table 3. Definitions of bit-wise quality flags for the EPS ADP "QC_Flag" variable.

Bit*	Quality Flag Name	Meaning (2-bits)			
		01	10	00	11**
0-1	QC_ASH_CONFIDENCE	Low quality	Medium quality	High quality	Bad/missing
2-3	QC_SMOKE_CONFIDENCE				
4-5	QC_DUST_CONFIDENCE				
6-7	QC_NUC_CONFIDENCE				

*Start from the least significant bit
**Bad data due to bad input data or missing due to missing observations

Table 4. Definitions of bit-wise diagnostic flags for the EPS ADP "PQI1" variable.

Bit*	Diagnostic Flag Name	Meaning			
		1-bit	0 (default)	1	-----
		2-bits	00 (default)	01	11
0	QC_INPUT_LON	1-bit	Valid longitude	Invalid longitude (longitude > 180 or < -180)	-----
1	QC_INPUT_LAT	1-bit	Valid latitude	Invalid latitude (latitude > 90 or < -90)	-----
2-3	QC_INPUT_SOLZEN	2-bits	Valid solar zenith angle (SZA) (0 ≤ SZA ≤ 90)	Invalid SZA (SZA > 90 or < 0)	90 ≥ SZA > 60

Bit			Valid local zenith angle (VZA) (0 ≤ VZA ≤ 90)	Invalid VZA (VZA > 90 or < 0)	90 ≥ VZA > 60
4-5	QC_INPUT_SATZEN	2-bits	Valid local zenith angle (VZA) (0 ≤ VZA ≤ 90)	Invalid VZA (VZA > 90 or < 0)	90 ≥ VZA > 60
6-7	QC_INPUT_SNOW/ICE_SOURCE	2-bits	VIIRS snow/ice mask	IMS snow/ice mask	Internal snow/ice mask

*Start from the least significant bit

Table 5. Definitions of bit-wise diagnostic flags for the EPS ADP "PQI2" variable.

Bit*	Diagnostic Flag Name	Meaning (1-bit)	
		0 (default)	1
0	QC_INPUT_SUNGLINT_SOURCE	VIIRS sun glint mask (from Cloud Mask product)	Internal sun glint mask
1	QC_INPUT_SUNGLINT	Outside of sun glint	Within sun glint
2	QC_INPUT_LAND/WATER	Water	Land
3	QC_INPUT_DAY/NIGHT	Day	Night
4	QC_WATER_SMOKE_INPUT	Valid VIIRS inputs	Invalid VIIRS inputs
5	QC_WATER_SMOKE_CLOUD	Cloud-free	Obscured by clouds
6	QC_WATER_SMOKE_SNOW/ICE	Snow/ice free	With snow/ice
7	QC_WATER_SMOKE_TYPE (only for IR/Visible algorithm path)	Thin Smoke	Thick Smoke

*Start from the least significant bit

Table 6. Definitions of bit-wise diagnostic flags for the EPS ADP "PQI3" variable.

Bit*	Diagnostic Flag Name	Meaning (1-bit)	
		0 (default)	1
0	QC_WATER_DUST_INPUT	Valid VIIRS inputs	Invalid VIIRS inputs
1	QC_WATER_DUST_CLOUD	Cloud-free	Obscured by clouds
2	QC_WATER_DUST_SNOW/ICE	Snow/ice free	With snow/ice
3	QC_WATER_DUST_TYPE (only for IR/Visible algorithm path)	Thin dust	Thick dust
4	QC_LAND_SMOKE_INPUT	Invalid VIIRS inputs	Valid VIIRS inputs
5	QC_LAND_SMOKE_CLOUD	Cloud-free	Obscured by clouds
6	QC_LAND_SMOKE_SNOW/ICE	Snow/ice free	With snow/ice

Bit*	Diagnostic Flag Name			
7	QC_LAND_SMOKE_TYPE (only for IR/Visible algorithm path)	Fire		Thick smoke

*Start from the least significant bit

Table 7. Definitions of bit-wise diagnostic flags for the EPS ADP "PQI4" variable.

Bit*	Diagnostic Flag Name		Meaning			
		1-bit	0 (default)	1	-----	-----
		2-bits	00 (default)	10	01	11
0	QC_LAND_DUST_INPUT	1-bit	Valid VIIRS inputs	Invalid VIIRS inputs	-----	-----
1	QC_LAND_DUST_CLOUD	1-bit	Cloud-free	Obscured by clouds	-----	-----
2	QC_LAND_DUST_SNOW/ICE	1-bit	Snow/ice free	With snow/ice	-----	-----
3	QC_LAND_DUST_TYPE (only for IR/Visible algorithm path)	1-bit	Thin dust	Thick dust	-----	-----
4-5	Smoke_Detection_Algorithm_Path	2-bits	Deep-blue	Missing	IR-Visible	Both
6-7	Dust_Detection_Algorithm_Path	2-bits				

*Start from the least significant bit

Table 8. Channel numbers and wavelengths for the VIIRS. Usage of Channels in the EPS ADP algorithm are given in last column.

Band Name	Nominal Wavelength Range (µm)	Nominal Central Wavelength (µm)	Horizontal Sample Interval (Km) (Along-Track×Along-Scan)		Sample Use
			Nadir	End of Scan	
M1	0.402-0.422	0.412	0.742×0.259	1.60×1.58	Dust/Smoke
M2	0.436-0.454	0.445	0.742×0.259	1.60×1.58	Dust/smoke
M3	0.478-0.498	0.488	0.742×0.259	1.60×1.58	Dust/Smoke
M4	0.545-0.565	0.555	0.742×0.259	1.60×1.58	Smoke
M5	0.662-0.682	0.640	0.742×0.259	1.60×1.58	Dust/Smoke
M6	0.739 – 0.754	0.746	0.742×0.776	1.60×1.58	Smoke
M7	0.846-0.885	0.865	0.742×0.259	1.60×1.58	Dust/Smoke
M8	1.230-1.250	1.24	0.742×0.776	1.60×1.58	Dust/Smoke
M9	1.371-1.386	1.378	0.742×0.776	1.60×1.58	Dust
M10	1.580-1.640	1.61	0.742×0.776	1.60×1.58	Smoke
M11	2.225-2.275	2.25	0.742×0.776	1.60×1.58	Dust/Smoke

M12	3.660-3.840	3.70	0.742×0.776	1.60×1.58	Dust/Smoke
M13	3.973-4.128	4.05	0.742×0.259	1.60×1.58	Smoke
M14	8.400-8.700	8.55	0.742×0.776	1.60×1.58	
M15	10.263-11.263	10.763	0.742×0.776	1.60×1.58	Dust/Smoke
M16	11.538-12.488	12.013	0.742×0.776	1.60×1.58	Dust

Table 9 Mapping of channels for different sensors to channels used in ADP Enterprise Processing System.

Channel in EPS		Use in Algorithm Path	Sensor Bands			
Number	Wavelength (μm)		VIIRS	MODIS	ABI	AHI
1	0.412	Deep-Blue	M1	8	**	**
2	0.445	Deep-Blue	M2	9	**	**
3	0.488	Deep-Blue and IR-Visible	M3	3	1	1
4	0.555	Deep-Blue	M4	4	(2)*	2
5	0.640	Deep-Blue and IR-Visible	M5	1	2	3
6	0.746	Deep-Blue	M6	15	**	**
7	0.865	Deep-Blue and IR-Visible	M7	2	3	4
8	1.24	Deep-Blue	M8	5	(5)*	(5)*
9	1.38	IR-Visible	M9	26	4	(5)*
10	1.61	IR-Visible	M10	6	5	5
11	2.25	Deep-Blue and IR-Visible	M11	7	6	6
12	3.70	IR-Visible	M12	20	(7)*	(7)*
13	4.05	IR-Visible	M13	21	7	7
14	10.35	IR-Visible	(M15)*	(31)*	13	13
15	11.2	IR-Visible	M15	31	14	14
16	12.01	IR-Visible	M16	32	15	15

* Sensor band missing for given wavelength; band in parentheses is substituted.
** Sensor band missing but not required for a given algorithm path, and filled with '-999.9' in order to run EPS ADP algorithm.

3 ALGORITHM DESCRIPTION

3.1 Algorithm Overview

The ADP serves to aid air quality forecasters in identifying smoke and dust laden atmospheres. The EPS ADP algorithm follows heritage algorithms:

- Non-cloud obstruction (including smoke and dust) detection in the MOD/MYD35 MODIS cloud mask developed for MODIS by the University of Wisconsin (UW).
- Operational dust detection from MODIS developed for NWS and run by NESDIS/OSPO.

The fundamental outputs of the ADP consist of 10 flags. They are 6 type flags, respectively for the presence of volcanic ash, smoke, dust, none/unknown/clear, clouds and snow/ice, and 4 quality flags, respectively for volcanic ash flag, smoke flag, dust flag and none/unknown/clear flag. The type flag has a value of 1 for the presence and 0 for the absence. As an example, in the smoke/dust flag, 1 represents smoke/dust and 0 represents no smoke/dust, respectively. The details on quality flags are given in section 2.1. The following sections describe the JPSS VIIRS EPS ADP algorithm.

3.2 Processing Outline

The processing outline of the EPS ADP algorithm is summarized in Figure 1, which includes the basic modules as input, output, and detection over land and water. The algorithm is written in C++, and products are outputted in netCDF4 format. For optimizing CPU usage, the EPS ADP algorithm is designed to run on segments of data. Each segment is comprised of multiple scan lines (12 lines). The ADP EPS algorithm is able to run through three paths: IR-visible based detection algorithm, defined as path **1**, deep-blue based detection algorithm, defined as path **2,** and combined IR-Visible based and deep-based detection algorithms, defined as Path **3.** The algorithm path is supplied or determined by the spectral coverage of the input data. The algorithm path taken to generate the product is outputted in the product quality information flags (see **Table 2**, PQI4 and details in **Table 7**), respectively for the detected smoke and dust**.**
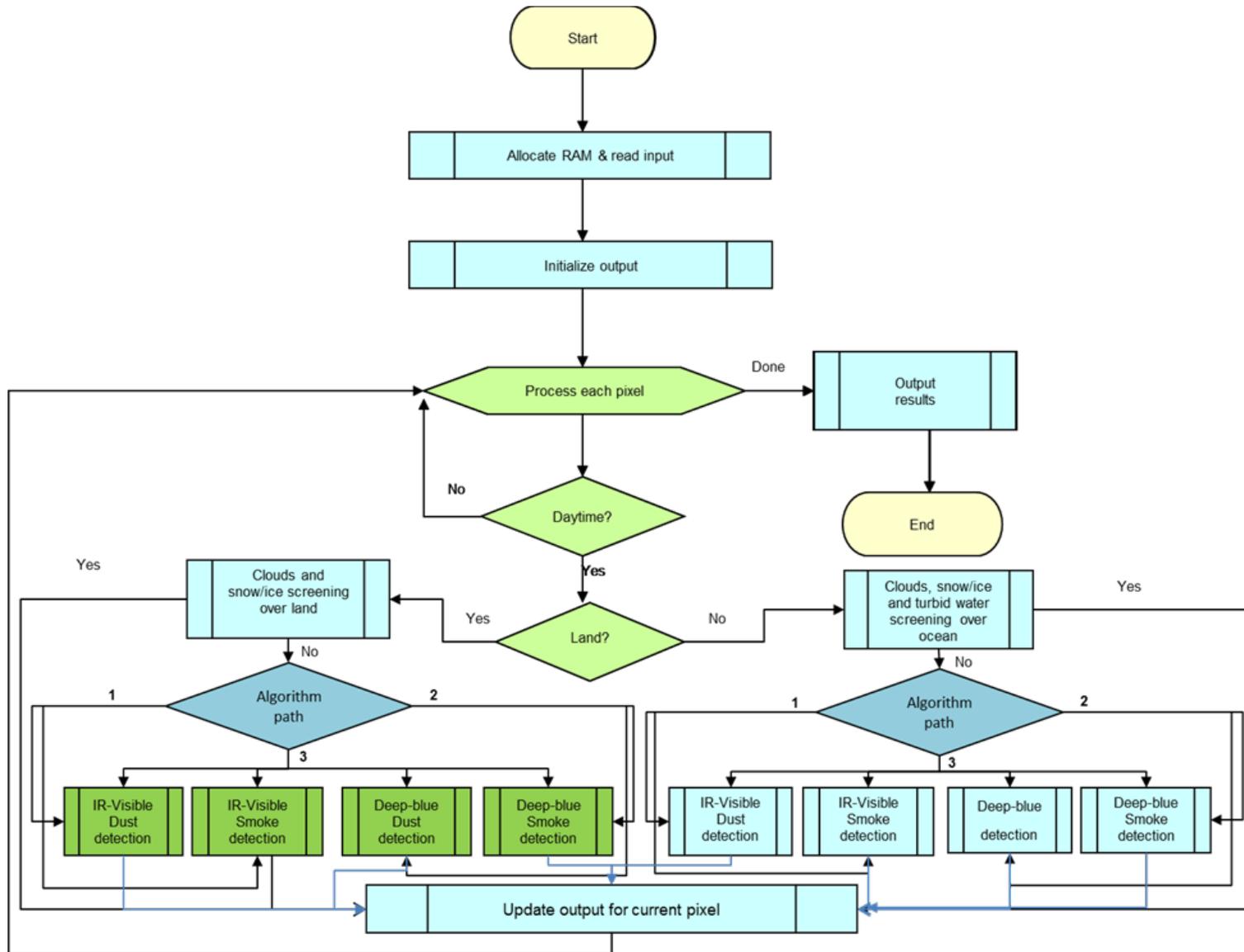
Figure 1: High level flowchart of the EPS ADP algorithm, illustrating the main processing sections.

3.3 Algorithm Input

This section describes the input needed to process the EPS ADP algorithm. While the ADP is derived for each pixel, it does require knowledge of the surrounding pixels. In its current operation, we run the EPS ADP algorithm on segments of 12 scan-lines.

3.3.1 Primary Sensor Data

Calibrated/Navigated VIIRS reflectances and brightness temperatures on selected channels, geolocation (latitude/longitude) information, and VIIRS sensor quality flags are used as the sensor input data for the algorithm. Table 8 contains the primary sensor data used by the EPS ADP algorithm. Note that the cloud mask required in the EPS ADP algorithm is designed to primarily come from the JPSS VIIRS cloud product. Channels used to determine the cloud mask are not listed here as that information is part of the VIIRS cloud mask ATBD.

Table 10   ADP primary sensor input data.

Name	Type	Description	Dimension
M1 reflectance	input	Calibrated VIIRS level 1b reflectance at M 1	grid (xsize, ysize)
M2 reflectance	input	Calibrated VIIRS level 1b reflectance at M 2	grid (xsize, ysize)
M3 reflectance	input	Calibrated VIIRS level 1b reflectance at M 3	grid (xsize, ysize)
M4 reflectance	input	Calibrated VIIRS level 1b reflectance at M 4	grid (xsize, ysize)
M5 reflectance	input	Calibrated VIIRS level 1b reflectance at M 5	grid (xsize, ysize)
M6 reflectance	input	Calibrated VIIRS level 1b reflectance at M 6	grid (xsize, ysize)
M7 reflectance	input	Calibrated VIIRS level 1b reflectance at M 7	grid (xsize, ysize)
M8 reflectance	input	Calibrated VIIRS level 1b reflectance at M 8	grid (xsize, ysize)
M9 reflectance	input	Calibrated VIIRS level 1b reflectance at M 9	grid (xsize, ysize)
M10 reflectance	input	Calibrated VIIRS level 1b reflectance at M 10	grid (xsize, ysize)
M11 reflectance	input	Calibrated VIIRS level 1b reflectance at M 11	grid (xsize, ysize)
M12 brightness temperature	input	Calibrated VIIRS level 1b brightness temperature at M12	grid (xsize, ysize)
M 13 brightness temperature	input	Calibrated VIIRS level 1b brightness temperature at M13	grid (xsize, ysize)
M15 brightness temperature	input	Calibrated VIIRS level 1b brightness temperature at M15	grid (xsize, ysize)
M16 brightness temperature	input	Calibrated VIIRS level 1b brightness temperature at M16	grid (xsize, ysize)
Solar zenith angle	input	Pixel solar zenith angle	grid (xsize, ysize)
Solar azimuth angle	input	Pixel solar azimuth angle	grid (xsize, ysize)
Satellite zenith angle	input	Pixel satellite zenith angle	grid (xsize, ysize)
Satellite azimuth angle	input	Pixel satellite azimuth angle	grid (xsize, ysize)
Latitude	input	Pixel latitude	grid (xsize, ysize)
Longitude	input	Pixel longitude	grid (xsize, ysize)
QC flags	input	VIIRS quality control flags with level 1b data	grid (xsize, ysize)

3.3.2 VIIRS Product Precedence and Ancillary Data

The dynamic data needed by the EPS ADP algorithm are from both VIIRS Level-1b and Level-2 products and are listed in Table 11. They include the cloud mask from the VIIRS cloud product and the snow/ice mask from the VIIRS level-2 product. The sunglint mask and day/night flag are determined internally in the EPS ADP algorithm from viewing and illuminating geometry information.

Table 11   JPSS VIIRS Product Precedence and Ancillary input data.

	Name	Type	Source	Dimension
VIIRS Product Precedence Data	Cloud mask	input	JPSS VIIRS level 2 cloud product	grid (xsize, ysize)
	Snow/Ice mask	input	JPSS VIIRS level 2 Snow/Ice Product	grid(xsize, ysize)
	Volcanic ash	input	JPSS VIIRS level 2 Volcanic ash Product	grid(xsize, ysize)
	Sun glint mask	input	Internally determined but needs information on viewing geometry	grid(xsize, ysize)
	Day/night flag	input	Internally determined but needs information on viewing geometry	grid(xsize, ysize)
Ancillary Data	Land/Water mask	Input	1 km dataset http://glcf.umiacs.umd.edu/data/landcover	grid(xsize,ysize)
	Snow/ice mask	Input	Interactive Multisensor Snow and Ice Mapping System (IMS) (http://nsidc.org/data/g02156.html) snow/ice mask	grid(xsize,ysize)

- **Snow/Ice mask**

The primary source of snow/ice is the VIIRS Level-2 Snow/Ice Product. However, in the event that the primary source is missing, Interactive Multisensor Snow and Ice Mapping System (IMS) (http://nsidc.org/data/g02156.html) snow/ice mask will be the secondary source.   In addition, the EPS ADP algorithm has an internal snow/ice test over land and internal sea ice test over water, whose function is to eliminate the residuals from the external snow/ice mask over land and water. It is applied after the primary/secondary snow/ice mask. Details on the internal snow/ice and sea ice mask are given in section 3.4.2.1. and 3.4.2.3.

- **Cloud mask**

The cloud mask is used in the EPS ADP algorithm to eliminate pixels with obvious clouds, such as high clouds or ice clouds, before performing smoke/dust detection. Hence, the cloud mask requirement of the EPS ADP algorithm is more specific than just determining cloudy or clear pixels. A stringent cloud mask has the potential to classify smoke/dust as cloud, while a relaxed cloud mask increases the chance of misidentifying clouds as smoke/dust. The EPS ADP algorithm uses only individual tests, which exist as a diagnostic cloud mask, such as "CloudMaskpacked" in both the JPSS Enterprise Cloud Mask (ECM) and baseline cloud mask. The JPSS cloud mask product indicates the existence of high clouds, ice

clouds, and thin cirrus clouds. In addition, some tests in the cloud mask product, such as cloud shadow and fire hot spot, are used as quality controls for the detected smoke/dust in the ADP. In addition, the flag for volcanic ash from the JPSS L-2 Volcanic ash product is used to set the volcanic ash flag in ADP output. Currently, the EPS ADP algorithm is using Suomi NPP VIIRS data as a proxy, including the SNPP VIIRS Enterprise Cloud Mask (ECM). Based on the definition of individual tests from ECM, Table 12 maps the cloud tests in ECM to individual tests in other cloud mask products, such as the Suomi NPP VIIRS Cloud mask (VCM) and MODIS cloud mask.

- **Sun glint mask**

The EPS ADP algorithm is designed to generate an internal sun glint mask based on ABI viewing and illuminating angles as a second source. The sun glint angle (η) is calculated as follows:

$$\cos(\eta) = \cos(\theta_0) \cdot \cos(\theta) + \sin(\theta_0) \cdot \sin(\theta) \cdot \cos(180 - \varphi)$$

Where θ_0 is the solar zenith angle; θ is the satellite zenith angle; and φ is defined as the difference between satellite azimuth angle and solar azimuth angle. An area with the calculated sun glint angle greater than zero and less than 40° is defined as the sun glint area.

- **Day/night mask**

A day/night flag is determined internally based upon the solar zenith angle. Day is defined as solar zenith angle of less than or equal to 87º, while night is defined as solar zenith angle greater than 87º.

- **Land/water mask**

The only static input data required by the EPS ADP algorithm is a global 1km land/water mask. The global land cover classification collection created by The University of Maryland Department of Geography with imagery from the AVHRR satellites acquired between 1981 and 1994 [Hansen et al., 1998] is the source (http://glcf.umiacs.umd.edu/data/landcover/).

Table 12 Mapping of EPS ADP cloud tests with different cloud mask products

Cloud tests names in EPS ADP algorithm	MODIS CLOUD MASK Byte No. (Bit no.)	Suomi NPP VIIRS Cloud mask (VCM) tests	JPSS VIIRS BAYESIAN CLOUD_MASK (ECM) tests Byte No. (Bit No.)	Description of Bayesian Cloud Mask tests	Locations where the tests are used in ADP
pCirrus1	2(0) (High cloud 1.38µm)	Cirrus Detection (Byte 1, bit 6)	6 (4-5)	CIRREF- Near IR Cirrus Test (1.38µ m) value=3 (confident cloudy)	Smoke over Water Dust over water Smoke over land Dust over land
pCirrus2	1(7) (High cloud 6.7µm test)	Cirrus Detection (Byte 1, bit 7)	6(4-5)	CIRREF- Near IR Cirrus Test (1.38µ m) value=3 (confident cloudy)	Smoke over Water Dust over water Smoke over land Dust over land
pCirrus3	1(1) (thin cirrus, solar test)	Cirrus Detection (Byte 5, bit 3)	2(3)	Thin Cirrus value=1 (yes)	Smoke over Water Dust over water Smoke over land Dust over land
pFlag1	2(2) (IR Temperature difference)	IR temperature difference test (BTM14 - BTM15) &(BTM15-BTM16) (Byte 2, bit 2)	4 (2-3) &3(4-5)	PFMFT – Positive FMFT (Split-Window BTD) Test and 11µm -8.5µm test value=3 (confident cloudy)	Smoke over land
pFlag2	2(3) (3.7µm-11µm test)	Temperature difference test (BTM15 - BTM12) (Byte 2, bit 3)	3(2-3)	ETROP – Emissivity at Tropopause Test value=3 (confident cloudy)	Smoke over land
pShadow	1(2) Shadow Test	Shadow Detected	2(7)	Shadow contaminated Flag	Smoke over Water Dust over water Smoke over land Dust over land
pFire	N/A	Fire Detected	2(8)	Fire contaminated Flag	Smoke over land Dust over land

3.4 Theoretical Description

The EPS ADP algorithm attempts to separate cloudy and clear pixels from those with smoke or dust. The detection of smoke or dust relies on the distinctive signature of smoke or dust which is often expressed in terms of spectral variations of the observed brightness temperature or solar reflected energy. The spectral variation of the refractive index plays an important role in the success of these methods. In addition, the scattering and absorption properties of aerosols also depend on the particle size distribution and the particle shape. Several aerosol remote sensing techniques have been developed using observations from the Advanced Very High Resolution Radiometer (AVHRR) [e.g. Barton et al., 1992]. Similar to dust plumes, volcanic ash plumes often generate negative brightness temperature differences between 11μm (BT_{11}) and 12 μm (BT_{12}). Prata [1989] has demonstrated the detection of volcanic aerosols using two infrared channels, while Ackerman and Strabala [1994] applied observations at 8.6, 11 and 12μm from the Hyper Spectral Infrared Sound (HIRS) instrument to study the Mt. Pinatubo stratospheric aerosol. Recently, Ciren and Kondragunta [2014] developed a simple and fast technique to detect dust based on MODIS observations in the deep-blue (412 nm), blue (440 nm) and shortwave-IR (2130 nm) bands. This technique utilizes the spectral dependence of dust absorption, surface reflectance, and differences in absorbing/scattering properties between small and large particles.

Image-based aerosol detection always involves assumptions of the radiometric characteristics of aerosol, clear and cloudy scenes. The surface conditions also influence the separation of aerosol pixels from those with clear-sky or cloud. The EPS ADP algorithm currently uses spectral and spatial tests to identify pixels with smoke or dust in the daytime. The algorithm also treats the detection differently for water and land.

3.4.1 Physics of the Problem

Techniques for the remote sensing of aerosols using solar and thermal measurements from satellites have been developed for several instruments, including AVHRR and MODIS. Fundamentally, these methods are based on the radiative signatures of aerosols. The problem of accurate detection and classification is compounded by the fact that the physical characteristics of aerosols (e.g. particle size distribution, concentration, chemical composition, location in the atmosphere) change as the aerosol layer develops and dissipates. These physical changes are capable of affecting the radiative characteristics of the original aerosol and our capability to detect them from satellite observations. In addition to being present at their source regions, aerosols are transported by winds to other regions of the globe.
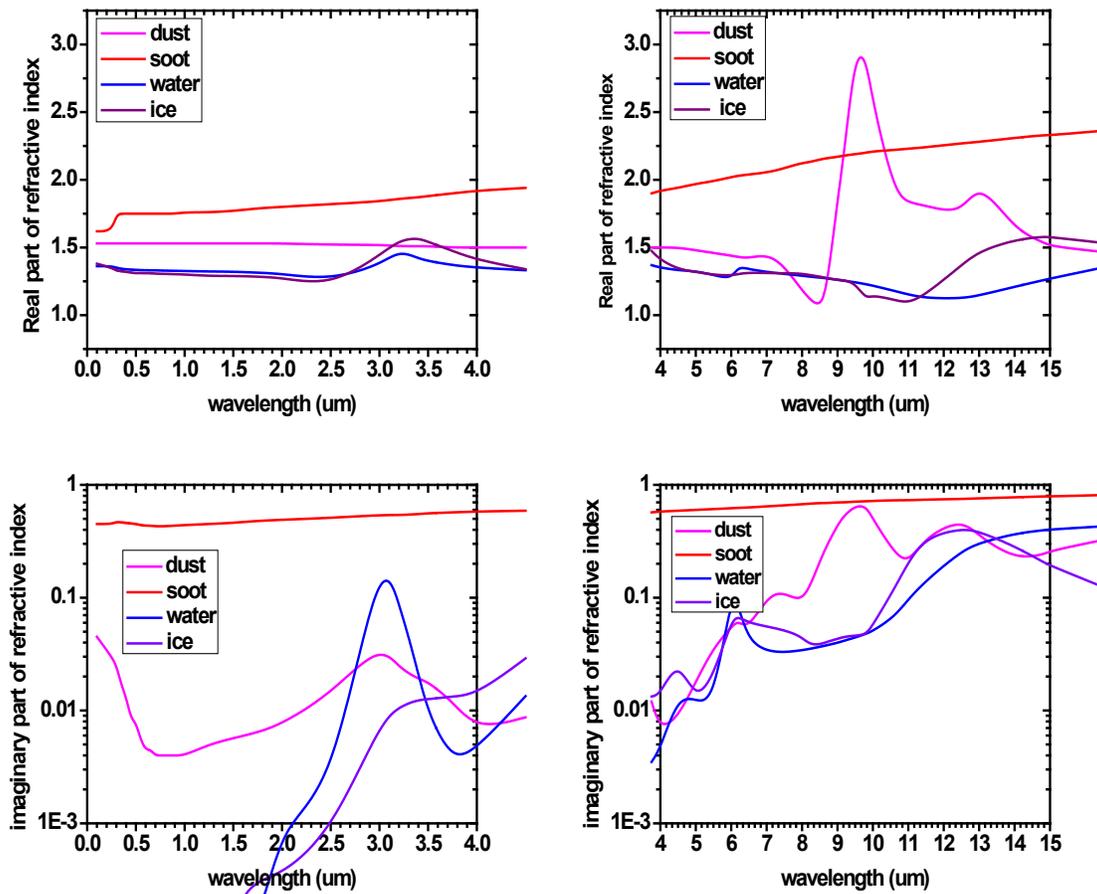
Figure 2: Real and imaginary part of dust, soot, water and ice as a function of wavelength. Plots are based on data obtained from NOAA's Community Radiative Transfer Model (CRTM).

Fundamentally, the radiative signatures of an aerosol layer are determined by the scattering and absorption properties of the aerosol within a layer in the atmosphere. These are:

- Extinction coefficient, σ_{ext} (which integrated over path length gives the optical thickness, τ). This parameter characterizes the attenuation of radiation through an aerosol volume due to aerosol scattering (measured by scattering coefficient σ_{sca}) and absorption (measured by absorption coefficient σ_{abs}) so that $\sigma_{ext} = \sigma_{sca} + \sigma_{abs}$.

- Single scattering albedo, $\omega_{\circ} = \sigma_{sca} / \sigma_{ext}$, which describes how much attenuation of radiation is due to scattering. It ranges between 1 for a non-absorbing medium and 0 for a medium that absorbs and does not scatter energy.

- Phase function, $P(\mu, \mu')$ which describes the direction of the scattered energy. Here μ and μ' are the cosine of solar and local zenith angles, respectively.

There are three important physical properties of a particle that are needed to determine the scattering and absorption properties listed above:

- The index of refraction ($m = m_r - im_i$) of the particle: The index of refraction of the medium is also required, but for air it is 1. Measurements of the index of refraction of a material are very difficult to make [Bohren and Huffman 1983]. The m_r is an indication of the scattering properties while the m_i is an indication of the absorption characteristics of the material. The scattering and absorption properties of an aerosol also depend on the particle size distribution. The index of refraction of smoke and dust is different from ice or water (Figure 2), which suggests that multi-spectral techniques should be useful in separating the aerosol from clouds. In addition, m_i of dust exhibits the sharpest increase with the decreasing wavelength in the deep blue region, indicating the spectral contrast between two neighboring wavelengths in this region can be used to separate dust from other aerosols.
- The shape of the particle: Microscopic analysis reveals that aerosols are irregular in shape. Thus, the assumption of spherical particles is often not accurate but a reasonable approximation. Shape effects may be a particular problem in the vicinity of strong infrared absorption bands for small particles with a uniform size distribution [Bohren and Huffman, 1983]. As no satisfactory method of handling the radiative properties of irregular shaped particles has been developed for general application to remote sensing techniques, the sensitivity studies generally assume spherical shaped particles.
- The size distribution of the particles, *n(r)*: In addition to defining the radiative properties, the *n(r)* also determines the aerosol mass concentration. Particle size distributions of aerosols are often expressed as a log-normal distribution.

Because of these distinctive wavelength dependent aerosol properties, spectral threshold-based techniques are used to detect dust, smoke, volcanic ash. Those techniques generally can be grouped as IR-based, IR/visible based and UV/deep-blue based, depending on the wavelength range of the utilized aerosol signatures. For aerosols with small particle size, such as smoke and haze, their distinctive signatures are mainly in the short-wavelengths, while for aerosols with a large particle size, such as dust and volcanic ash, their distinctive signatures are in the IR wavelengths.

Dust exhibits distinct radiative signatures in the UV, visible and IR regions (Sokolik, 2002). Various satellite-based dust detection techniques have been developed by utilizing its signature either in the UV (Herman et.al, 1997), visible (Miller, 2003; Jankowiak and Tanré´, 1992; Martins et al., 2002; Kaufman et al., 1997), IR (Ackerman, 1997; Darmenov and Sokolik, 2005; Hansell et at., 2007) or a combination of visible and IR (Evan et al., 2006; Cho et al., 2013). Strong absorption by dust and low surface reflectivity in the UV spectral region enables the detection of absorbing aerosols, including dust, in the atmosphere (Herman et al., 1997). In addition, unlike most other dust detection techniques which can only provide a simple binary mask, absorbing Aerosol Index (AI) is also associated with the intensity of dust, although quantifying the dust loading in terms of optical depth requires the knowledge of dust layer height (Hsu et al., 1999; Torres et al., 2002). However, the UV aerosol detection technique is limited by its inability to separate dust from other absorbing aerosols such as smoke. Dust absorption in the visible region (a brownish color as seen by human eyes), is well utilized

to detect dust using spectral and spatial variability tests (Miller, 2003, Darmenov and Sokolik, 2009; Zhao et al., 2010; Cho et al., 2013). However, clouds, other type of aerosols, and bright surfaces can become a major interference. A unique radiative signature of dust in the IR window region, i.e., the negative brightness temperature difference between 11 µm and 12 µm, is widely used to distinguish the effect of dust from that of clouds (Sokolik, 2002; Legrand et al., 2001; Bullard et.al, 2008).

Some algorithms use 8.5 µm in addition to 10 µm and 11 µm to detect dust using tri-spectral differencing techniques (Hu et al, 2008; Ackerman, 1989; Ackerman, 1997, Ashpole *et al.,* 2012). However, Darmenov and Sokolik (2005) indicated that the magnitude or even the sign of the brightness temperature difference depends on the composition of the dust, height of the dust layer, and the surface emissivity; thus, the ability to detect dust can vary from location to location. In addition, another complication with the IR detection of dust is from the water vapor absorption in the longwave IR, which significantly affects the detection over regions and/or seasons depending on atmospheric water vapor content (Ashpole *et al.,* 2012). Besides utilizing the dust signature in the brightness temperature difference between 11 µm and 12µm, Kluser and Schepanski (2009) further utilized the dust effect on the diurnal cycle of brightness temperature in 11 µm to derive a Bi-temporal Mineral Dust Index (BMDI) for Meteosat Second Generation (MSG) IR observations.   However, it is only available over land, applicable only to geostationary satellite observations, and based on the assumption that the diurnal variability of dust plumes is small, which is not always true for transported dust.

The bulk transmittances of dust and volcanic ash display a strong spectral variation in the 8-10 µm and 10-12 µm regions. This is also a spectral region over which the atmosphere is fairly transparent. For these reasons, techniques have been developed that successfully employ satellite radiance measurements at 11 and 12 µm to detect dust and volcanic ash. These split window IR techniques have primarily been applied to volcanic aerosols, particularly those from sulfur-rich eruptions [e.g. Prata 1989; Barton et al. 1992] as well as dust outbreaks [Legrand et al., 1992, 2001; Evan et al., 2006]. As demonstrated in Figure 3, dust absorbs more radiation at 12µm than 11µm, which causes the brightness temperature difference between the two to be negative.

Positive $BT_{11µm}$-$BT_{12µm}$ values are usually associated with clear sky atmospheres, since water vapor has both absorption and emission in the 11 and 12 µm channels, and the weighting function for the 11µm channel peaks lower in the atmosphere than does the 12µm channel. However, the presence of a dry air mass, often associated with dust events, will tend to reduce the positive $BT_{11µm}$-$BT_{12µm}$. In addition, as shown in Figure 2, dust has a larger absorption at 12µm than at 11µm, so dust plumes generally have a higher emissivity and lower transmissivity in the 12 µm channel [Ackerman, 1997; Dunion and Velden, 2004]. For more elevated dust layers, the increased temperature separation between the dust layer and the surface, and coincident reduction of dry air closer to the peak of the 11µm weighting function, makes the split window brightness temperature difference even less positive. However, this difference has also been observed to be affected by the optical thickness of a given dust plume, so that in thick plumes, the $BT_{11µm}$-$BT_{12µm}$ difference becomes more negative. Darmenov and Sokolik [2005] further explored the brightness temperature difference technique using MODIS data applied to dust outbreaks from different regions of the globe. In general, $BT_{8µm}$-$BT_{11µm}$ becomes less negative and

BT$_{11\mu m}$-BT$_{12\mu m}$ becomes more negative with increasing dust loading (Figure 3). However, in the EPS ADP algorithm, the 3.9 μm is chosen instead of 8 μm because 3.9 μm has less water vapor absorption and also to eliminate false alarms from low level clouds (often towering cumulus).

In the short-wavelength region, dust absorbs at blue wavelengths and appears visually brown in color. Clouds are spectrally neutral and appear white to human eyes. For this reason, the reflectances at 0.86, 0.47 and 0.64μm have been used to identify dust. This is often done in a ratio of one to another or as a normalized difference index. For example, the MODIS aerosol optical depth retrieval algorithm has a condition that the ratio of reflectances between 0.47 μm and 0.64 μm should be less than 0.75 for the central pixel in a 3 x 3 box for the pixel to be identified as dust. Evan et al [2006] use a constraint that the reflectance value of the 0.86μm channel ($R_{0.86\mu m}$) divided by the reflectance value of the 0.63μm channel ($R_{0.63\mu m}$) is within the range of 0.6–1.0 for the AVHRR (this range is slightly different for MODIS due to differences in the spectral response functions). Again, due to the nonlinear relationship with optical thickness, we chose to square the reflectances prior to applying a test. The physical basis for this test is that the presence of smaller aerosols, like smoke, tends to reduce the values for this ratio, as smaller particles are more efficient at scattering light at 0.63μm. Although dust particles are observed to scatter more light at 0.63μm than at 0.86μm, probably due to their size, they tend to exhibit more uniform scattering across this spectral region [Dubovik et al., 2002]. Thus, the $R_{0.86\mu m}$/ $R_{0.63\mu m}$ ratio test [Evan et al., 2006] has been found to be useful in discriminating pixels containing smoke from those with dust. Another test for identifying dust over water is the requirement that the ratio of reflectance at 0.47 μm and 0.64 μm is smaller than 1.2. Similar to dust detection over land, low level clouds (often towering cumulus) can also have a negative split window brightness temperature difference. Therefore, the brightness temperature between 3.9 μm and 11 μm can be used to screen out cloud contaminated pixels.
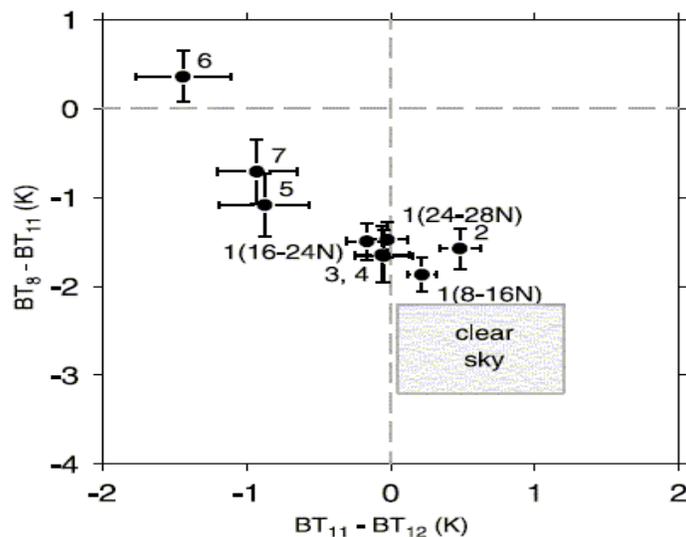
Figure 3. Combined tri-spectral diagram of brightness temperature differences for "heavy dust" pixels, indicated by the number 1 to 7, and for clear sky. From Darmenov and Sokolik [2005].

The VIIRS RGB image in Figure 4-1 shows a dust plume with different regions of heavy dust, thin dust, and clear sky clearly identified. For these different regions, the relationship between different visible and IR BT differences are plotted in the four panels of Figure 4-2. Clear sky pixels have low reflectance at both 0.47 and 0.64 μm, thin dust has elevated reflectances at these channels, and thick dust pixels have 20% or greater reflectance at these channels. The BT difference between 3.9 μm and 11 μm plotted against the BT difference between 11 μm and 12 μm shows a clear separation of thick dust pixels compared to thin dust and clear-sky.
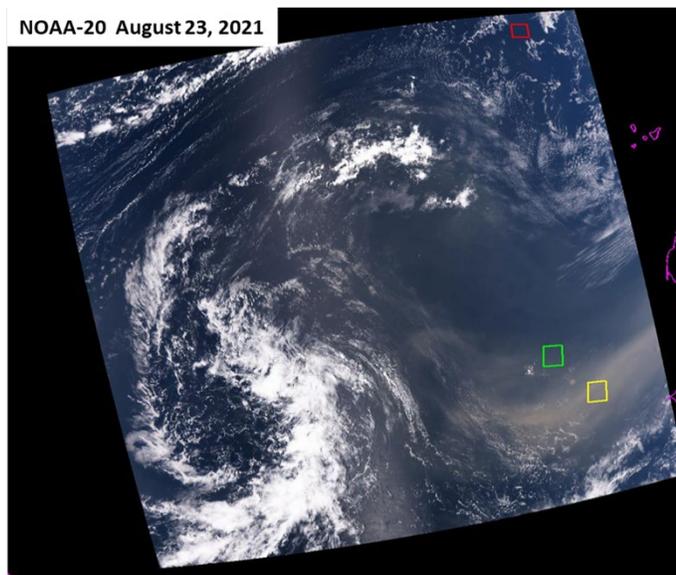
Figure 4-1: NOAA-20 VIIRS true color (RGB) image on August 23, 2021 at 15:20-15:26 UTC for a dust event over the west coast of Africa. The yellow, green, and red boxes represent heavy dust, thin dust, and clear conditions.
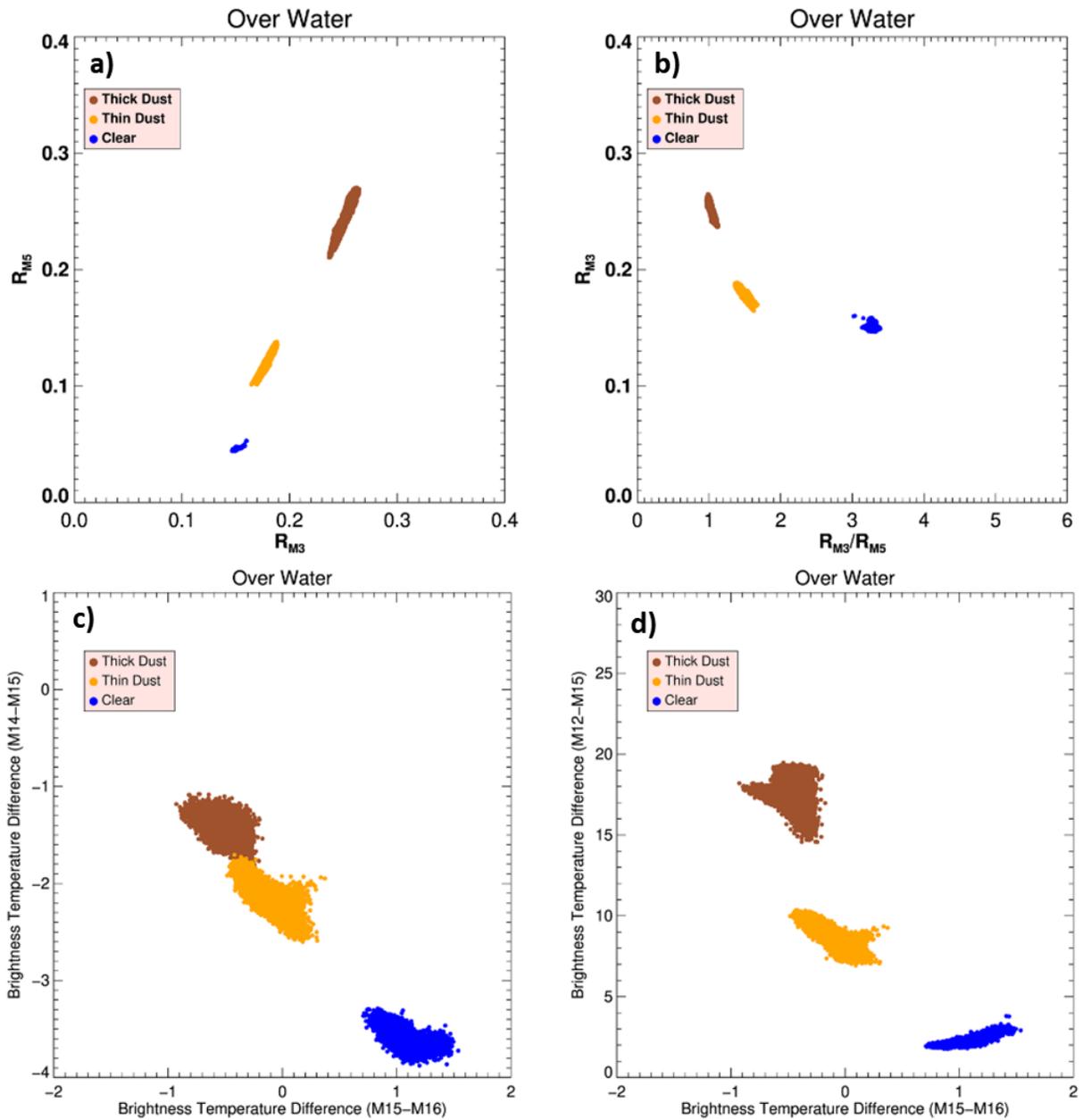
Figure 5-2: For pixels identified as clear (blue; corresponding to red box in Figure 4-1), thick dust-laden (brown; corresponding to yellow box in Figure 4-1) and thin dust-laden (orange; corresponding to green box in Figure 4-1), scatter plots of the relationship between various combinations of VIIRS bands: observed TOA reflectances R3 (M3, 488 nm) vs. R5 (M5, 672 nm) (a), observed TOA reflectances R3 (M3, 488 nm) vs. ratio of R3 (M3, 488 nm) to R5 (M5, 672 nm) (b), brightness temperature difference M14 (8.55 ⬚m)-M15 (10.76 ⬚m) vs. brightness temperature difference M15 (10.76 ⬚m)-M16 (12.01 μm) (c), and brightness temperature difference M12 (3.70 μm)-M15 (10.76 ⬚m) vs. brightness temperature difference M15 (10.76 ⬚m)-M16 (12.01 μm) (d).

Besides separating clouds from other type of aerosols, the challenge of detecting dust lies largely in separating it from a bright surface that is generally the source of airborne dust. In the deep-blue to blue wavelength region, reflectance from a bright surface is well below the critical surface reflectance:

a quantity to define if signal from the aerosol is distinguishable from the surface. A deep-blue aerosol optical depth algorithm developed by Hsu et al (2004) shows aerosol properties can successfully be retrieved even over a bright surface, when measurements at deep blue channels are used. In the deep blue aerosol retrieval algorithm, deep-blue Absorbing Aerosol Index (AAI), defined in a manner similar to the Total Ozone Mapping Spectrometer (TOMS) AI, is used for cloud screening to separate aerosol from clouds, but aerosol type is determined using the aerosol model selected in the aerosol optical thickness retrieval algorithm. Note that, like TOMS AI, the AAI described by Hsu et al (2004) cannot separate dust from other absorbing aerosols.

The advantage of using measurements in the blue wavelength region (410 to 490 nm) to retrieve aerosol optical properties has been clearly demonstrated by Hsu et al. (2004, 2006). Due to the fact that the sensitivity of reflectance to dust in the atmosphere decreases with the increasing wavelength, the spectral contrast between two neighboring wavelengths can be used as an indicator for the presence of dust. The spectral shape of the reflectance at the Top of the Atmosphere (TOA) for a cloud-free atmosphere is determined by three main processes: Rayleigh scattering, absorption and scattering by aerosols, and reflection by the underlying surface. The strong wavelength-dependent Rayleigh scattering creates a strong contrast between two neighboring wavelengths. The presence of dust, however, reduces this contrast as a result of the increased absorption with decreasing wavelength. As for the underlying surfaces, their effects on spectral contrast depend on the spectral variability of surface reflectance. For a surface type such as water, the surface reflectance is nearly independent of wavelength within the deep-blue to blue region except for areas with sunglint; therefore, its effect on the spectral contrast is minimal. However, arid or desert surfaces show increased reflection with increasing wavelength (Hsu et.al. 2004), similar to absorbing aerosol; reflection from these surfaces will also reduce the spectral contrast.

This is illustrated by simulating the spectral dependence at TOA in the blue wavelength region for different surfaces and atmospheric conditions with a thoroughly tested vector version of 6S radiative transfer code (Kotchenova et. al. 2006). Figure 5 shows the ratio between MODIS band 8 (412 nm) and band 9 (440 nm) TOA reflectance at three solar zenith angles (SZA) (i.e. 10°, 30° and 50°) for various scenarios: (a) an atmosphere with only Rayleigh scattering bounded by a black surface (surface reflectance of 0.0), (b) an atmosphere with Rayleigh scattering bounded by desert, vegetation and water, and (c) an atmosphere with Rayleigh scattering and dust bounded by desert, vegetation and water. Note that the sunglint angles are also shown to illustrate the sunglint region over ocean.

In Figure 5, for different scenarios, the dashed line and solid lines represent dust-free and dust conditions with an aerosol optical depth (τ) of 1.0, respectively. A non-spherical dust, i.e., spheroid dust model, based on the almucantur inversion of AERONET observations [Dubovik, 2006] is used in the simulations. The details of the microphysical/optical properties of the dust model were given by Remer et al. [2006]. Surface spectral reflectance of vegetation and sand embedded in 6S are used to represent vegetated and desert surface. The ocean Bi-directional Reflectance Distribution Function (BRDF) from 6S was selected to calculate the ocean surface reflectance for an easterly wind speed of 6 m/s. It is seen that the contrast between reflectances at 412 nm and 440 nm become smaller when dust is present in the atmosphere for desert, vegetation and sunglint-free (with a sunglint angle >30º) ocean surface, compared to dust-free conditions.   The reduction in contrast between the two

wavelengths is most significant for a sunglint-free ocean surface and relatively smaller for desert and vegetated surfaces because a sunglint-free ocean surface has a relatively lower and flat spectral reflectance. For a clear atmosphere over ocean outside of sunglint regions, TOA reflectance is dominated by the spectral signature of Rayleigh scattering. In contrast, desert and vegetated surfaces are brighter and have spectrally increasing reflectance that is opposite of the spectral signature of Rayleigh scattering. Therefore, the spectral variation of TOA reflectance is reduced for a dust-free atmosphere over desert and vegetation. In addition, it is also seen that the decrease in spectral contrast is larger at both a larger viewing zenith angle (VZA) and a larger SZA, since the slant path increases with the increasing SZA and VZA. However, it is also seen that the spectral contrast decreases sharply with decreasing sunglint angle for an ocean surface without dust, indicating that reflection from sunglint itself may reduce the spectral contrast. This has to be considered to avoid misidentifying sunglint as dust.
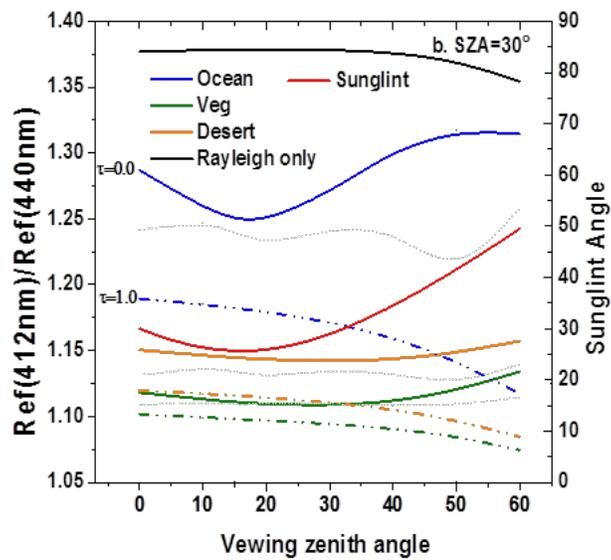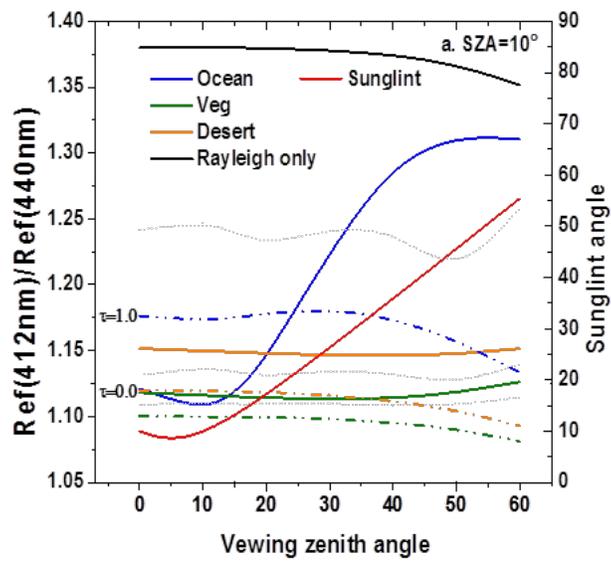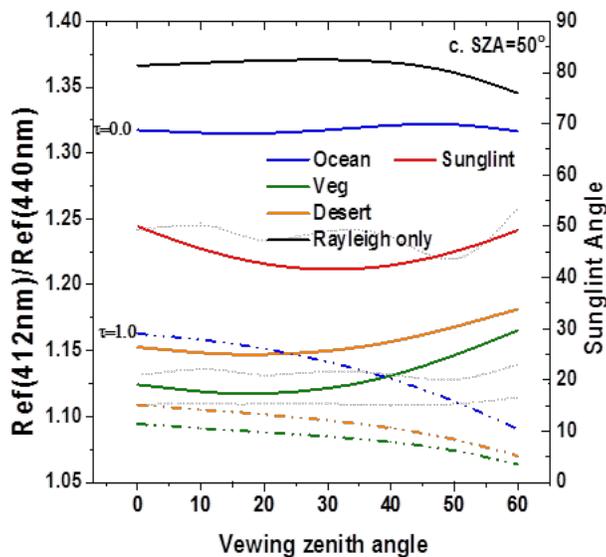
Figure 6: Ratio of the simulated TOA reflectance at MODIS band 8 (412 nm) and band 9 (440 nm) as a function of viewing zenith angle at a solar zenith angle of $10°$ (a), $30°$ (b) and $50°$ (c). Solid lines represent a clear atmosphere bounded by ocean (blue), vegetation (green), and desert (orange). Dashed lines represent an atmosphere with dust (AOD at 550 nm is 1.0) bounded by ocean (blue), vegetation (green) and desert (orange). Red solid lines are sunglint angle over ocean. Relative azimuth angle of 120° is used. Total ozone amount is set at 350 DU.

The reduction in the spectral contrast of Rayleigh scattering when dust is present in the atmosphere is also seen in satellite observations. Figure 6a-b shows the regions highlighted by boxes where pixels are identified as clear and as dusty, respectively, for over land and ocean. Figure 6c-d shows the ratio of TOA reflectance at 412 nm and 440 nm as a function of TOA reflectance at 412 nm for pixels from the selected boxes over land and over ocean. It is seen that the ratio of 412 nm to 440 nm for pixels with dust is distinct from clear pixels over ocean, showing the reduced contrast between 412 nm and 440 nm (see Figure 6d). Such separation is also seen for dust over desert (Figure 6c), although it is not as distinct as that for over ocean.
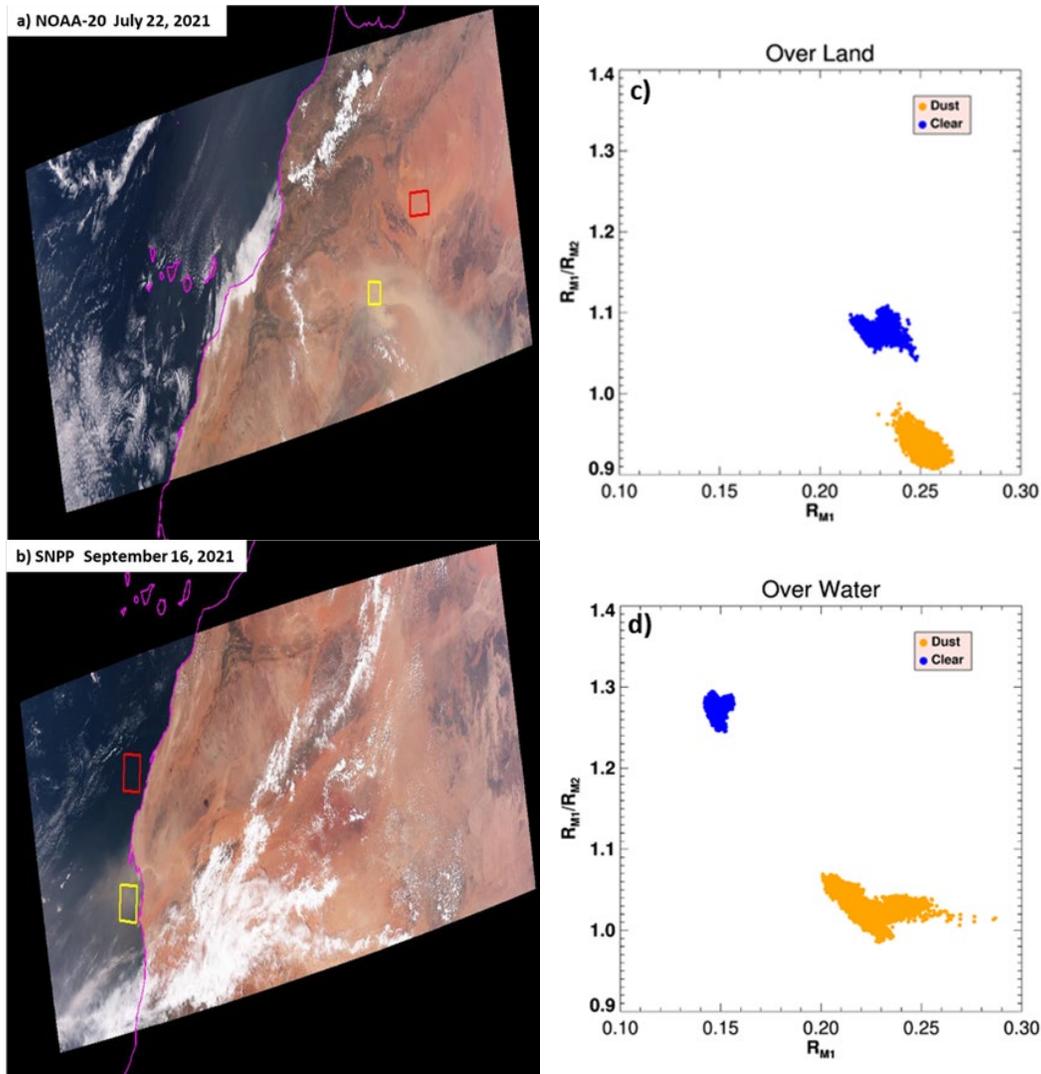
Figure 7: VIIRS true color (RGB) images (red box and yellow box indicate dusty and clear conditions, respectively): NOAA-20 granules on July 22, 2021, ~13:43-13:44 UTC (a) and SNPP granules on September 16, 2021, ~13:42-13:43 UTC (b); for pixels identified as clear (blue) and dust-laden (orange), scatter plots of the observed TOA reflectances (R) of VIIRS bands: ratio of R_{M1} (M1, 412 nm) to R_{M2} (M2, 440 nm) vs. R_{M1} (M1, 412 nm) over land (c) [corresponding to colored boxes in (a)] and over water (d) [corresponding to colored boxes in (b)].

This analysis based on theory and observations suggests that the effect of dust in reducing the spectral contrast between 412 nm and 440 nm could be used as a way to detect the presence of dust in the atmosphere. However, using the spectral contrast under clear conditions as a reference to detect dust requires knowledge of the spectral reflectance of the underlying surface. To bypass this problem, the spectral contrast from pure Rayleigh scattering is used as a reference, and different thresholds for the reduction in spectral contrast is chosen for over land and water. Therefore, an index similar to AI and the absorbing aerosol index used in SeaWiFS (Hsu al, 2000), has been developed, named the Absorbing Aerosol Index (AAI) shown in Equation 1.

$$AAI = -100 \left[log_{10} \left(\frac{R_{412nm}}{R_{440nm}} \right) - log_{10} \left(\frac{R'_{412nm}}{R'_{440nm}} \right) \right] \qquad (1)$$

In Equation 1, R is the TOA reflectance, R' is the reflectance from Rayleigh scattering as computed by 6S code for a given location and satellite viewing geometry. To illustrate how AAI changes with the dust loading, 6S radiative transfer model simulations were used to calculate AAI for dust with different optical depths (at 550nm): no dust (τ=0.0), weak (τ=0.5), heavy (τ=1.0) and extreme dust loading (τ=2.0). Results are given in Figure 7a-c, showing the AAI as a function of viewing zenith angle, respectively for over desert, over ocean and over vegetation. Filled square, triangle, circle and diamond markers respectively represent different dust-loading indicated by dust aerosol optical depth at 550nm (τ) of 0.0, 0.5, 1.0 and 2.0. Dash-dotted, solid and dotted lines correspond to solar zenith angles of 10°, 30° and 50° respectively. The AAI values for heavy and extreme dust loadings are well separated from those of no dust for both desert and vegetation surfaces and especially for the ocean surface outside sunglint regions, indicating AAI is well suited to detect heavy to extreme dust over both land and ocean. For retrievals over desert and vegetation, it is clearly seen that the separation increases with increasing solar zenith angle and increasing viewing zenith angle, suggesting AAI performs better for larger solar and viewing zenith angles. And the difference in AAI becomes smaller with increasing dust loading. However, it should also be noted that the AAI threshold to detect dust has to be carefully chosen to minimize false alarms and maximize detection, especially for low aerosol loading at a lower solar and viewing zenith angles. Over ocean, weak dust loading is not detectable over sunglint regions. Over sunglint-free ocean regions, the separation between weak dust (represented by τ=0.5) and no dust (represented by τ=0.0) loading is much larger than over land and is less sensitive to the changing solar and viewing zenith angles. This finding suggests that detecting low to weak dust loading with AAI is much better over ocean than over land.

However, as shown in Figure 8a, other absorbing aerosols such as smoke also show an effect on the spectral contrast between 412 nm and 440 nm similar to that of dust. Due to the fact that dust particles are considerably larger than smoke particles, dust extends its scattering signature even to shortwave IR wavelengths, whereas smoke is mostly transparent (Kaufman et al, 2000). By introducing observations at shortwave IR wavelengths, it is possible to separate dust from other absorbing aerosols. As an example, Figure 8b shows a scatter plot between TOA reflectance at 412 nm and 2250 nm from VIIRS for pixels identified as smoke, dust and clear-sky over ocean. Pixels with dust have higher reflectance at 2130 nm and are well separated from clear-sky pixels and pixels with smoke. To this
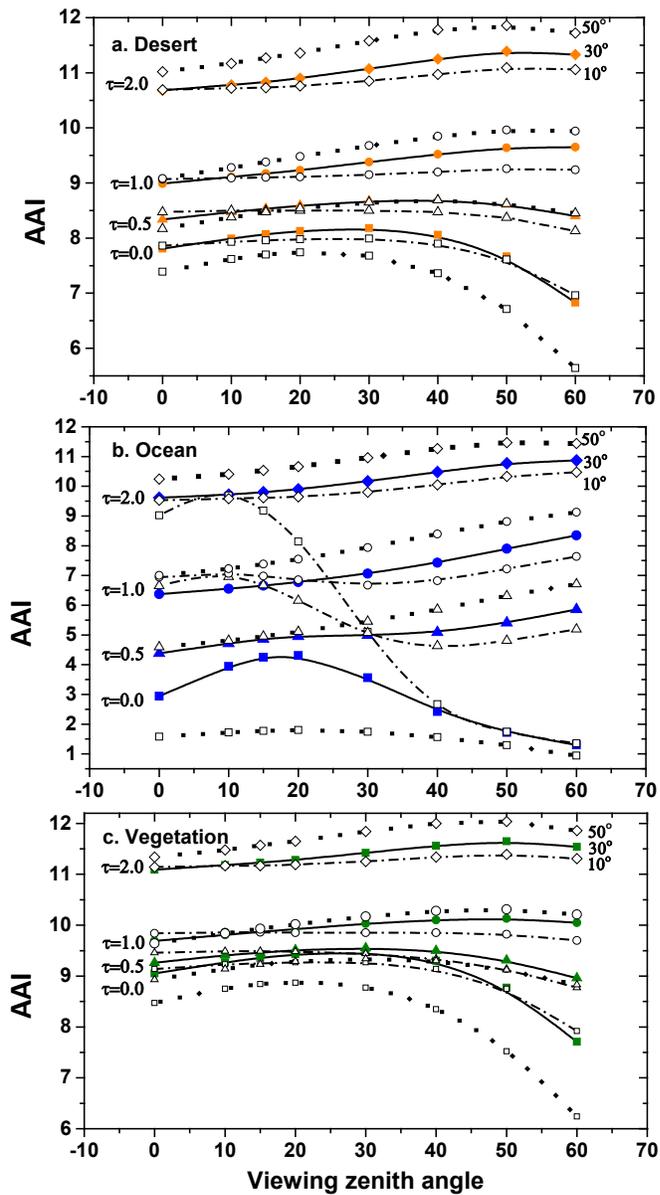
Figure 8: AAI as a function of viewing zenith angle over desert (a), over ocean (b) and over vegetation (c), for aerosol optical depth at 550 nm (τ) of 0.0 (square), 0.5 (triangle), 1.0 (circle) and 2.0 (diamond). Solar Zenith Angle (SZA) of 10°, 30° and 50° is represented by dash-dotted, solid, and dotted lines, respectively. Note that relative azimuth is set at 120°.
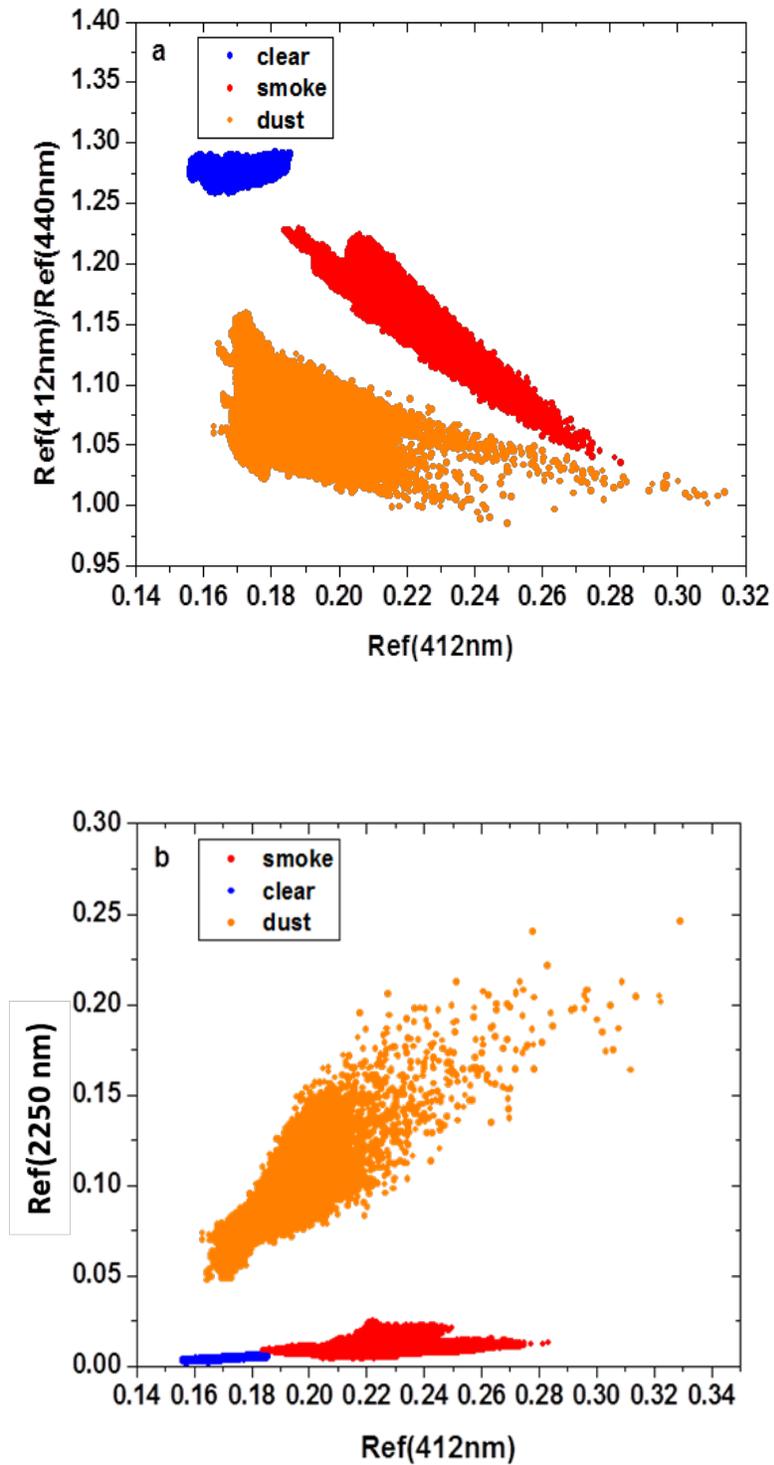
Figure 9: Ratio of the observed TOA reflectance at: a) VIIRS M1 (412 nm) and M2 (440 nm), b) VIIRS M1 (412 nm) and M11 (2250 nm), as a function of the observed TOA reflectance at VIIRS M1(412 nm) for pixels identified as clear (blue), smoke-laden (red) and dust-laden (orange) over ocean.

end, a second index, named the Dust Smoke Discrimination Index (DSDI) is computed using the formula shown in Equation 2.

$$DSDI = -10\left[log_{10}\left(\frac{R_{412nm}}{R_{2250nm}}\right)\right] \qquad (2)$$

In Equation 2, R is the observed TOA reflectance. The DSDI is applied to pixels which pass through the AAI threshold test.

As shown in the above section, by using the spectral contrast between the deep-blue and blue wavelengths, absorbing aerosols, including smoke and dust, can be detected. Furthermore, with the spectral contrast between deep-blue and shortwave IR wavelengths, dust can be separated from other absorbing aerosols, including smoke, indicating this technique can also be used for both smoke and dust detection.

Besides the above-motioned deep-blue technique, signatures of the presence of smoke in other wavelengths are also used for smoke detection. For smoke detection over land, fire spots are first detected by looking at pixels with BTs at 4.05 μm greater than 350K and the BT difference between 4.05 μm and 10.76 μm greater than or equal to 10K. It is assumed that pixels identified as fires using this test have thick smoke. Secondly, smoke tests over land also take advantage of a linear relationship between the reflectance in the visible band (0.67 μm for VIIRS) and shortwave IR band (2.25 μm for VIIRS). Figure 9 shows this relationship with the corresponding VIIRS bands. It is seen that surface reflectance at M5 is generally around 80% of the surface reflectance at 2.25μm. However, due to the fact that the size of smoke particles is relatively small, the signal from smoke will be extremely small in the shortwave IR wavelengths; therefore, there is a larger increase in $R_{0.67\mu m}$ than $R_{2.25\mu m}$ for an atmosphere in the presence of smoke. As for separating smoke from clouds, spatial uniformity tests for the M5 (0.67 μm) band are used for over land, since clouds show large variability in this band compared to smoke, and also the surface is darker.

As for smoke detection over water, spatial variability tests will also help in avoiding the mis-classification of clouds as smoke. Since clear pixels, pixels loaded with thick smoke, and clouds are more uniform than pixels with partial cloud or thin dust, by using the standard deviation of the reflectance at 0.86 μm, where both aerosol and cloud effects are moderate, pixels which contain thick smoke vs. clouds/thin smoke can be separated. It is known that in visible wavelength channels, smoke looks brighter than the water surface but darker than a cloud. However, it is very difficult to completely separate smoke by only using the reflectance test. Therefore, based on the fact that reflection from clouds is spectrally independent, while reflection from smoke has a strong wavelength dependence, spectral contrast tests are combined to separate clouds, smoke, and water surfaces. First, the ratio between $R_{0.47\mu m}$ and $R_{1.61\mu m}$ is used; the rationale for choosing these two channels is because the aerosol effect is larger at 0.47μm but water is darker at 1.61μm. Second, the ratio between $R_{2.25\mu m}$ and $R_{1.61\mu m}$ is combined to enhance the separation of smoke from clouds. Third, by constraining $R_{0.47\mu m}$ and $R_{1.61\mu m}$, thick smoke can be identified.
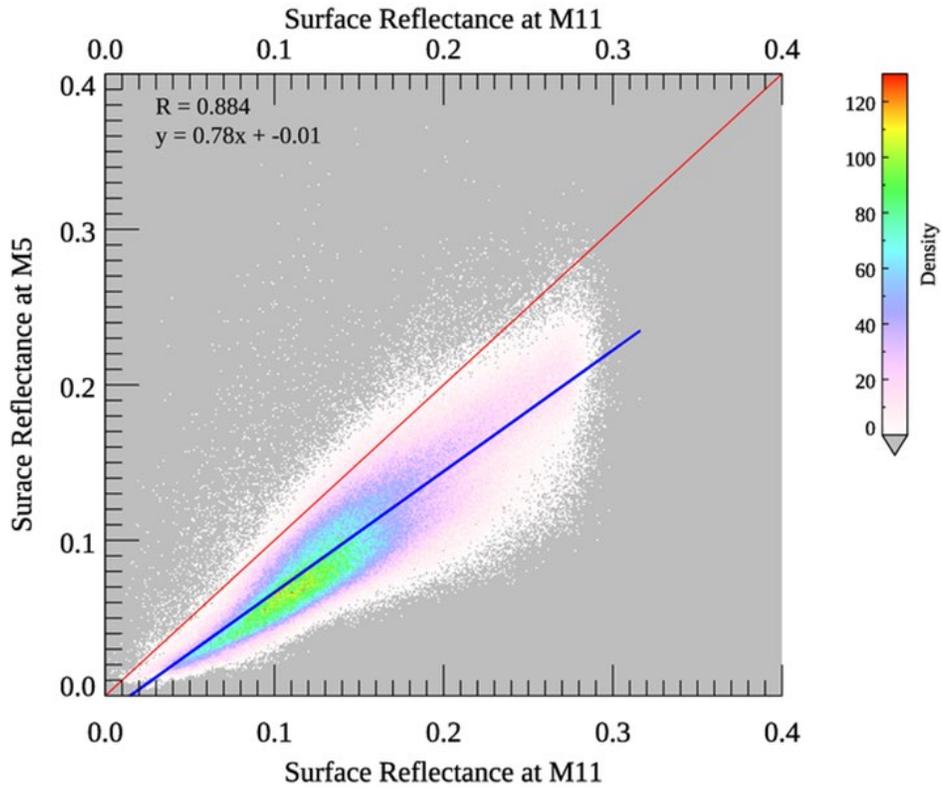
Figure 10 : Surface reflectance at M5 (0.67μm) vs. surface reflectance at M11 (2.25μm) from S-NPP VIIRS.

As an illustration, scatterplots of the ratio of $R_{0.47\mu m}$ to $R_{1.61\mu m}$ and the ratio of $R_{2.25\mu m}$ to $R_{1.61\mu m}$ against $R_{0.47\mu m}$ and $R_{1.61\mu m}$ are shown, respectively, for clear pixels, pixels loaded with thick smoke, pixels loaded with thin smoke, and cloudy pixels, in Figure 10.
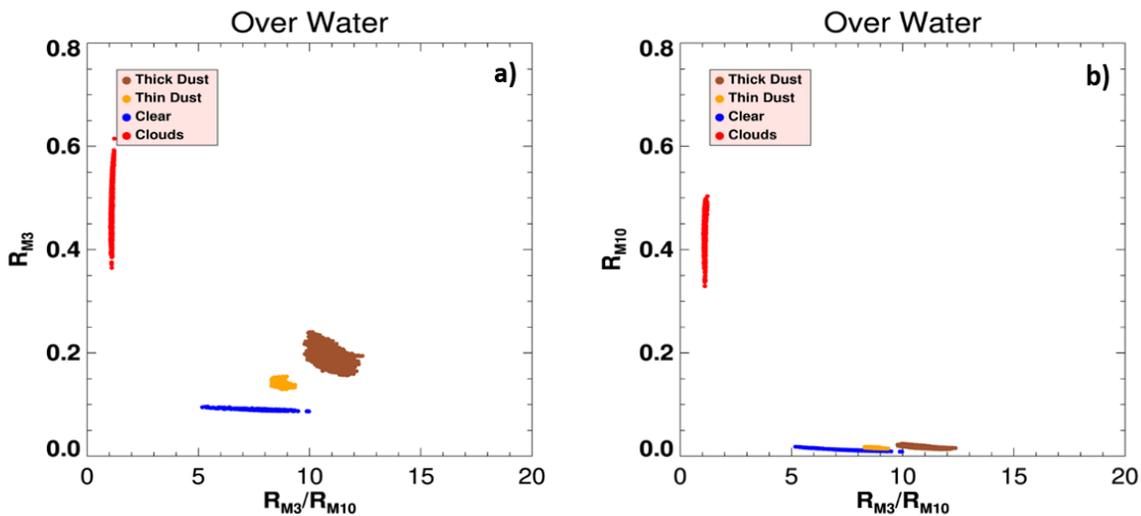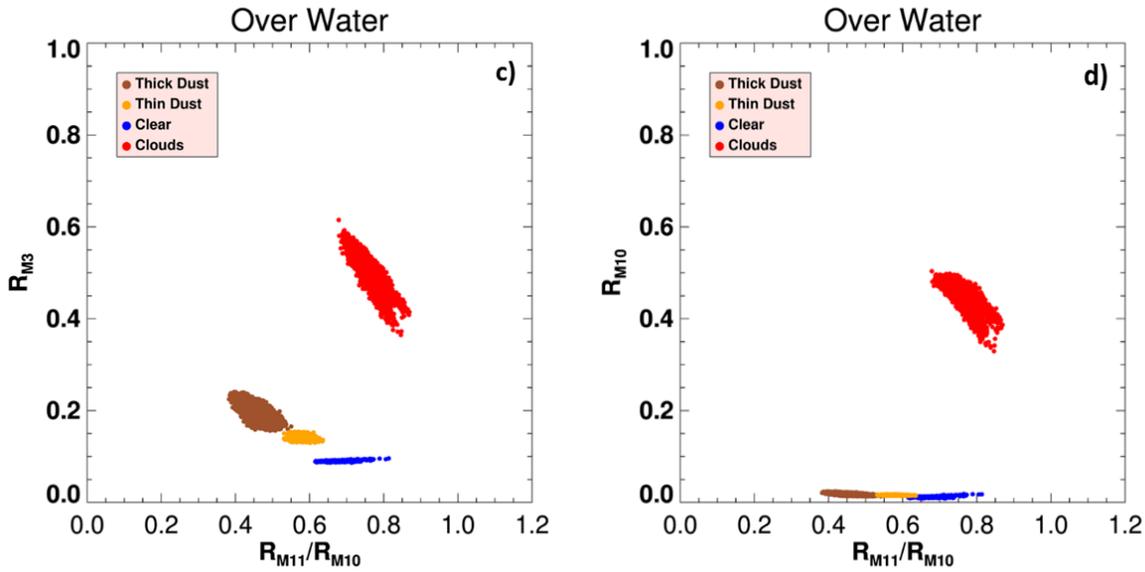
Figure 11: For pixels identified as clear (blue), thick smoke-laden (dark brown), thin smoke-laden (light brown), and cloudy (red) over water, scatter plots of the observed TOA reflectances (R) of VIIRS bands: R_3 (M3, 488 nm) vs. ratio R_3 (M3, 488 nm) to R_{10} (M10, 1061 nm) (a); R_{10} (M10, 1061 nm) vs. ratio of R_3 (M3, 488 nm) to R_{10} (M10, 1061 nm) (b); R_3 (M3, 488 nm) vs. ratio of R_{11} (M11, 2250 nm) to R_{10} (M10, 1061 nm) (c); and R_{10} (M10, 1061 nm) vs. ratio of R_{11} (M11, 2250 nm) to R_{10} (M10, 1061 nm) (d).

3.4.2 Mathematical Description

Computation of the binary flag for smoke/dust in the EPS ADP algorithm is a process of elimination and determination. It has three levels. First, any pixel which contains cloud (ice, high and optically thick clouds) and snow/ice, determined from the input cloud mask and snow/ice mask, is tagged as a cloudy or snow/ice pixel, respectively, and not processed. Second, pixels contaminated by clouds but not screened by the cloud mask are further identified by a combination of spectral and spatial variability tests. Third, spectral contrast tests, such as AAI and DSDI (see Equations 1 and 2), are used to determine if a pixel has smoke or dust. Due to the fact that the contrast of smoke/dust to the underlying surface is different for land and water, computation of the binary flag for smoke/dust in the ADP is separated for land and water.

The following sections describe the various tests employed in the EPS ADP algorithm in detail. Besides the two indices defined in Equations (1) and (2), the symbols and formulae used in the various tests throughout the EPS ADP algorithm are defined as follows:

$$R_1 = \frac{R_{M3}}{R_{M5}}$$

$$R_2 = \frac{R_{M7}}{R_{M5}}$$

$$R_3 = \frac{R_{M3}}{R_{M10}}$$

$$R_4 = \frac{R_{M11}}{R_{M10}}$$

$$Rat_1 = \frac{R_{M5} - R_{M3}}{R_{M5} + R_{M3}}$$

$$Rat_2 = \frac{Rat_1^2}{R_{M3}^2}$$

$$NDVI = \frac{R_{M7} - R_{M5}}{R_{M7} + R_{M5}}$$

$$MNDVI = \frac{NDVI^2}{R_{M5}^2}$$

In the formulae listed above, "*Rat*" is ratio, "*NDVI*" is Normalized Difference Vegetation Index, "*MNDVI*" is Modified Normalized Difference Vegetation Index, and "*R*" is the TOA reflectance. Additional variables include "*BT*" for Brightness Temperature, "*BTD*" for Brightness Temperature Difference, and "*StdR*" for Standard Deviation of Reflectence. *StdR* is computed spatially for a pixel centered in a box containing 3 x 3 pixels. For a pixel that is not on the edge of a scan, *StdR* is computed from the surrounding 3 x 3 pixels. For pixels on the edge of a scan, the standard deviation for the closest pixel is assigned.

3.4.2.1 Snow/ice test over land

Before proceeding to any tests over land, it is important to identify pixels contaminated by snow/ice. As described earlier, the VIIRS snow/ice product is the primary source, and if the primary source is unavailable, the snow/ice mask from IMS is used as a secondary source. However, a further test is designed to catch any pixels that pass through but have snow/ice.

The specific internal tests as currently implemented are:
1) Good data test
    - R_{M7}, $R_{M8.}$ > 0.0   &
    - BT_{M15} > 0.0K   &
    - VIIRS quality flags for above channels indicate good data.

If the good data test passed then the process precedes, otherwise the process is terminated.

2) Snow and Ice tests
The Internal snow ice test over land relies on the brightness temperature at M15 (BT_{M15}) and the Normalized Difference Snow Index ($NDSI$). $NDSI$ is defined as:

$$NDSI = \frac{(R'_{M7} - R'_{M8})}{(R'_{M7} + R'_{M8})} \tag{3}$$

where R'_{M7} and R'_{M8} are Rayleigh-coorected TOA reflectance. Pixelsare defined as snow/ice comtamined if $BT_{M15} < 285K$ and $NDSI > 0.1$. In this case, ADP detetction is avoided and the detetced snow/ice is outputted in the snow/ice flag for quality control purposes for this pixel.

3.4.2.2 Sea ice test over water

Before proceeding to any tests over water, it is important to identify pixels contaminated by sea ice. As described earlier, the VIIRS snow/ice product is the primary source, and if the primary source is unavailable, snow/ice mask from IMS is used as a secondary source. However, a further test is designed to catch any pixels that pass through but have sea ice.

The specific internal tests as currently implemented are:
   3) Good data test
      - R_{M5}, $R_{M10} > 0$ &
      - $BT_{M15} > 0K$ &
      - VIIRS quality flags for above channels indicate good data

If the good data test passed then the process precedes, otherwise the process is terminated.

   2). Sea Ice tests:

   if $BT_{M15} \leq 275k$ & $\frac{(R'_{M5} - R'_{M10})}{(R'_{M5} + R'_{M10})} > 0.4$ &
   $R'_{M5} > 0.1$ & $R'_{M10} > 0.05$
   then sea ice indicated for this pixel.

R´ is the Rayleigh-corrected TOA reflectance.

3.4.2.3   Dust Detection over Land

Dust detection over land has two paths. If either path identifies the presence of dust, then dust is shown to be present in the product. The first path uses the same algorithm as the GOES-R Advanced Baseline Imager (ABI) to detect dust over land, which is based on the spectral variability tests in the visible bands and the negative brightness temperature difference between two wavelengths in the IR regions; the second test is designed for VIIRS, by taking advantage of the VIIRS bands in the deep-blue range. The chosen path is determined by the availability of channels; if deep-blue channels (i.e., M1 and M2 for VIIRS) are not available, the algorithm takes the first path only. Otherwise, both paths are taken.

3.4.2.3.1   IR and visible-based dust detection

The IR and visible-based algorithm is adopted from the heritage of the GOES-R ABI EPS ADP algorithm. Figure 11 is a flow chart of the IR-Visible path of the EPS ADP algorithm to detect the presence of dust over land during daytime (defined as solar zenith angle less than or equal to 87º degrees). The tests are not performed over snow and ice or in the presence of clouds.

The specific tests as currently implemented are:

(1) Test for the presence of snow/ice by using both the primary snow/ice mask and internal snow/ice test, which is described in section 3.4.2.1. However, for dust detection over land, the cloud mask is not applied to avoid the frequent miss-identification of dust plumes as clouds in the cloud mask. Pixels with obvious cloud contamination are eliminated by requiring the reflectance at M1 (after correction for Rayleigh scattering) is larger than or equal to 0.4, i.e., $R'_{M1} \geq 0.4$, and the cloud flag is set as 1. Any pixel with a positive snow/ice mask is not processed, and the corresponding snow/ice flag is set as 1.

(2) Test for the quality of the input radiance data

- $R_{M9} > 0.0$ &
- BT_{M13}, BT_{M15}, $BT_{M16} > 0.0K$ &
- VIIRS quality flags for above channels equal to zero, indicating the quality of the data is assured.

(3) Thin Dust detection: BTD and R tests – check for pixels with thin dust and no cirrus clouds

- If BT_{M15}-$BT_{M16} \leq$ -0.2K & 20K $\leq BT_{M13}$- $BT_{M15} < 25K$ & $R_{M9} < 0.055$ & $MNDVI > 0.08$ then thin dust (1) is present
- If BT_{M15}-$BT_{M16} \leq$ -0.2K & BT_{M13}- $BT_{M15} \geq 20K$ & $0.035 \leq R_{M9} < 0.055$ & $MNDVI > 0.08$ then thin dust (2) is present

(4) Thick dust detection

- If BT_{M15}-$BT_{M16} <$ -0.2K & BT_{M13}- $BT_{M15} \geq 25K$ & $R_{M9} < 0.035$ & $MNDVI > 0.2$ then thick dust is present
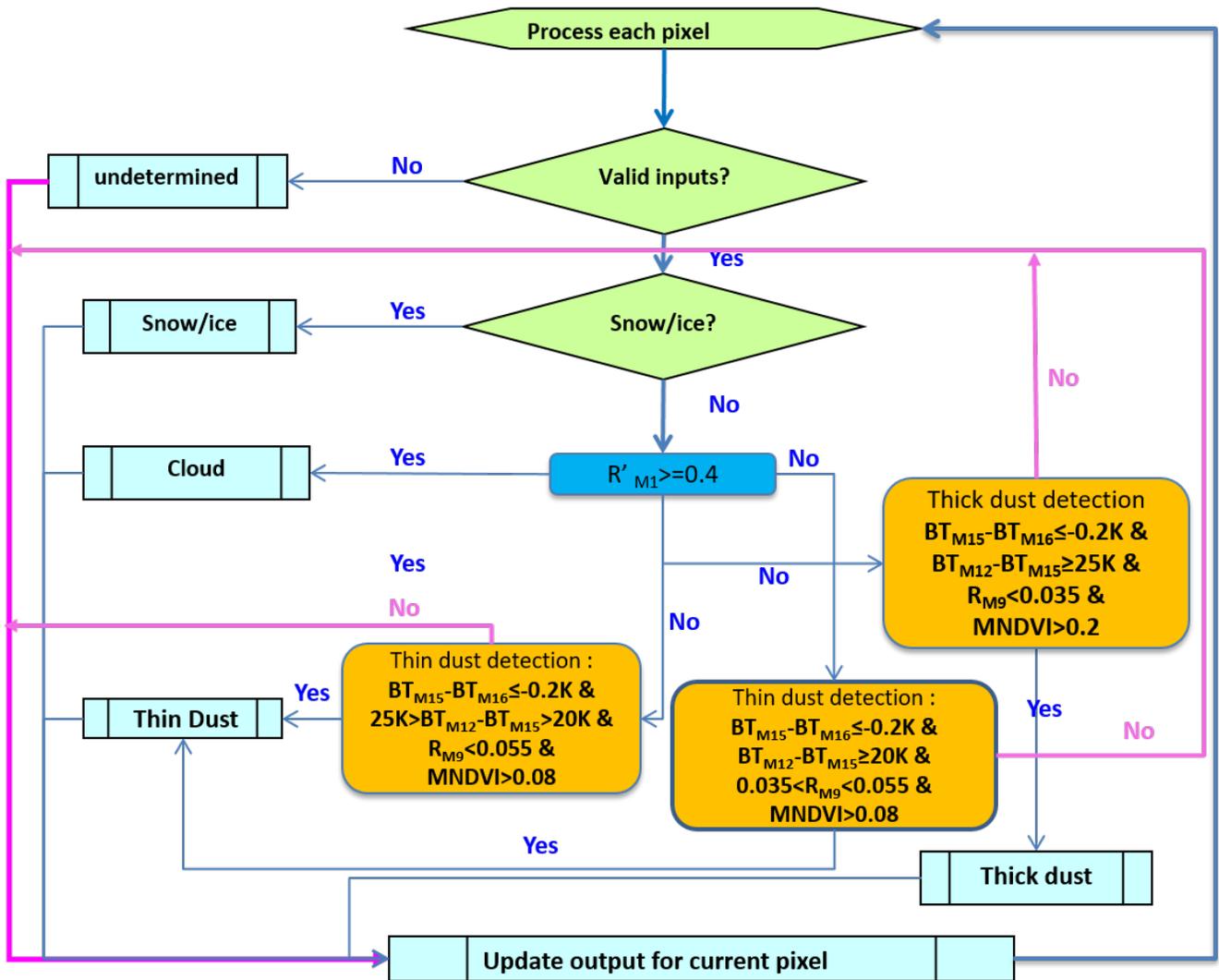
Figure 12: Detail Flow chart of IR-Visible based dust detection over land.

3.4.2.3.2   Deep-blue based dust detection

Figure 12 is a flow chart of the deep-blue path of the EPS ADP algorithm to detect the presence of dust over land during daytime (defined as solar zenith angle less than or equal to 87° degrees). The tests are not performed over snow and ice or in the presence of clouds.

The specific tests as currently implemented are:

(1) Test for the presence of snow/ice by using both the primary snow/ice mask and internal snow/ice mask, which is described in section 3.4.2.1. The test for the presence of clouds relies on cirrus cloud tests in the VIIRS cloud mask and Rayleigh-corrected reflectance at M1. A pixel is considered to be obscured by clouds if any of these three cloud tests in Table 10, i.e. pCiirus1,

pCirrus2 and pCirrus3, is true, or $R'_{M1} \geq 0.4$. Any pixel that tests positive for the presence of snow/ice or clouds is not processed, the corresponding snow/ice flag/cloud flag is set as 1.

(2) Test for the quality of the input radiance data

- R_{M1}, R_{M2}, R_{M8}, R_{M11} > 0.0 &
- VIIRS quality flags for the above channels equal to zero, indicating the quality of the data is assured.

(3) Bright surface test

- R_{M8}, R_{M11} > 0.0 &
- VIIRS quality flags for the above channels equal to zero, indicating the quality of the data is assured.

$$Bridx = \frac{(R_{M8} - R_{M11})}{(R_{M8} + R_{M11})} \qquad (4)$$

If *Bridx* <0.05 or R_{M11} >0.25 then the pixel is considered a bright pixel.

(4) Dust detection: AAI and DSDI tests – check for pixels with dust

If AAI >10.0 and DSDI ≥0.0, dust exists for the pixel. Once dust is detected for the pixel, the dust flag is set and the value of the Scaled Absorbing Aerosol Index (SAAI), which is associated with the intensity of the dust, is obtained by scaling AAI as follows:

$$SAAI = AAI - 10.0 \qquad (5)$$

(5) Residual cloud test

Residual cloud contamination is determined by standard deviation of R_{M1} (*StdR$_{M1}$*) in a 3 by 3 box centered with the processed pixel. If *StdR$_{M1}$*≥0.01, residual cloud exists for the processed pixel and it is assigned as cloudy.

Process each pixel

undetermined ← **No** — **Valid inputs?**

Yes

Snow/ice ← **Yes** — **Snow/ice?**

No

Cloud ← **Yes** — **Cloud ?**

No

Bright Surface

Cloud ← **Yes** — $R'_{M1} >= 0.4$

No

Yes → **Bright Surface Test:**
$Bridx = (R_{M8} - R_{M11})/(R_{M8} + R_{M11})$
$Bridx < 0.05$ or $R_{M11} > 0.25$

Dust ← **Yes** — **Dust Detection:** AAI >10.0 & DSDI>=0.0 ← **No** — **Uniformity test:** $StdR_{M1} >= 0.01$

No

Yes

Cloud

Update output for current pixel
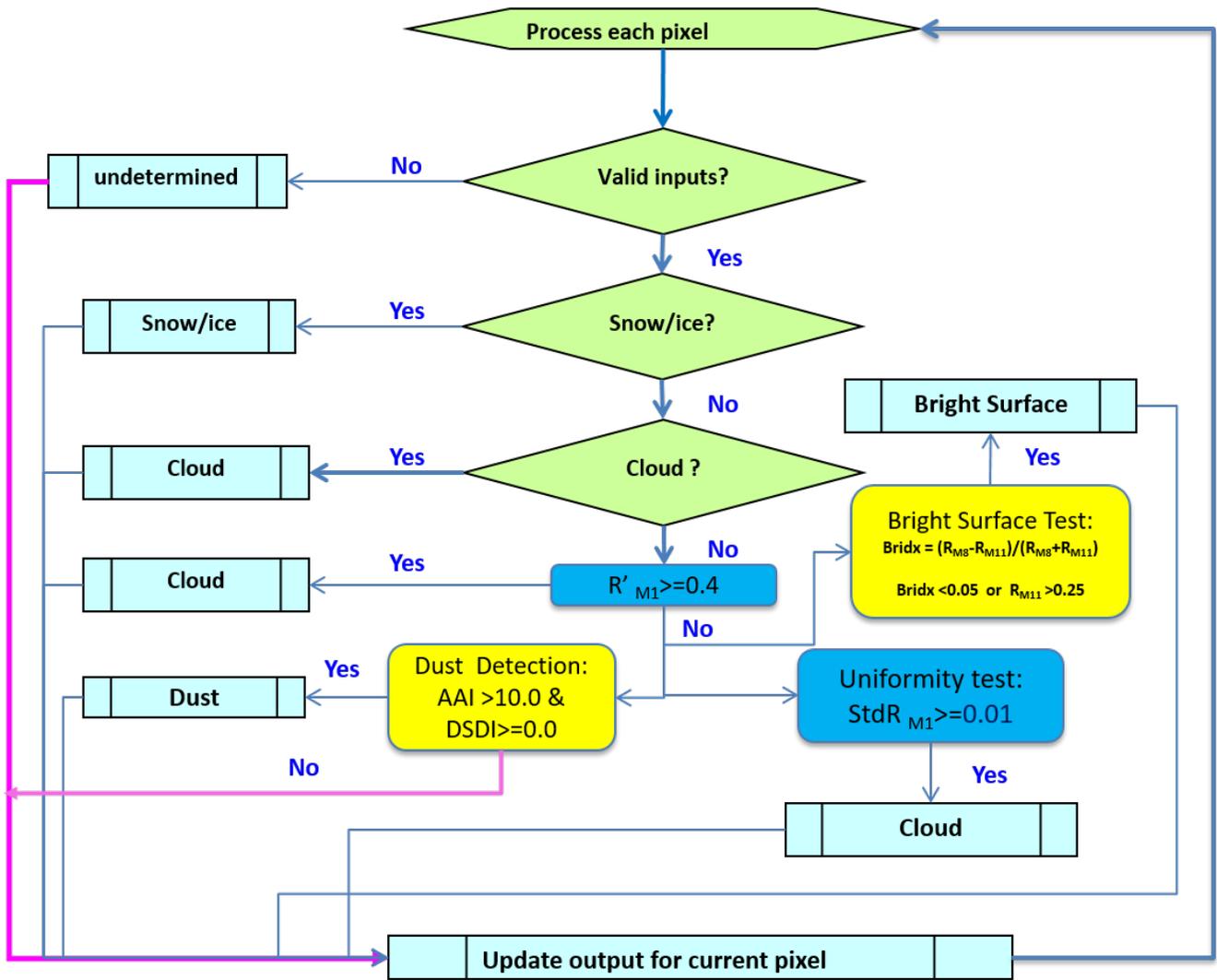
Figure 13: Detail Flow chart of deep-blue based dust detection over land.

3.4.2.3.3 Determination of quality and confidence flags

As shown in Section 2.1, dust detection quality flags, which have a value of 1/2/0, are defined as low, medium and high confidence, respectively. Determination of the level of confidence in the quality flag relies on several steps as follows:

1. If the pixel is determined to be a bright surface, or masked as confident adjacent cloud or cloud shadow in the cloud mask, then the dust flag for this pixel is assigned a quality flag value of 1, i.e., low confidence.

2. The magnitude of AAI and DSDI are also used to assess the quality of detection.

In general, there are three types of tests, i.e., (1) Value of the test < threshold; (2) Value of the test > threshold; and (3) Value of the test is within a range of two thresholds. Detailed descriptions on how the confidence value (given as Con_value) is assigned for each type of tests are given as follows.

Test type 1: used if test looks like value < threshold or value ≤ threshold

The Con_value is calculated as follows:

- If $(threshold - value) < value_1$ then Con_value = 0.0
- If $value_1 \leq (threshold - value) < value_2$ then Con_value = 0.5
- If $(threshold - value) \geq value_2$ then   Con_value = 1.0

Where $value_1$ is 0.05×threshold, $value_2$ is 0.30×threshold. However, under the circumstance that the threshold is 0.0, $value_1$ and $value_2$ is assigned with values of 0.05 and 0.3, respectively.

Test type 2: used if test looks like value > threshold or value ≥ threshold

  The Con_value is calculated as follows:

- If $(value - threshold) < value_1$ then Con_value = 0.0
- If $value_1 \leq (value - threshold) < value_2$ then Con_value = 0.5
- If $(value - threhsold) \geq value_2$ then Con_value = 1.0

Where $value_1$ is 0.05×threshold, $value_2$ is 0.30×threshold. However, under the circumstance that the threshold is 0.0, $value_1$ and $value_2$ is assigned with values of 0.05 and 0.3, respectively.

Test type 3: used if test looks like: upper threshold (< or ≤) value (< or ≤) lower threshold

The Con_value is calculated as follows:

$$dv = \frac{(upper\ threshold - lower\ threshold)}{3}$$

- If $(value < threshold_{lower} + dv)$
      or $(threshold_{upper} - dv < value)$ then   Con_value = 0.0
- If $(threshold_{lower} + dv \leq value \leq threshold_{upper} - dv)$ then Con_value = 1.0

Once Con_value is calculated for an individual test, the ensemble confidence value is then calculated by averaging the confidence value for all the tests. The final confidence level is determined by the ensemble confidence value. i.e., high confidence for an ensemble confidence value ≥0.66, low confidence for an ensemble confidence value ≤0.33, and medium confidence for an ensemble

confidence value >0.33 and <0.66. Details on the determination of the confidence level for dust detection over land are given as follows:

    a. For Deep-blue based dust detection as shown in section 3.4.2.2.2

Test1: AAI ≥ 10.0
Test2: DSDI ≥ 0.0

Intermediate confidence value (con_value$_a$) is calculated by averaging the con_value for Test1 and Test2 as follows:

$$\text{con\_value}_a = \frac{\text{con\_value(Test1)} + \text{con\_value(Test2)}}{2} \tag{6}$$

    b. For IR and visible-based dust detection shown in section 3.4.2.2.1

The BTD between BT_{M15} and BT_{M16} is chosen as the crucial test. The confidence level is defined as follows:

Crucial Test: BTD=$BT_{M15} - BT_{M16}$

Intermediate confidence value (con_value$_b$) is calculated as follows

If -0.3<BTD⩽-0.2 then con_value$_b$=0.2
If -0.6<BTD⩽-0.3 then con_value$_b$=0.5
If   BTD⩽-0.6 then con_value$_b$=0.8

    c. Ensemble confidence

The ensemble confidence value is finally calculated by summing up the con_value$_a$ and con_value$_b$. The final confidence level is set as low if the ensemble confidence value is ≤ 0.25; the confidence level is set as medium if the ensemble confidence value is > 0.25 but <0.50; and the confidence level is set as high if the ensemble confidence value is ≥0.50.

3.4.2.3.4　Example results

The results of an application of the JPSS EPS ADP algorithm to S-NPP VIIRS observations on September 14, 2013 at around 20:20 UTC is shown in Figure 13. The top panel of the figure is a red-green-blue (RGB) false color image of the scene showing the location of the dust outbreak. The bottom panel of the figure shows the results of the smoke/dust detection. Pixels flagged as dusty are colored as yellow to brown, which is scaled with the AAI values, as defined in Equation 5. A second example is given in Figure 13, which is for another dust event on December 14, 2013.
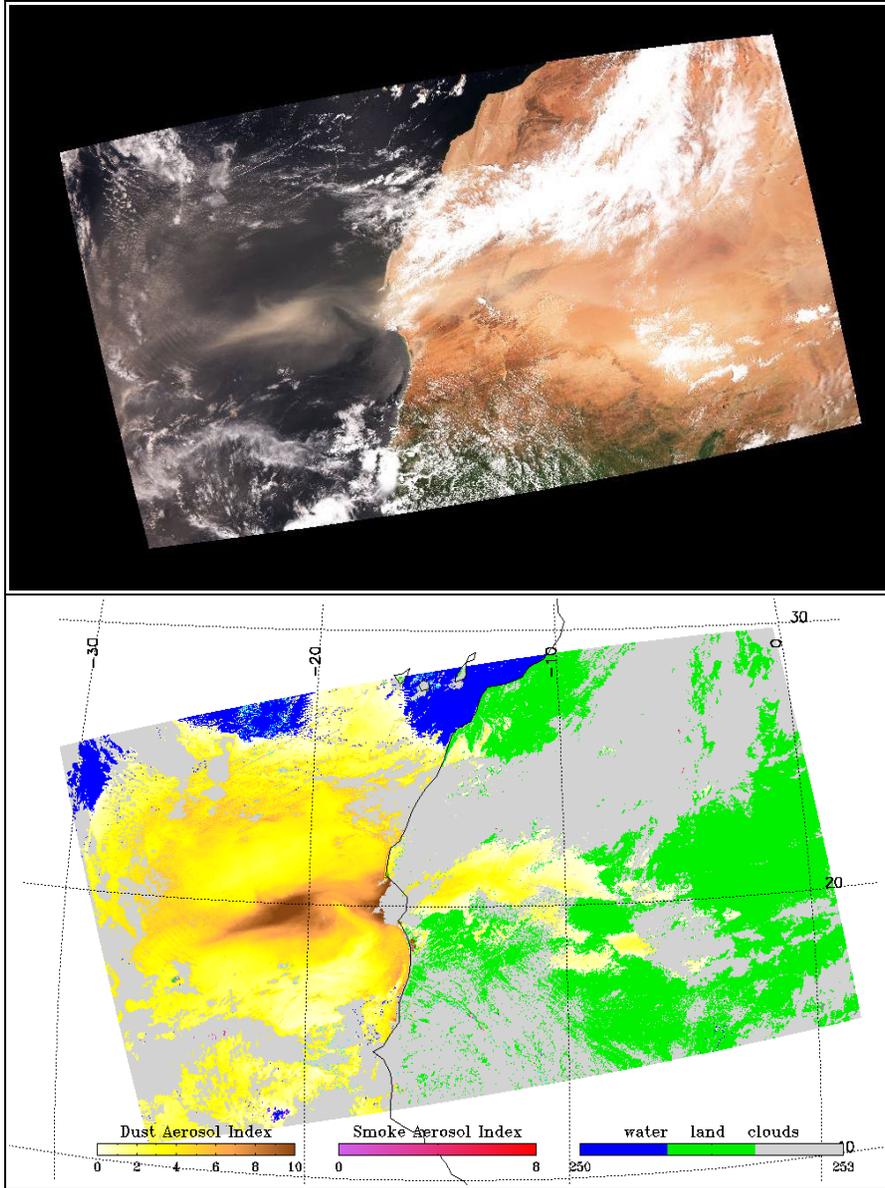
Figure 14: Top: a red-green-blue (RGB) false color image of S-NPP observation on September 14, 2013 at approximate 20:20 UTC. Bottom: the results of the dust detection where pixels flagged as dusty are colored as yellow to brown, scaled by AAI.
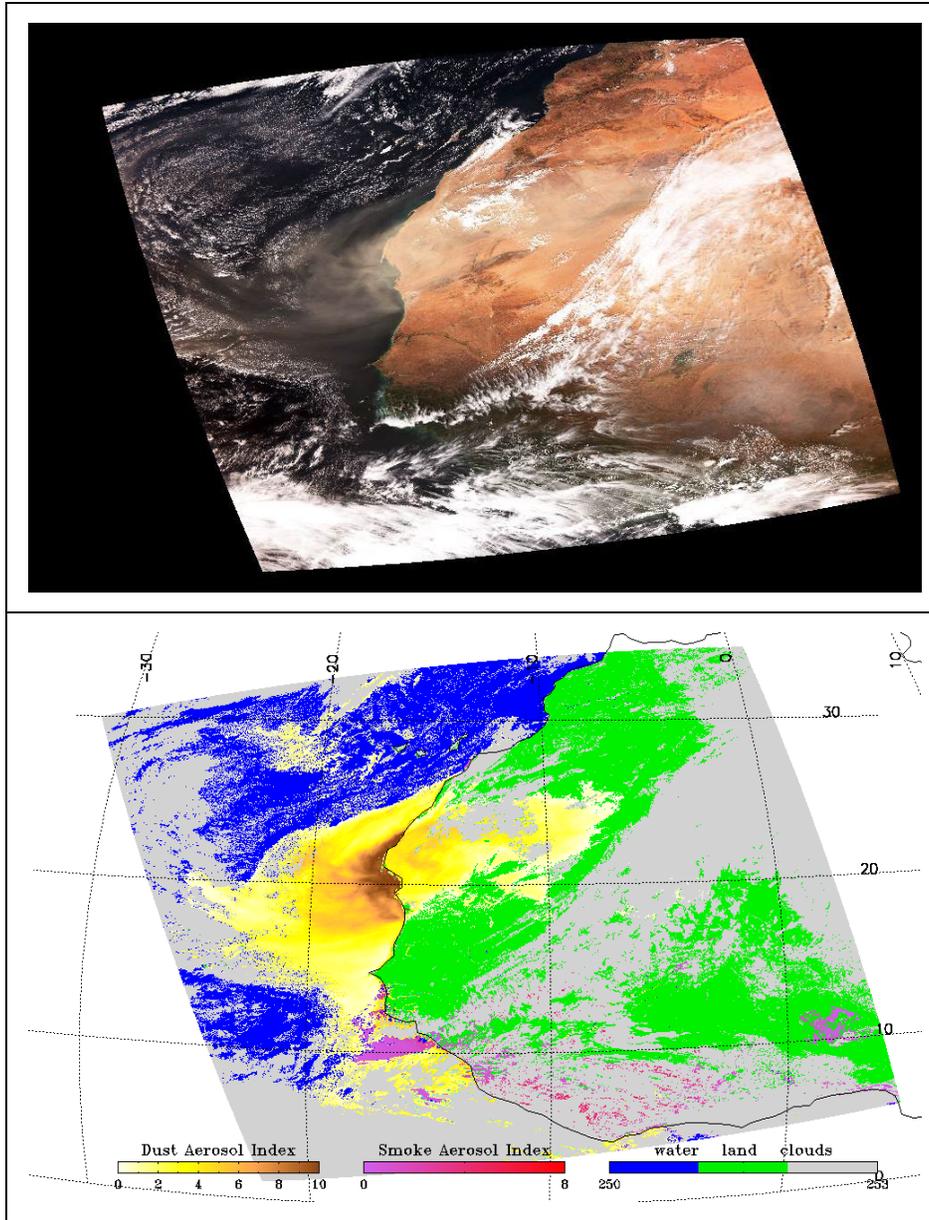
Figure 15: Top: a red-green-blue (RGB) false color image of S-NPP observation data on December 14, 2013 at approximate 19:55 UTC. Bottom: the results of JPSS EPS ADP algorithm where pixels flagged as dusty are colored as yellow to brown, scaled by AAI; pixels flagged as smoke are colored as pink to red, scaled by AAI.

Process each pixel

Valid inputs? — No → undetermined
Yes ↓

Snow/ice? — Yes → Snow/ice
No ↓

Cloud ? — Yes → Cloud

No ↓

$R'_{M1}>=0.4$ — Yes → Cloud
No →

$MeanR_{M7}>0.0$
$StdR_{M7}≤0.005$ &
$R_{M3} ≤0.30$ &
$R_1<2.0$
No

Yes ↓

$4.0K<BT_{M12}- BT_{M15}≤20k$

Yes →

$(BT_{M15}−BT_{M16}<0.1K$
$& -0.3≤NDVI≤0)$
or $R_1<1.5$
or $(BT_{M12}−BT_{M15}>8.6k$
$& BT_{M15}−BT_{M16}<0.1K)$ — Yes → Thin Dust

No ↓

$BT_{M15}−BT_{M16}<0.0$&
$BT_{M12}−BT_{M15}>20k$
&
$-0.3≤NDVI≤0.05$ — Yes → Thick dust

No

Uniformity test:
$StdR_{M11}>=0.008$ — Yes →

Cloud

No ↓

Update output for current pixel

Figure 16:   Detailed flow chart of IR-visible based dust detection over water
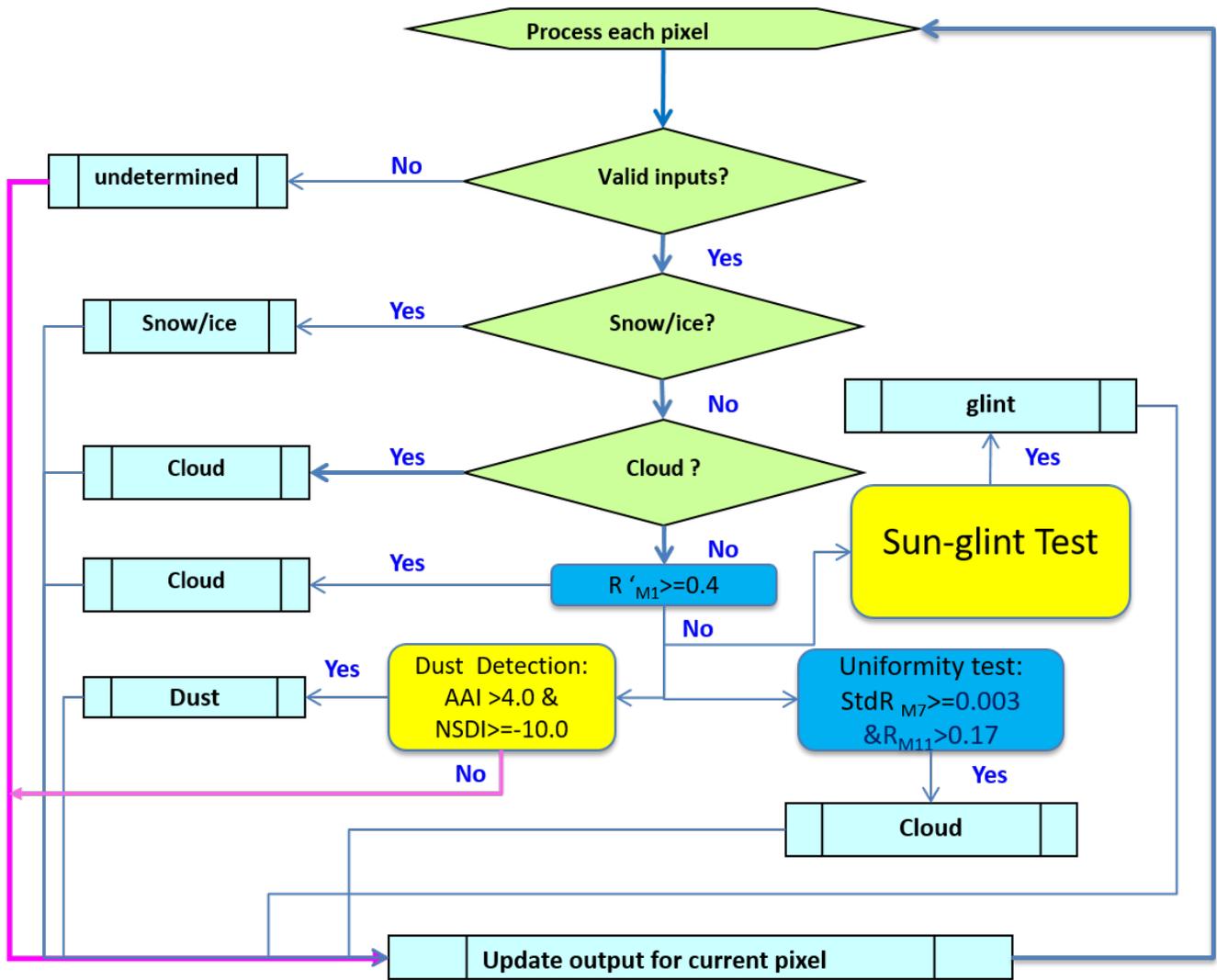
Figure 17: Detailed flow chart of Deep-blue based dust detection over water.

3.4.2.4 Dust Detection over Water

Dust detection over water has also two paths. If either path identifies the presence of dust, then dust is shown to be present in the product. The first path uses the same algorithm as the GOES-R Advanced Baseline Imager (ABI) to detect dust over land, which is based on the spectral variability tests in the visible bands and the negative brightness temperature difference between two wavelengths in IR regions; the second one is designed for VIIRS, by taking advantage of the VIIRS bands in the deep-blue range. The chosen path is determined by the availability of channels; if deep-blue channels (i.e., M1 and M2 for VIIRS) are not available, the algorithm takes the first path only. Otherwise, both paths are taken.

3.4.2.4.1   IR and visible-based dust detection

Figure 15 is a detailed flow chart of the IR-Visible path of the EPS ADP algorithm to detect the presence of dust over water during the daytime. The tests are not performed over snow and ice or in the presence of ice clouds.

The specific tests as currently implemented are:

1) Test for the presence of snow/ice by using both the primary snow/ice mask and internal sea/ice test, which is described in section 3.4.2.2. The test for the presence of clouds relies on the VIIRS cloud mask. A pixel is considered to be obscured by clouds if any one of the two cloud mask tests in Table 12, i.e., pCirrus1, pCirrus2 and pCirrus3, pFlag1 and pFlag2, is true or $R'_{M1} \geq 0.4$. Any pixel with positive snow/ice or clouds is not processed, and the corresponding snow/ice flag or cloud flag is set as 1.

2) Test for the quality of the input radiance data

    - R_{M3}, R_{M5}, $R_{M7} > 0.0$ &
    - BT_{M12}, BT_{M15}, $BT_{M16} > 0.0K$
    - VIIRS quality flags for the above channels equal to zero, indicating the quality of the data is assured.

3) Uniformity and spectral tests for residual clouds

    - $MeanR_{M7} > 0.0$ and $StdR_{M7} \leq 0.005$ &
    - $R_{M3} \leq 0.3$ &
    - $R_1 < 2.0$

      If all above tests passed, then proceed to dust detection. Otherwise, detection is stopped here and the dust flag is set as 0 and cloud flag is set as 1.

4) Tests for dust

    - If $4.0K < BT_{M12} - BT_{M15} \leq 20K$, then perform thin dust test
    - Otherwise, perform thick dust test

      4.1 thin dust test
       - If $BT_{M15} - BT_{M16} < 0.1K$ and $-0.3 \leq NDVI \leq 0$ or $R_1 < 1.5$ or $BT_{M12} - BT_{M15} > 8.6K$ and $BT_{M15} - BT_{M16} < 0.1K$, then thin dust (1), (2) and (3) is present

      4.2 thick dust test
       - If $BT_{M12} - BT_{M15} > 20K$ and $BT_{M15} - BT_{M16} \leq 0.0K$ and $-0.3 \leq NDVI \leq 0.05$, then thick dust is present

5) Set dust mask flag

3.4.2.4.2 Deep-blue based dust detection over water

Figure 16 is a detailed flow chart of the deep-blue path of the EPS ADP algorithm to detect the presence of dust over water during the daytime. The tests are not performed over snow and ice or in the presence of clouds.

The specific tests as currently implemented are:

1) Test for the presence of snow/ice by using the primary snow/ice mask, and if the primary is not available, then using the secondary snow/ice mask. The test for the presence of clouds relies on the VIIRS cloud mask and reflectance at M1. A pixel is considered to be obscured by clouds if any of these three cloud mask tests in Table 12, i.e. pCiirus1, pCirrus2 and pCirrus3, is true, or $R'_{M1} \geq 0.4$. Any pixel that tests positive for the presence of snow/ice or clouds is not processed, and the corresponding snow/ice flag or cloud flag is set as 1.

2) Test for the quality of the input radiance data

    - R_{M1}, R_{M2}, R_{M7}, R_{M11} > 0.0 &
    - VIIRS quality flags for the above channels equal to zero, indicating the quality of the data is assured.

3) Dust detection: AAI and DSDI tests – check for pixels with dust

    If AAI >4.0 and DSDI≥-10.0, dust exists for the pixel. Once dust is detected for the pixel, the dust flag is set and the value of the Scaled Absorbing Aerosol Index (SAAI), which is associated with the intensity of the dust, is obtained by scaling AAI as follows:

$$SAAI = AAI - 4.0 \tag{10}$$

4) Uniformity and spectral tests for residual clouds

    If $StdR_{M7}$≥0.003 and R_{M11}>0.17 then residual cloud exists and the pixel is assigned as cloudy.

3.4.2.4.3 Determination of quality and confidence flags

The approach to determine the quality flag with the confidence value is the similar to that described in section 3.4.2.3.3. Dust detection quality flags, which have a value of 1/2/0, are defined as low, medium

and high confidence, respectively. Determination of the level of confidence in the quality flag relies on several following steps:

A. If the pixel is masked as confident adjacent cloud or cloud shadow in the cloud mask, or is within sunglint, then the dust flag for this pixel is assigned a quality flag   value of 1, i.e., low confidence.

B. If the dust-detected pixel passed through step 1, then the confidence is further determined by the closeness of both AAI and DSDI to their thresholds. The details on how to calculate the confidence values for individual tests and the ensemble confidence value are given in section 3.4.2.3.3.

   a. For Deep-blue based dust detection as shown in section 3.4.2.3.2

    Test1: AAI > 4.0
    Test2: DSDI ≥ -10.0

    Intermediate confidence value (con_value$_a$) is calculated by averaging the con_value for Test1 and Test2 as follows:

$$\text{con\_value}_a = \frac{\text{con\_value(Test1)} + \text{con\_value(Test2)}}{2} \tag{11}$$

   b. For IR and visible-based dust detection shown in section 3.4.2.2.1

    1. Thin dust (1):

     Test 1: $BT_{M15} - BT_{M16} \leq 0.1K$
     Test 2: $-0.3 \leq NDVI \leq 0.0$
     Test 3: $BT_{M12} - BT_{M15} > 8.6k$

    Intermediate confidence value (con_value$_b$) is calculated by averaging the con_value for Test1 Test2, and Test3 as follows:

$$\text{con\_value}_b = \frac{\text{con\_value(test1)} + \text{con\_value(test2)} + \text{con\_value(test3)}}{3} \tag{12}$$

    2. Thin dust (2):

     Test 1: $4K < BT_{M12} - BT_{M15} \leq 20k$
     Test2: $R_1 < 1.5$

    Intermediate confidence value (con_value$_b$) is calculated by averaging the con_value for Test1 and Test2 as follows:

$$\text{con\_value}_b = \frac{\text{con\_value(test1)} + \text{con\_value(test2)}}{2} \qquad (13)$$

3. Thick Dust:

    Test1: $BT_{M15} - BT_{M16} \leq 0.0K$
    Test2: $BT_{M12} - BT_{M15} \geq 20K$
    Test3: $-0.3 \leq NDVI \leq 0.05$

Intermediate confidence value (con_value$_b$) is calculated by averaging the con_value for Test1 Test2, and Test3 as follows:

$$\text{con\_value}_b = \frac{\text{con\_value(test1)} + \text{con\_value(test2)} + \text{con\_value(test3)}}{3} \qquad (14)$$

C. Ensemble confidence

The ensemble confidence value is calculated by summing up con_value$_a$ and con_value$_b$. The final confidence level is set as low if the ensemble confidence value is ≤ 0.25; the confidence level is set as medium if the ensemble confidence value is > 0.25 but <0.50; and the confidence level is set as high if the ensemble confidence value is ≥0.50.

3.4.2.4.4   **Example results**

The results of an application of the JPSS EPS ADP algorithm to S-NPP VIIRS observations on February 1, 2015 at approximately 11:25 to 11:28 UTC is shown in Figure 17. The top panel is a RGB image. The image in the bottom panel shows the results of the dust detection over both and land and water, where orange and brown colors indicate the presence of dust. It is clearly seen that the RGB image and the JPSS EPS ADP dust mask image show qualitative agreement.
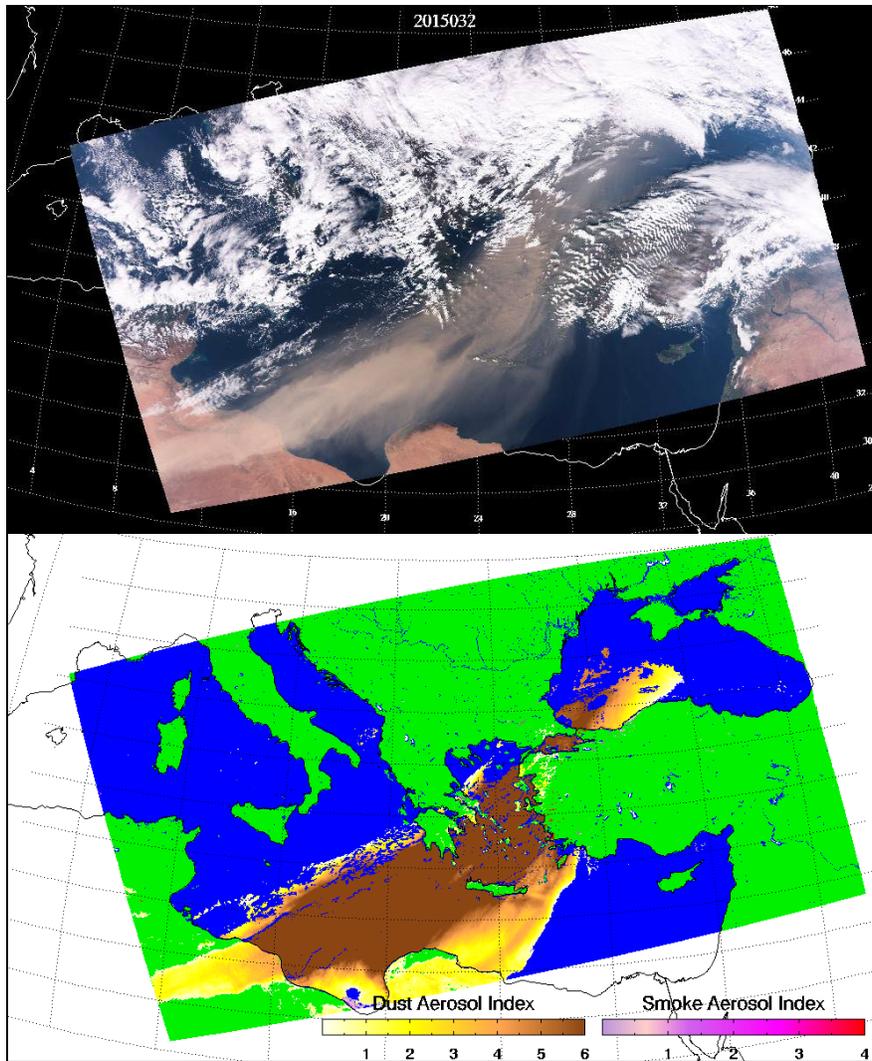
Figure 18: S-NPP VIIRS observations on Feb 1, 2015 at approximately 11:25 to 11:28 UTC. A dust plume is moving from the Sahara Desert over the adjacent Mediterranean Ocean.

3.4.2.5 Smoke Detection over Land

Smoke detection over land has two paths. If either path identifies the presence of smoke, then smoke is shown to be present in the product. The first path uses the same algorithm as the GOES-R Advanced Baseline Imager (ABI) to detect thick smoke, which is based on the spectral variability tests in the visible bands; the second one is designed for VIIRS, by taking advantage of the VIIRS bands in the deep-blue range. Figure 18 is a detailed flow chart of the first algorithm path to detect the presence of smoke over land during daytime. A detailed flow chart of the second algorithm path to detect the

presence of smoke over land during daytime is given in Figure 19. Note that the tests are not performed in the presence of snow/ice and ice clouds.
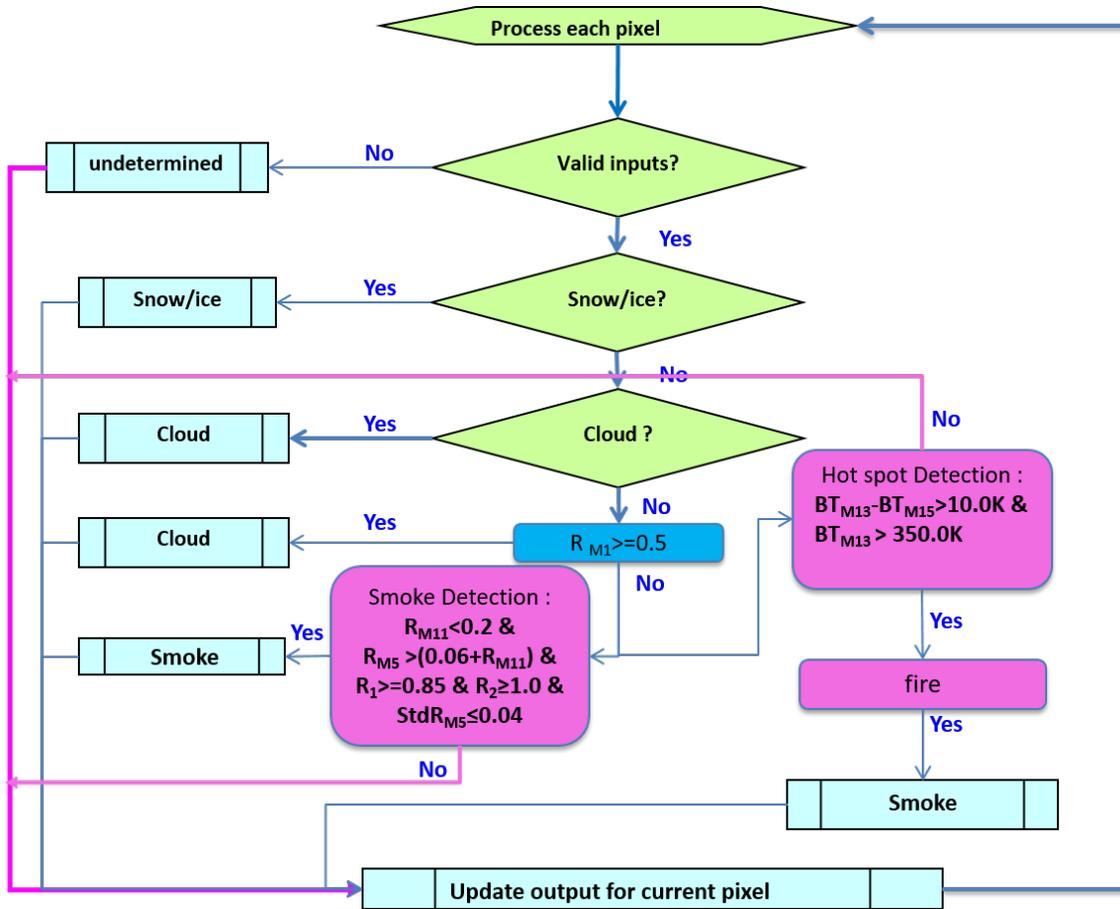
Figure 19: Detailed flow chart of IR-Visible based smoke detection over land.

3.4.2.5.1   IR-Visible based smoke detection

Figure 18 is a detailed flow chart of the IR-Visible path of the EPS ADP algorithm to detect the presence of smoke over land during daytime.

The specific tests as currently implemented sequentially are:

1) Test for the presence of snow/ice by using the primary snow/ice mask, and if the primary is not available, then by using the secondary snow/ice mask and also the internal snow/ice test. The test for the presence of clouds relies on the VIIRS cloud mask. A pixel is considered to be obscured by clouds if any of these five cloud mask tests in Table 10, i.e. pCiirus1, pCirrus2, pCirrus3, pFlag1 and, pFlag2, is true or $R'_{M1} \geq 0.4$.

Any pixel that tests positive for the presence of snow/ice/clouds is not processed, and the corresponding snow/ice flag or cloud flag is set as 1.

2) Test for the quality of the input reflectance data

- R_{M3}, R_{M5}, R_{M7}, R_{M11} > 0.0 &
- BT_{M13}, BT_{M15} > 0.0K
- VIIRS quality flags for the above channels equal to zero, indicating the quality of the data is assured.

3) Fire detection (hot spot)

Fire hot spots are determined by the combination of brightness temperature at M_{13} (BT_{M13}) and the brightness temperature difference between M_{13} and M_{15} ($BT_{M13} - BT_{M15}$). If BT_{M13} > 360K and $BT_{M13} - BT_{M15}$ > 10K, then the processed pixel is indicated as having a fire.

4) Spectral and uniformity tests for thick smoke
For detection of thick smoke, the following spectral contrast and uniformity tests are applied:

R_{M11} < 0.2
R_{M5} > (0.06 + R_{M11})
R_1 ≥ 0.85
R_2 ≥ 1.0
$StdR_{M5}$ ≤ 0.04

where R_{M11} and R_{M5} are reflectance at M_{11} and M_5, respectively. R_1 and R_2 are spectral contrast as defined in section 3.4.2. $StdR_{M5}$ is the standard deviation of R_{M5} in a 3 x 3 box centered with the processed pixel.
If all tests shown above are passed, thick smoke is detected for the processed pixel.

5) Set smoke flag

- If fire or thick smoke is indicated in the processed pixel, then thick smoke flag is set.
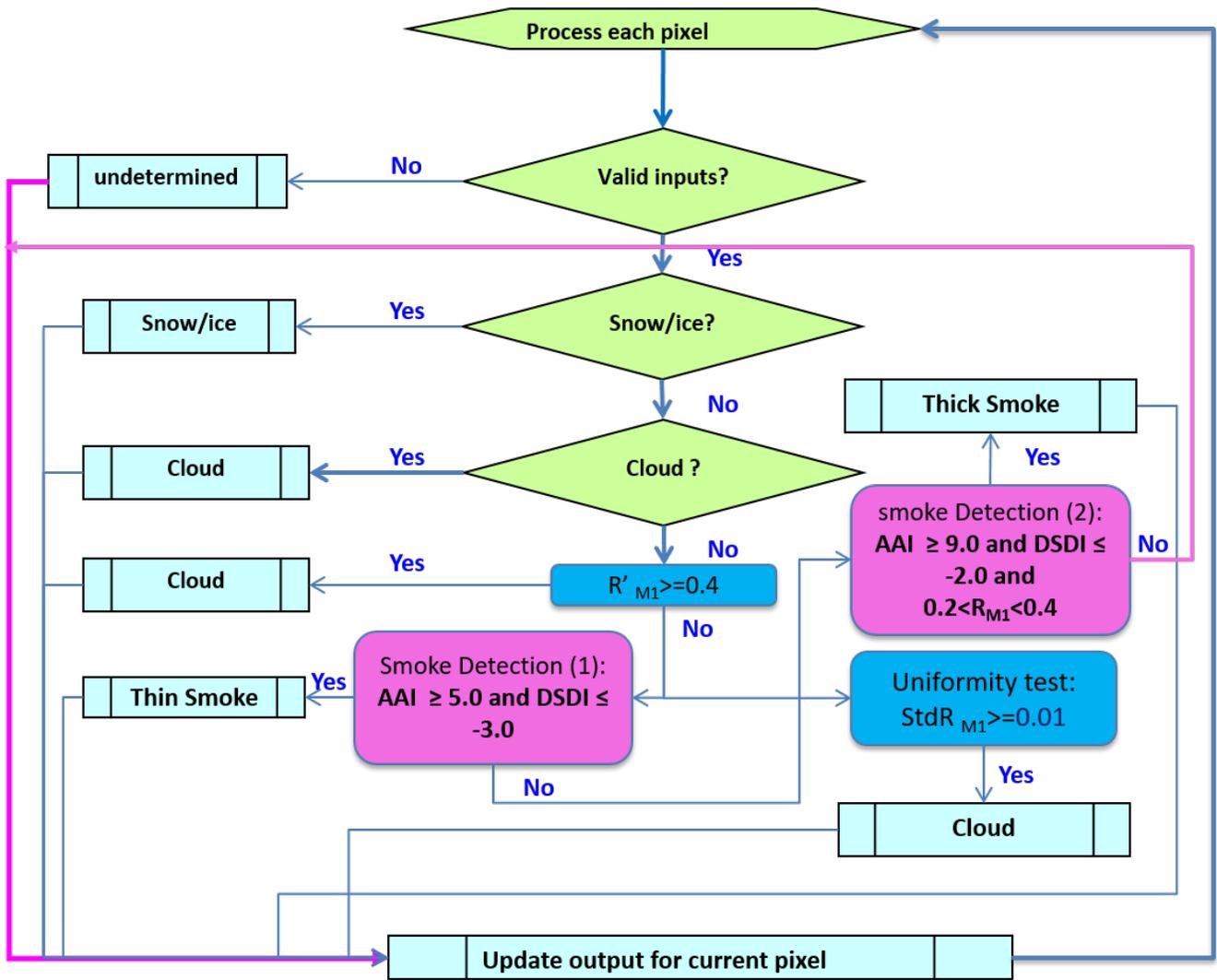
Figure 20: Detailed flow chart of Deep-blue based smoke detection over land

3.4.2.5.2 Deep-blue based smoke detection

Figure 19 is a detailed flow chart of the deep-blue path of the EPS ADP algorithm to detect the presence of smoke over land during daytime.

The specific tests as currently implemented are:

1) Test for the presence of snow/ice by using the primary snow/ice mask, and if the primary is not available, then by using the secondary snow/ice mask and also the internal snow/ice test. The test for the presence of clouds relies on the VIIRS cloud mask and reflectance measured by band M1. A pixel is considered to be obscured by clouds if any of these three cloud mask tests in Table 10, i.e. pCiirus1, pCirrus2 and pCirrus3, is true, or $R'_{M1} \geq 0.4$. Any pixel that tests positive for the

presence of snow/ice or clouds is not processed, and the corresponding snow/ice flag or cloud flag is set as 1.

2) Test for the quality of the input radiance data

- R_{M1}, R_{M2}, R_{M7}, R_{M11} > 0.0 &
- VIIRS quality flags for the above channels equal to zero, indicating the quality of the data is assured.

3) Smoke detection: AAI and DSDI tests – check for pixels with thin/thick dust

If AAI >5.0 and DSDI ≤-3.0, thin smoke exists for the processed pixel. However, If AAI >9.0 and DSDI ≤-2.0 and 0.2 <R_{M1}<0.4, then thick smoke exists for the processed pixel. Once smoke (either thin or thick) is detected for the pixel, the smoke flag is set and the value of the Scaled Absorbing Aerosol Index (SAAI), which is associated with the intensity of the smoke, is obtained by scaling AAI as follows:

$$SAAI = AAI - 5.0 \tag{15}$$

4) Uniformity and spectral tests for residual clouds

If the processed pixel is identified as having smoke from above steps, but $StdR_{M1}$≥0.01, then residual cloud exists and the processed pixel is assigned as cloudy.

5) Ephemeral water and dry river/lake bed screening

The ephemeral water test and dry river/lake bed test are applied as follows:

$$NDVI = \frac{(R'_{M7} - R'_{M5})}{(R'_{M7} + R'_{M5})}$$

- If $NDVI$<0.1 and R'_{M7}<0.1 then ephemeral water is present

$$NDWI = \frac{(R'_{M7} - R'_{M5})}{(R'_{M7} + R'_{M5})}$$

- If $NDWI$>0.25 then dry river/lake bed is present

In the presence of either ephemeral water or a dry river/lake bed, smoke detection is considered as not optimal. Therefore, the smoke flag is set as 0 but the NUC flag is set as 1.

3.4.2.5.3   Determination of quality and confidence flags

The approach to determine the quality flag with the confidence value is the similar to that described in section 3.4.2.3.3.   Smoke detection quality flags, with a value of 1/2/0, are defined as low, medium and high confidence, respectively. Determination of the level of confidence in the quality flag relies on several following steps:

1. If the pixel is masked as confident adjacent cloud or cloud shadow in the cloud mask, then the smoke flag for this pixel is assigned a quality flag value of 1, i.e., low confidence.

2. If the smoke-detected pixel passed through step 1, then the confidence is further determined by the closeness of tests to their threshold. The details on how to calculate the confidence values are given in section 3.4.23.3.

a. For Deep-blue based smoke detection as shown in section 3.4.2.3

   For thin smoke:

         Test1: AAI > 5.0
         Test2: DSDI ≤ -3.0

   For thick smoke:

         Test1: AAI > 9.0
         Test2: DSDI ≥ -2.0

   Intermediate confidence value (con_value$_a$) is calculated by averaging the con_value for Test1 and Test2 as follows:

   $$\text{con\_value}_a = \frac{\text{con\_value(Test1)} + \text{con\_value(Test2)}}{2} \tag{16}$$

b. For IR-Visible thick-smoke detection as shown in section 3.4.2.4.1

   1) Smoke from fire as shown in section 3.4.2.4

   Test1: BT_{M13} > 350K
   Test2: $BT_{M13} - BT_{M15}$ > 10K

   Intermediate confidence value (con_value$_b$) is calculated by averaging the con_value for Test1 and Test2 as follows:

   $$\text{con\_value}_b = \frac{\text{con\_value(Test1)} + \text{con\_value(Test2)}}{2} \tag{17}$$

   2) Thick smoke as shown in section 3.4.2.4

   Test1: R_{M11} < 0.2
   Test2: R_{M5} > (0.06 + $R_{2.25\mu m}$)
   Test3: R_1 ≥ 0.85

Test4: $R_2 \geq 1.0$

Intermediate confidence value (con_value$_b$) is calculated by averaging the con_value for Test1, Test2, Test3 and Test4 as follows:

$$\text{con\_value}_b = \frac{\text{con}_{value(Test1)} + \text{con}_{value(Test2)} + \text{con\_value}(Test3) + \text{con\_value}(Test4)}{4} \qquad (18)$$

c. Ensemble confidence

The ensemble confidence value is calculated by summing up con_value$_a$ and con_value$_b$. The final confidence level is set as low if the ensemble confidence value is $\leq$ 0.25; the confidence level is set as medium if the ensemble confidence value is > 0.25 but <0.50; and the confidence level is set as high if the ensemble confidence value is $\geq$0.50.

3.4.2.5.4   Example results

The result of an application of the smoke detection algorithm to S-NPP VIIRS observations on August 3, 2014 at 20:10 UTC is shown Figure 20. Smoke over the west cost of the U.S. is detected. Comparison of the smoke mask to RGB images shows that smoke over land was well captured.
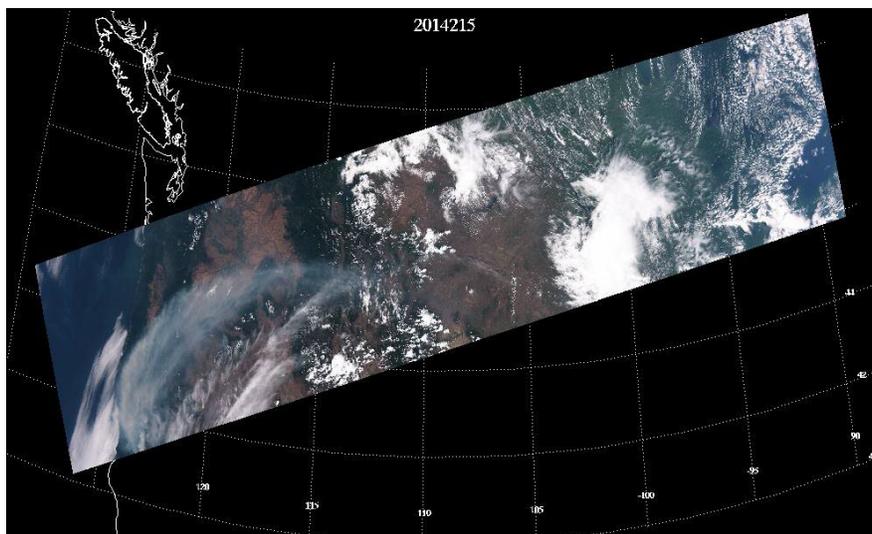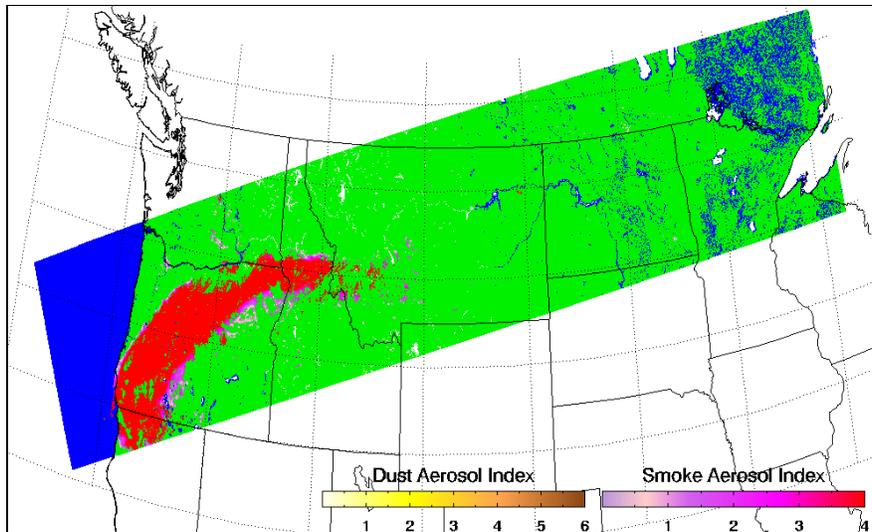
Figure 21: Top: a red-green-blue (RGB) false color image of S-NPP VIIRS observation data on August 3, 2014 at approximate 20:10 UTC. Bottom: the results of the smoke detection where pixels flagged as smoky are pink to red.

3.4.2.6 Smoke detection over water

Smoke detection over water has two paths. If either path identifies the presence of smoke, then smoke is shown to be present in the product. The first path uses the same algorithm as the GOES-R Advanced Baseline Imager (ABI) to detect thick smoke, which is based on the spectral variability test in the visible bands; the second one is designed for VIIRS, by taking advantage of the VIIRS bands in the deep-blue range. Figure 21 is a detailed flow chart of the first algorithm path to detect the presence of smoke over water during daytime. A detailed flow chart of the second algorithm path to detect the presence of smoke over water during daytime is given in Figure 22. Note that the tests are not performed in the presence of snow/ice and ice clouds.
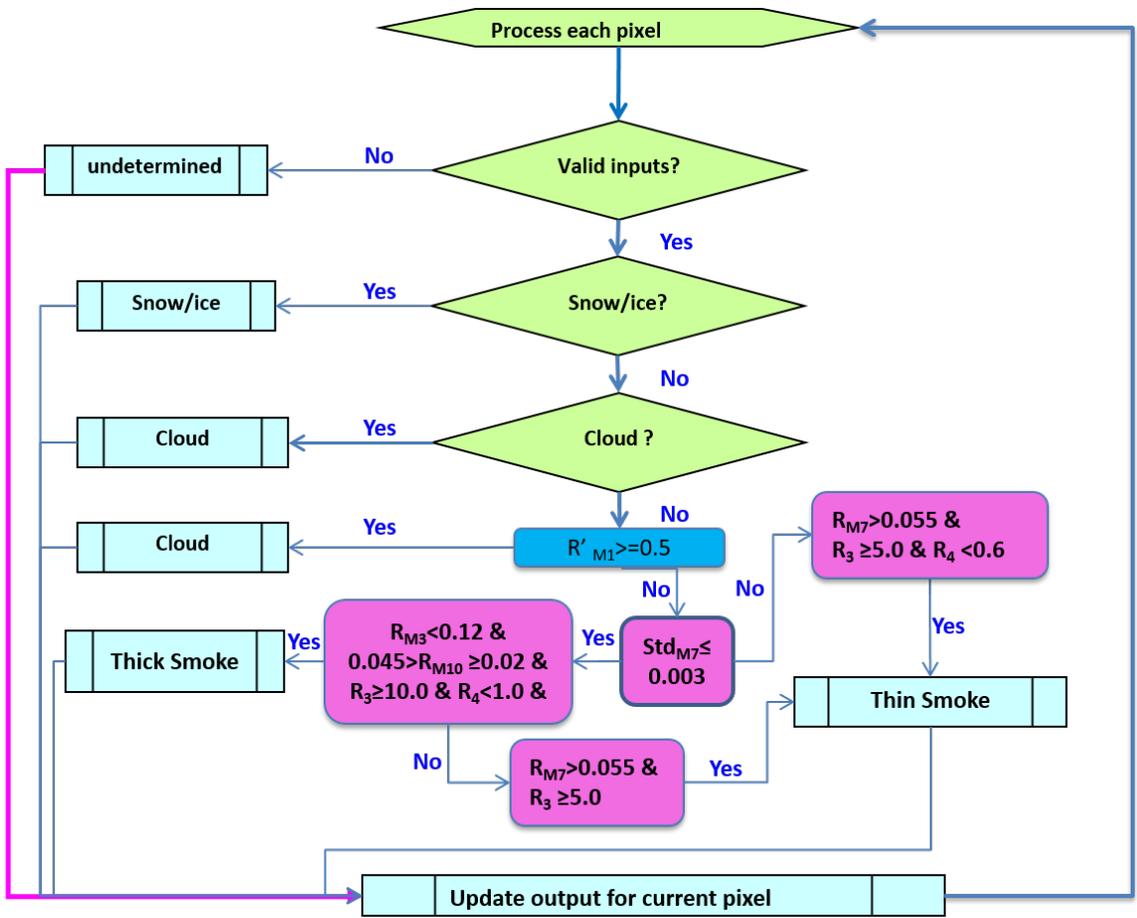
Figure 22: Detailed flow chart of IR-Visible based smoke detection over water.
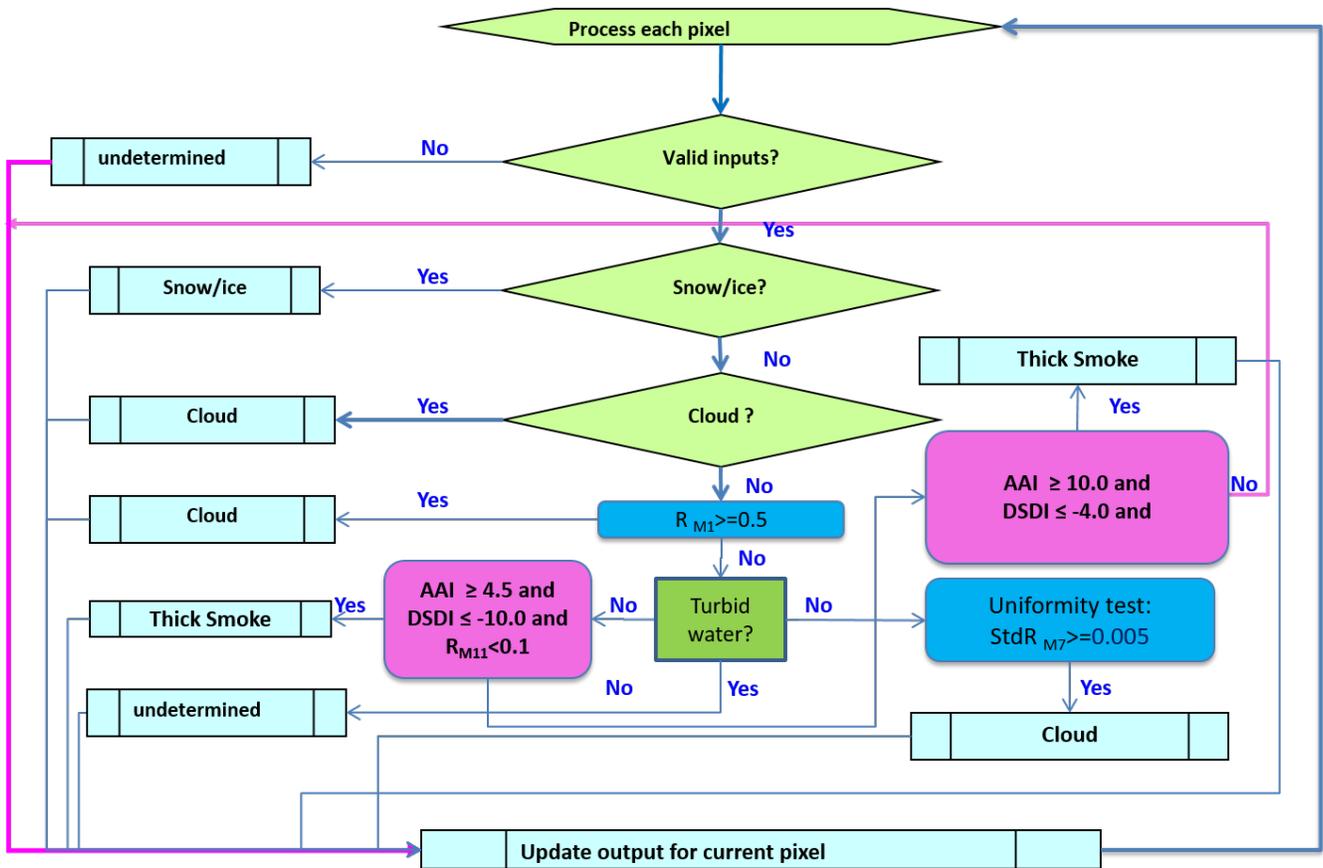
Figure 23: Detailed flow chart of Deep-blue based smoke detection over water.

3.4.2.6.1   IR-Visible based Smoke detection

Figure 21 is a detailed flow chart of the IR-Visible path of the EPS ADP algorithm to detect the presence of smoke over water during daytime.

The specific tests as currently implemented sequentially are:

1) Test for the presence of snow/ice by using the primary snow/ice mask, and if the primary is not available, then by using the secondary snow/ice mask, and also the internal sea ice test. The test for the presence of clouds relies on the VIIRS cloud mask. A pixel is considered to be obscured by clouds if any of these four cloud mask tests in Table 10, i.e. pCiirus1, pCirrus2, pCirrus3 and pFlag1, is true or $R'_{M1} \geq 0.4$. Any pixel with a positive snow/ice/cloud mask is not processed, and the corresponding snow/ice flag or cloud flag is set as 1.

2)   Test for the quality of the input radiance data

- $R_{M3}, R_{M7}, R_{M10}, R_{M11} > 0.0$
- VIIRS quality flags for the above channels equal to zero, indicating the quality of the data is assured.

3) Uniformity test

A uniformity test with $StdR_{M7}$ is first performed to decide the detection path. If $StdR_{M7}$ ≤0.003, a thick smoke determination test is performed. Otherwise, a thin smoke determination test is performed.

3.1) Thick smoke determination test

Thick smoke is detected for the processed pixel if the all of the following tests are passed:

- R_3 ≥10.0
- R_{M3} ≥0.12
- $0.02 \leq R_{M10} < 0.045$
- $R_4 < 1.0$

where R_{M2} and R_{M11} are respectively the reflectance at M2 and M11, R_3 and R_4 are spectral contrast as defined in section 3.4.2.

If above tests are not passed, then further tests are performed; thin smoke is identified if the all of the following tests are passed:

- $R_{M7} > 0.055$
- $R_3 \geq 5.0$

where R_{M7} is the reflectance at M7, R_3 is spectral contrast as defined in section 3.4.2.

3.2) Thin smoke determination test

Thin smoke is detected for the processed pixel if the all of the following tests are passed:

- $R_{M7} > 0.055$
- R_3 ≥5.0
- $R_4 < 0.6$

where R_{M7} is the reflectance at M$_7$, R_3 and R_4 are spectral contrast as defined in section 3.4.2.

4) Set smoke flag

If either thin or thick smoke is detected for the processed pixel, then the smoke flag is set as 1.

3.4.2.6.2 Deep-blue based smoke detection over water

Figure 22 is a detailed flow chart of the deep-blue path of the EPS ADP algorithm to detect the presence of smoke over water during daytime.

The specific tests as currently implemented are:

1) Test for the presence of snow/ice by using the primary snow/ice mask, and if the primary is not available, then by using the secondary snow/ice mask, and also the internal sea ice test. The test for the presence of clouds relies on the VIIRS cloud mask and reflectance measured by band M$_1$ (R_{M1}) A pixel is considered to be obscured by clouds if any of these three cloud mask tests in Table 10, i.e. pCiirus1, pCirrus2 and pCirrus3, is true, or $R'_{M1} \geq 0.4$. Any pixel that tests positive for the presence of snow/ice or clouds is not processed, and the corresponding snow/ice flag or cloud flag is set as 1.

2) Test for the quality of the input radiance data

- R$_{M1}$, R$_{M2}$, R$_{M7}$, R$_{M11}$ > 0.0 &

- VIIRS quality flags for the above channels equal to zero, indicating the quality of the data is assured.

3) Turbid/shallow water and algae bloom test

The MODIS heritage turbid/shallow water test described in Li et al. (2003) is used to identify turbid water containing suspended sediments and also to identify shallow water, for which smoke detection will not be carried out to reduce the incidence of false alarms. The sediment masking algorithm uses the observed reflectances at M3, M8, M10, and M11 to derive the power law fit using least squares minimization. The computed reflectances (R$'_{M4}$) at M4 based on the power law fit are then compared with the observed reflectances (R$_{M4}$) at the same band. The specific criteria to trigger that the pixel is affected by turbid water are:

- $R_{M4} - R'_{M4} > 0.015$
- $R_{M3} < 0.25$ (19)

- $R_{M11} < 0.10$

In addition, for water surfaces, phytoplankton blooms will be mis-identified as smoke by the Deep-blue based smoke detection algorithm. To eliminate this false alarm, smoke detection will not be carried out for any pixels which have phytoplankton blooms. To determine if a pixel contains a phytoplankton bloom, an index (*SABI*), which is defined as follows, is used:

$$SABI = \frac{R_{M4} - R_{M5}}{R_{M4} + R_{M7}} \tag{20}$$

Any pixel with an *SABI* value larger than 0.28 is considered as having a phytoplankton bloom.

4) Smoke detection: AAI and DSDI tests – check for pixels with thin/thick dust

If AAI >4.5, DSDI≤-10.0 and R_{M11}<0.1, thin smoke exists in the processed pixel. However, If AAI >10.0 and DSDI≤-4.0, thick smoke exists in the processed pixel. Once smoke (either thin or thick) is detected for the pixel, the smoke flag is set and the value of the Scaled Absorbing Aerosol Index (SAAI), which is associated with the intensity of the smoke, is obtained by scaling AAI as follows:

$$SAAI = AAI - 4.5 \tag{21}$$

5) Uniformity and spectral tests for residual clouds

If the processed pixel is identified as having smoke from above steps, but *StdR_{M7}*≥0.005, then residual cloud exists and the processed pixel is assigned as cloudy.

3.4.2.6.3   Determination of quality and confidence flags

The approach to determine the quality flag with the confidence value is the similar to that described in section 3.4.2.3.3.   Smoke detection quality flags (1/2/0) are defined as low, medium and high confidence, respectively. Determination of the level of confidence in the quality flag relies on several following steps:

1. If the pixel is masked as confident adjacent cloud or cloud shadow in the cloud mask, then the smoke flag for this pixel is assigned a quality flag value of 1, i.e., low confidence.

2. If the smoke-detected pixel passed through step 1, then the is further determined by the closeness of tests to their threshold. The details on how to calculate the confidence values are given in section 3.4.2.3.3.

a. For Deep-blue based smoke detection as shown in section 3.4.2.5.2.
   For thin smoke:

Test1: AAI > 4.5
Test2: DSDI ≤ -10.0

For thick smoke:

Test1: AAI > 10.0
Test2: DSDI ≤ -4.0

Intermediate confidence value (con_value$_a$) is calculated by averaging the con_value for Test1 and Test2 as follows:

$$\text{con\_value}_a = \frac{\text{con\_value(Test1)} + \text{con\_value(Test2)}}{2} \tag{22}$$

b. For IR-Visible based smoke detection as shown in section 3.4.2.5.1

1) Thin Smoke (1) as shown in section 3.4.2.5.1

Test1: $R_3 \geq 5.0$

Intermediate confidence value (con_value$_b$) is equal to Con_value of Test1.

2) Thin Smoke (2) as shown in section 3.4.2.5.1

Test1: $R_3 \geq 5.0$
Test2: $R_4 < 0.6$

Intermediate confidence value (con_value$_b$) is calculated by averaging the con_value for Test1 and Test2 as follows:

$$\text{con\_value}_b = \frac{\text{con\_value(Test1)} + \text{con\_value(Test2)}}{2} \tag{23}$$

3) Thick smoke (3) as shown in section 3.4.2.5.1

Test1: $R_3 \geq 10.0$
Test2: $R_{M3} \geq 0.12$
Test3: $0.02 \leq R_{M9} < 0.45$
Test4: $R_4 < 1.0$

Intermediate confidence value (con_value$_b$) is calculated by averaging the con_value for Test1, Test2, Test3 and Test4 as follows:

$$\text{con\_value}_b = \frac{\text{con}_{\text{value(Test1)}} + \text{con}_{\text{value(Test2)}} + \text{con\_value(Test3)} + \text{con\_value(Test4)}}{4} \qquad (24)$$

c. Ensemble confidence

The ensemble confidence value is calculated by summing up con_value$_a$ and con_value$_b$. Then, the confidence level for the quality flag is set as low if the ensemble confidence value is ≤ 0.25; the confidence level is set as medium if the ensemble confidence value is > 0.25 but <0.50; the confidence level is set as high if the ensemble confidence value is ≥0.50.

3.4.2.6.4 Example results

The results of an application of the JPSS EPS ADP algorithm to S-NPP VIIRS data on July 11, 2015 at approximately 13:00 UTC is shown in Figure 23. Smoke stretched from the east coast of Greenland to the central Atlantic Ocean, as   shown in the RGB image. This ribbon of smoke aloft originated from forest fires over Russia and was transported eastward across the North Atlantic Ocean by the circulation of a large area of low pressure on July 17. The leading edge of the smoke had moved over the British Isles and was headed toward Scandinavia. It is clear seen that the detected coverage of the smoke is very similar to the pattern that observed from the RGB image, indicating the success of EPS ADP algorithm.
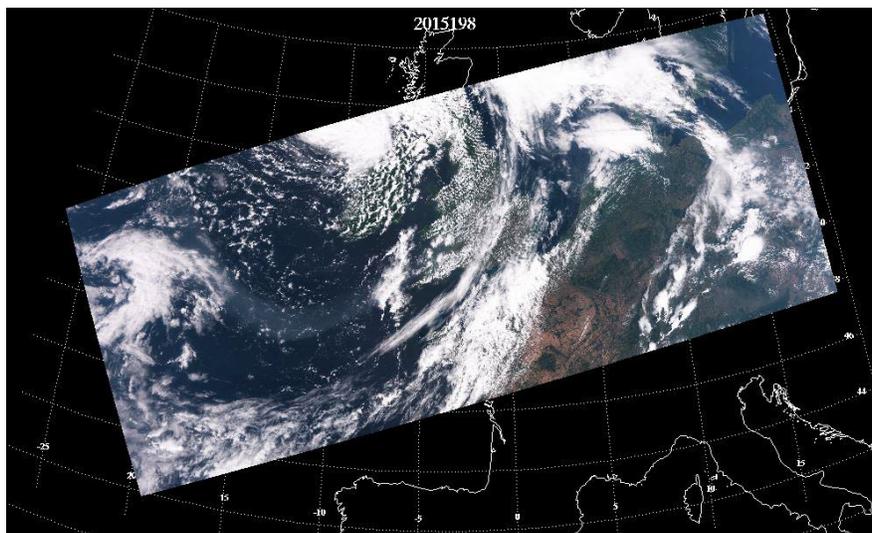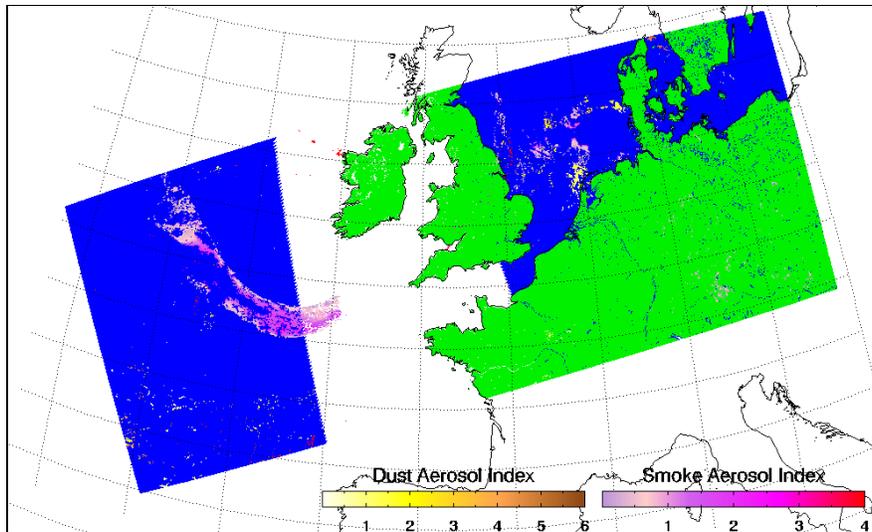
Figure 24: Top: a red-green-blue (RGB) false color image of S-NPP VIIRS observations on July 11, 2015 at approximately 12:58 UTC. Bottom: the results of EPS ADP algorithm.

3.4.3 Noise reduction in smoke/dust detection

Smoke/dust events are usually larger than several ABI pixels. To reduce noise that can occur from detection of smoke or dust in a single pixel, "buddy" checks are applied after the steps described in the previous sections. For smoke pixels, the buddy check is performed for surrounding pixels in a 3 x 3 box. If the number of pixels detected as smoke in this box is < 5, then the detected smoke is considered noise, and the corresponding smoke flag is reversed from 1 to 0, and the corresponding confidence flag is changed to as a default value, i.e., 0. The same buddy check procedure is applied to dust pixels which are identified as dust.

In addition, to reduce the contamination from pixels which contain melting snow/ice or are covered partially by snow/ice, and are thus usually missed by the snow/ice mask, snow/ice adjacency tests are performed. These tests are performed for all pixels identified as snow/ice by the snow/ice mask. If a pixel is identified as snow/ice by the snow/ice mask, then the smoke/dust flag in all surrounding pixels in a 3 x 3 box is set to 0, and the corresponding confidence flags are set to the default value of 0.

3.4.4 Algorithm Output

The final output of the EPS ADP algorithm includes a binary (yes/no) detection mask for smoke, dust, volcanic ash (currently is set as 0), clouds, snow/ice and none/unknown/clear (NUC), and values for Scaled Absorbing Aerosol Index (SAAI) for smoke/dust, Dust smoke Discrimination Index (DSDI) and smoke concentration (currently as filled value). The full set of output variables are listed in Table 2, and the corresponding data quality flags as shown in Table 3.

4 TEST DATASETS AND OUTPUTS

4.1 Proxy Input Data Sets and validation data

4.1.1 Input Data sets

The VIIRS instrument flying on NASA's Suomi-NPP satellites measures radiances at 16 wavelengths including infrared and visible bands with a spatial resolution of 750m at nadir. The cloud mask is part of the Suomi-NPP Cloud Product [*Ackerman et al.*, 1998, 2008; *Frey et al.*, 2008; *King et al.*, 2003; *Platnick et al.*, 2003]. Due to the fact that Suomi-NPP VIIRS is identical to JPSS-VIIRS, currently S-NPP VIIRS provides the optimum source of data for testing. tThe channels of Suomi-NPP VIIRS and those used in the JPSS VIIRS EPS ADP algorithm are listed in Table 8.

S-NPP VIIRS Sensor Data Record (SDR) data, VIIRS cloud mask product, and Terrain Corrected Geolocation (GMTCO) were obtained from the NASA Atmosphere Product and Evaluation and Test Element (PEATE) hosted at the Space Science and Engineering Center (SSEC) of the University of Wisconsin (http://peate.ssec.wisc.edu/). The corresponding required inputs for JPSS ADP, which are listed in Table 8, are derived from these data. The Visible channel reflectances and Brightness Temperatures for the IR channels were obtained from SDR data. Viewing and illumination geometry and geo-location were from GMTCO. Various cloud tests used in ADP were extracted from the corresponding bits in the VIIRS Enterprise cloud mask product (ECM). The snow/ice mask from ECM was used as the primary source of snow/ice mask. The land/water mask was also from ECM. Both the sun glint mask and day/night flag were internally calculated as described in section 3.12.

4.1.2 Truth data

4.1.2.1 Supervised S-NPP VIIRS RGB image and VIIRS Aerosol Optical Depth Product

Both smoke and dust have a distinctive signature in RGB images, and the NASA Natural Hazard system (http://earthobservatory.nasa.gov/NaturalHazards/) and the MODIS rapid response system (http://rapidfire.sci.gsfc.nasa.gov/gallery/) routinely issue MODIS observations containing smoke and dust outbreaks around the globe. By selecting VIIRS granules which are dominated by either only smoke or only dust, a supervised truth dataset was obtained. Then the corresponding Aerosol Optical Depth (AOD) product was used to identify the smoke/dust laden (AOD>0.2) and smoke/dust free (0.2>AOD>0.0) pixels. VIIRS pixels with no AOD retrievals were considered to be covered by clouds or snow/ice, bright surface over land or bad input data. These conditions are consistently unfavorable for detection of smoke/dust as well, as discussed in Section 3. In addition, due to the difference in cloud screening procedures between the VIIRS AOD product and JPSS EPS ADP algorithm, only pixels with both VIIRS AOD and JPSS ADP indicating cloud-free conditions were used for quantitative analysis.

4.1.2.2 Aerosol Robotic Network (AERONET) observations

The ground-based remote sensing network, AEROsol Robotic Network (AERONET), equipped with well-calibrated sunphotometers at over more than 100 sites throughout the world, measures and derives

quality-assured aerosol optical properties for a wide diversity of aerosol regimes, for up to the last 10 years [Holben et al., 1998; 2001; Dubovik et al., 2002]. These high quality data have been widely used as ground "truth" for evaluation and validation of satellite remote sensing of aerosols [Yu et al., 2003; Remer et al., 2005]. Observations from AERONET are be the primary source of in situ ground truth for ADP, since the stratification of Angstrom Exponent data from AERONET indicates the presence of smoke or dust particles in the atmosphere. However, the Angstrom Exponent used as a proxy for aerosol particle size parameter has a limited ability to separate different types of aerosols. At best it can provide a clean separation of dust and smoke but not haze and smoke (see Figure 24).
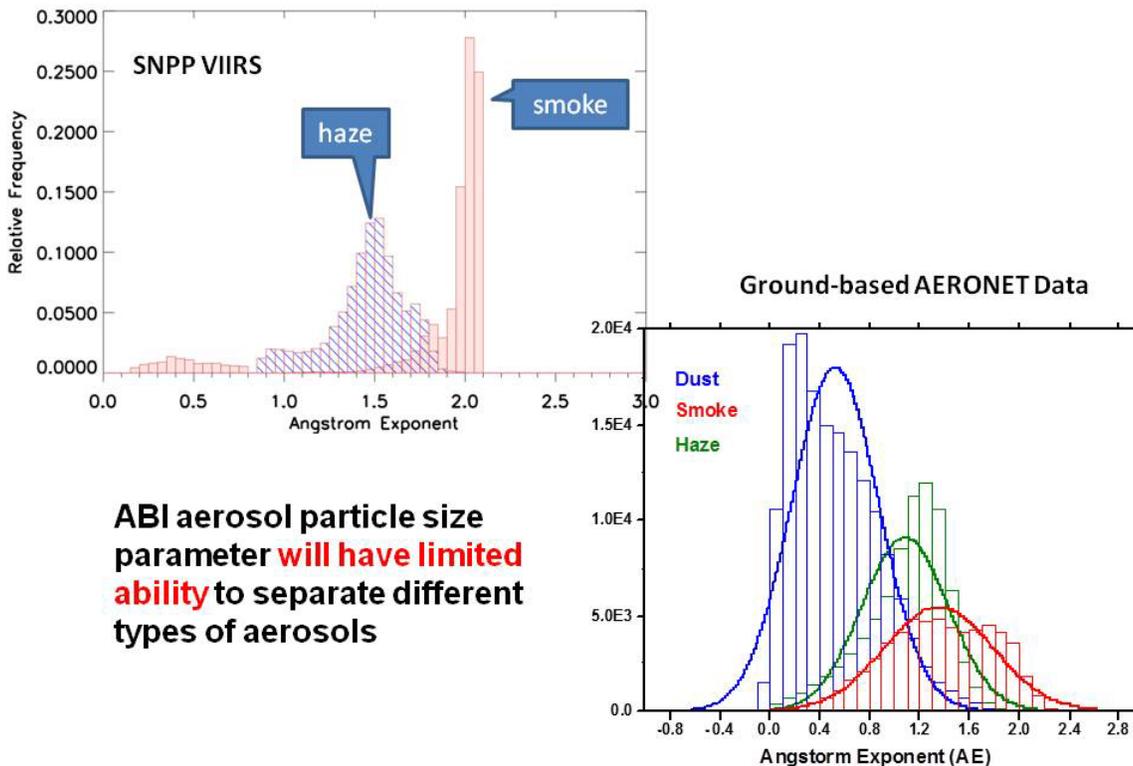
Figure 25 : Top: histogram of Angstrom Exponent (AE) for pixels with smoke and haze in S-NPP VIIRS observations. Bottom: histogram of Angstrom Exponent (AE) for smoke, dust and haze from AERONET observations.

The matchup strategies are as follows:
- Collocated AERONET and JPSS VIIRS ADP smoke/dust detection results
    – Spatial coverage: a circle with a radius of 25 km and centered on AERONET stations are chosen to determine the dominant Aerosol type from JPSS ADP.
    – Temporal average: AERONET measurements within a 30 minute   window centered on the NPP VIIRS overpass time, at least three measurements are available.
- Dominant Aerosol type from JPSS ADP
    – 80% of pixels in the circle are cloud, snow/ice and glint-free (for over water)

- The type of more than half the valid retrievals was chosen as the dominant type from JPSS ADP.
- Classification of Aerosol Type over AERONET:
  - Smoke:
  AOD>0.3 and AE>1.1
  - Dust:
  AOD>0.3 and AE<0.6

4.1.2.3 CALIPSO VFM product

With the launch of CALIPSO and CloudSat in the EOS A-Train formation in April 2006, the ability to conduct global satellite cloud product validation increased significantly. Besides cloud type, CALIPSO also identifies aerosol types including smoke and dust. Vertical Feature Mask (VFM) is the CALIPSO product which is used for validating VIIRS ADP. It gives not only vertical distribution of aerosol layers but also 6 types of aerosol, including clean marine, dust, polluted dust, polluted continental, clean continental, polluted dust and smoke. However, the sparse spatial coverage and narrow swath of CALIPSO LIDAR observation limits the amount of match-up overpasses with VIIRS for smoke and dust cases.
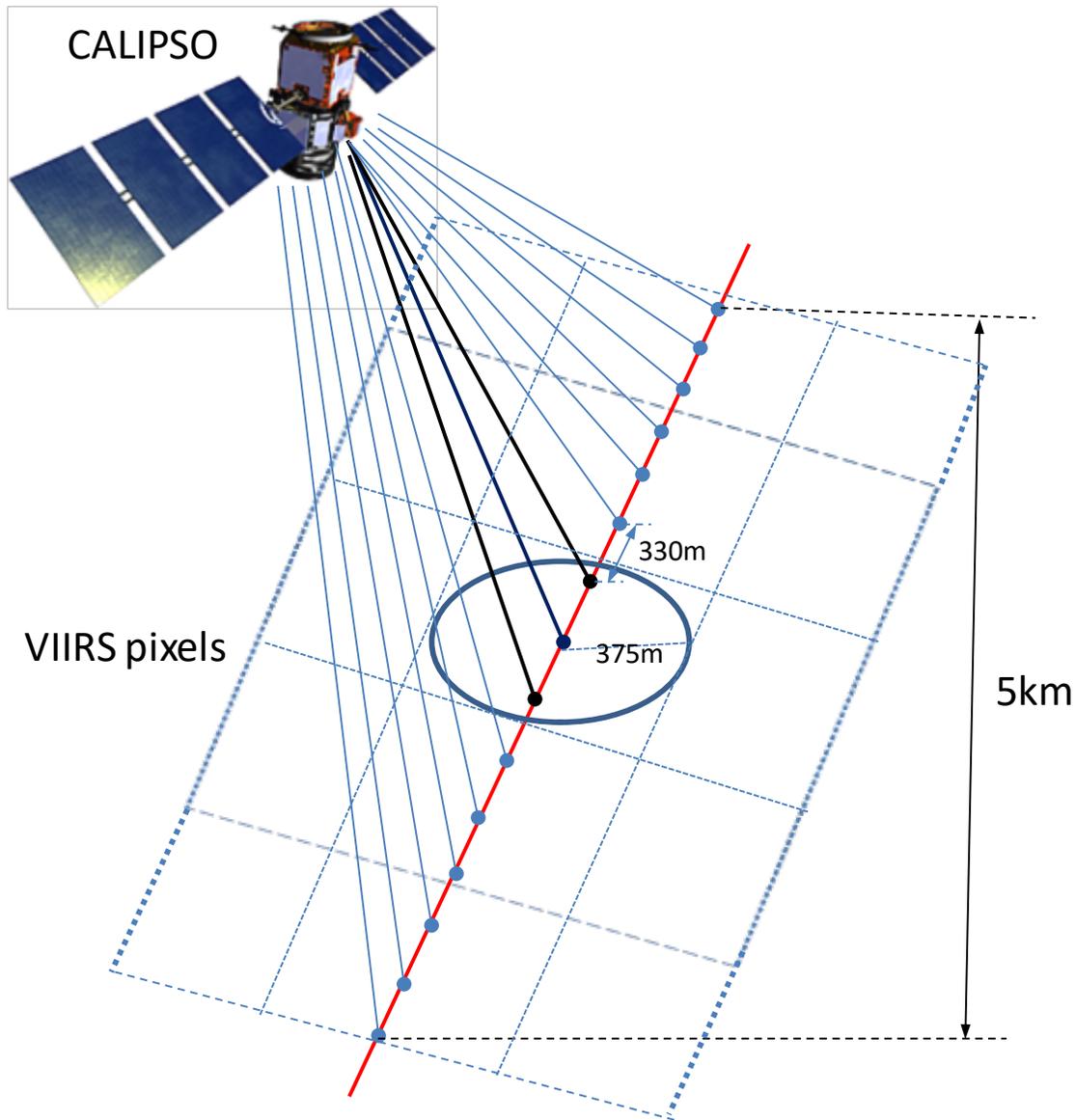
Figure 26: Schematic illustration of matchups between S-NPP VIIRS and CALISPO-VFM product.

The matchup strategies are as follows:

- Time difference: ±30 minutes within the starting time of each CALIPSO VFM track.
- Spatially, the VIIRS pixel that is within ± 375m of the location of the middle profile (i.e., 8th profile) in each 5km trunk of the CALIPSO VFM product is selected, then a box of 5 x 5 pixels, for a total of 25 pixels, centered over the selected pixel, is matched.
- Aerosol Types in CALIPSO VFM are grouped as :
    - a. dust (including polluted dust)
    - b. smoke
    - c. cloudy
    - d. clear
    - f. others

- Aerosol Types in JPSS VIIRS ADP are grouped in 5 x 5 box as :
  - a. dust
  - b. smoke
  - c. cloudy
  - d. Unknown/None/Clear
- Determination the dominant Aerosol type in CALIPSO VFM

  For each 5 km trunk of CALIPSO VFM, which consists of 15 profiles, the dominant aerosol type for each profile is first determined through the calculation of dust (smoke and others) fraction i.e., number of dust (smoke and others) layers divided by the number of aerosol layers from the surface to 20.2 km. For profiles without clouds at any layer, any aerosol type that has a fraction larger than 80% is defined as the dominant type. If all three are less than 80%, then the dominant type is defined as "others". If clouds exist in any layer, this profile is defined as "cloudy". Otherwise, this profile is defined as "clear". The ensemble Aerosol type for each 5km trunk is further determined as: dust if 12 out of 15 profiles are dust, as smoke if 12 out of 15 profiles are dust, as others if not smoke or dust, as cloudy if any one of 15 profiles is cloudy or as clear if all of 15 profiles are clear.

- Quality Control
    Medium to high quality used

4.2 Output from proxy data sets

4.2.1 Output for Dust Detection

4.2.1.1 Comparison with RGB image and AOT product

Supervised RGB images can capture dust events very well since dust plumes look bright and brown in the image compared to cloud. Thus, RGB images can be used to validate the ADP dust detection algorithm qualitatively. Therefore, we can apply the dust detection algorithm to S-NPP VIIRS measurements of a dust event and compare the detection result with the VIIRS RGB image. One example is shown in Figure 26 for the NPP VIIRS observations on April 5, 2015 at around 09:59 UTC. Qualitative comparison of dust detection with the VIIRS RGB image shows good agreement.
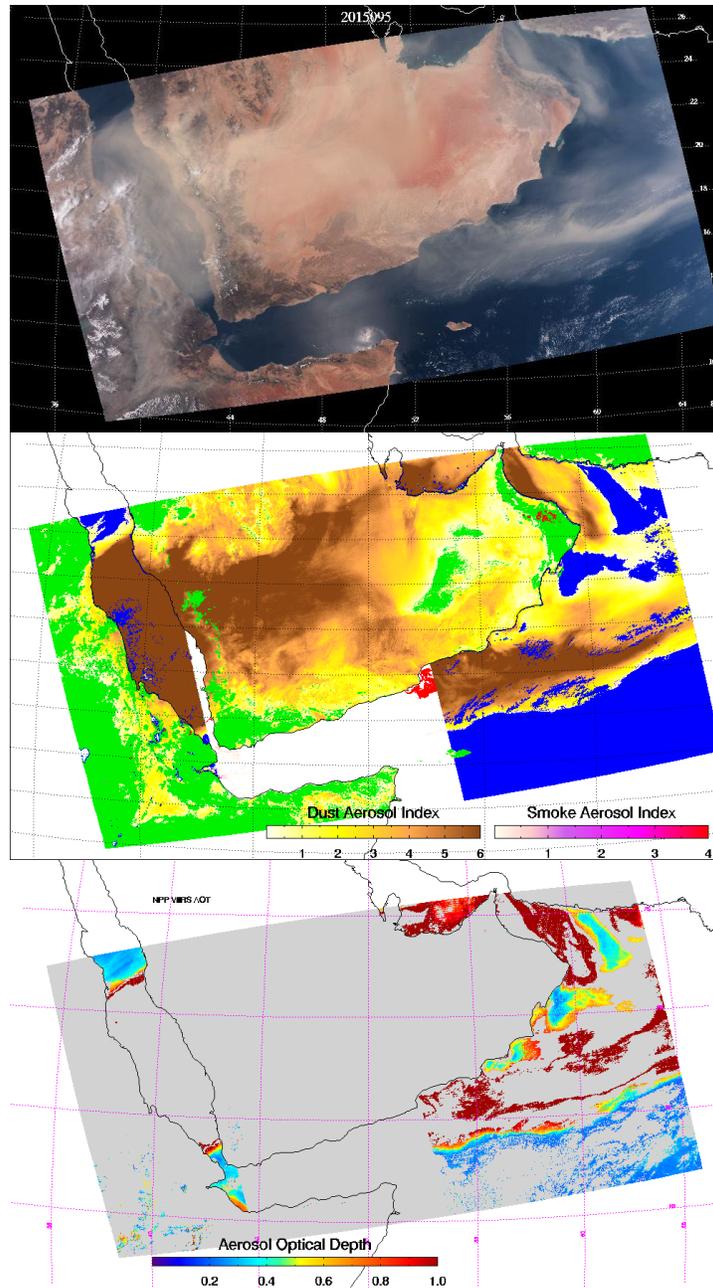
Figure 27: TOP: S-NPP VIIRS RGB Image on April 5, 2015 at about 09:59 UTC. Middle: the results of the dust detection from JPSS ADP. Bottom: S-NPP VIIRS AOD (only pixels with AOD > 0.2 are shown)

Dust particles are mainly located near and downwind of desert regions and a dust event is mainly associated with high aerosol optical depth (AOD,) so the AOD distribution retrieved from satellite observations can help us to qualitatively examine the ADP dust detection algorithm.

4.2.1.2 Comparison with CALIPSO VFM

CALIPSO is onboard the same spacecraft as MODIS Aqua, which has the same afternoon overpass time as S-NPP VIIRS, and its VFM products provide the vertical distribution of 6 aerosol types, including smoke and dust, over its narrow (a footprint with a 70m diameter) track. Although the sparse spatial coverage of CALIPSO LIDAR observations limits the number of overpass matchups with S-NPP VIIRS granules over the whole globe during the time period of 2.5 years (from 2012 to June of 2015), many cases containing dust outbreaks were found. And the possibility of using the S-NPP VIIRS and CALIPSO overpass and the CALIPSO aerosol type data to validate the dust detection in JPSS ADP is explored.
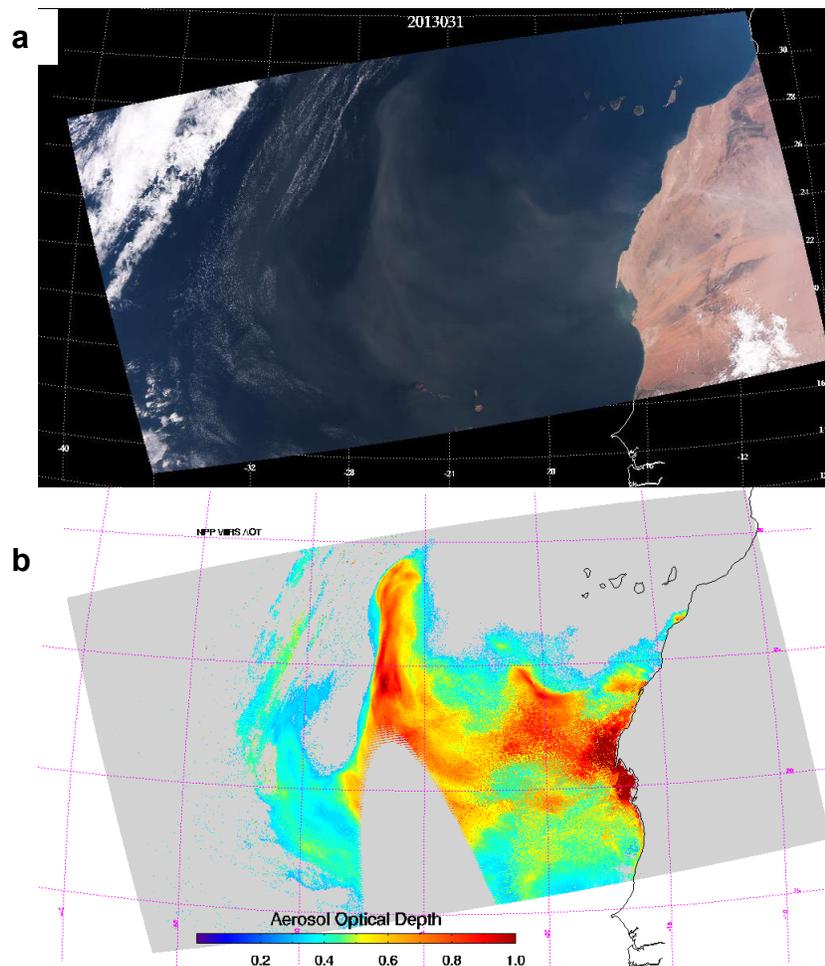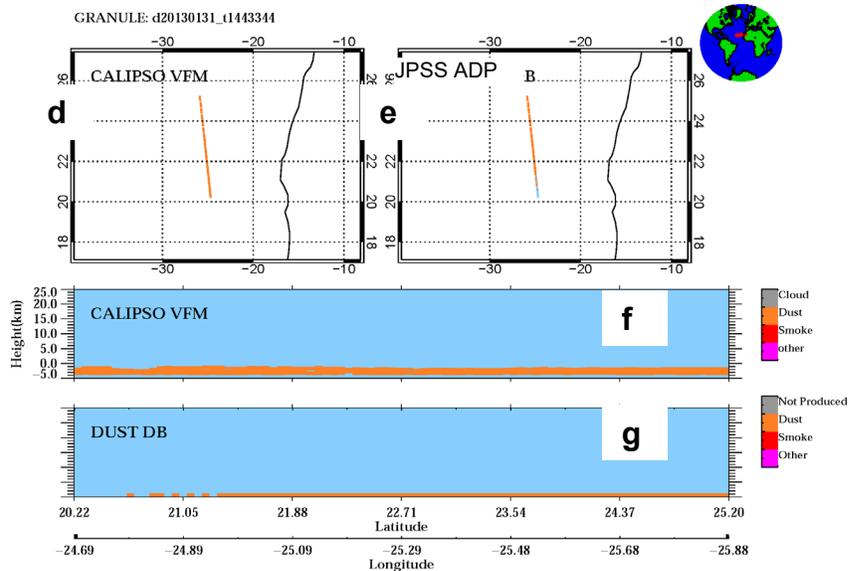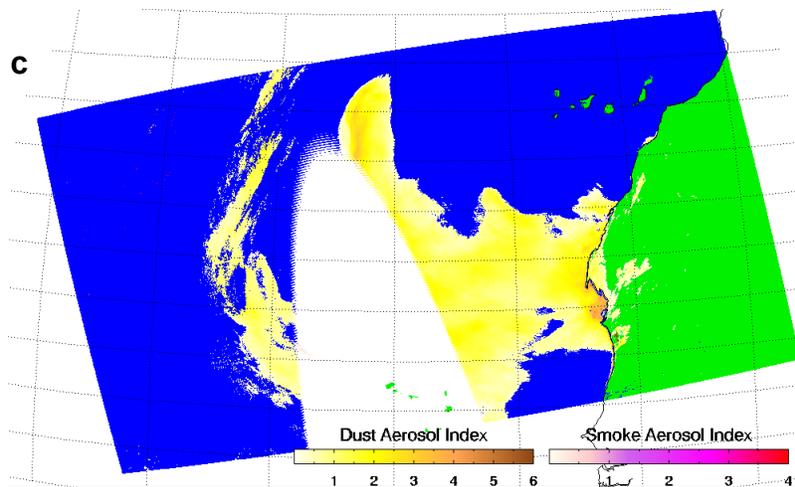
Figure 28: Comparison of dust detected (orange) using the VIIRS EPS ADP algorithm with the CALIPSO Vertical Feature Mask (VFM) on January 30, 2013, UTC 14:33. a) RGB image, b) Aerosol Optical depth from S-NPP VIIRS aerosol Product, c) Dust mask from ADP, d) Dust (orange) on CALIPSO track, e) Dust (orange) detected with VIIRS EPS ADP algorithm on CALIPSO track, f) Dust vertical distribution on the part of CALIPSO track collocated with VIIRS ADP, g) Dust from VIIRS ADP on the same part of track as in b.

The first example is shown in Figure 27 for CALIPSO VFM vs. VIIRS ADP for S-NPP VIIRS observations on January 30, 2013 at around 14:33 UTC. The dust plume is clearly visible in the RGB image (Figure 27 a). As shown in Figure 27(d), the CALIPSO VFM indicates the existence of dust over the middle part of the CALIPSO track which is collocated with S-NPP VIIRS, and the dust is seen over the coast of West Africa and close to the sunglint region. VIIRS ADP dust mask over the co-located CALIPSO track is given in Figure 27c.

CALIPSO VFM data shows that dust was dispersed between the surface and 2 km (Figure 27 g).   First, there is   good agreement between the dust plume pattern detected by ADP and the pattern shown in both RGB and VIIRS AOD (>0.2). Second, similar good agreement is also seen on the CALIPSO VFM track. It is noted that this co-located overpass is right on the edge of a sun glint region where VIIRS ADP data are not processed. Therefore, by excluding pixels in the overpass within the sun glint region and with VIIRS AOD less than 0.2, the agreement between VIIRS ADP and CALIPSO VFM for this event is 83% and 85%, respectively for Accuracy and PTPD. The definition of accuracy (and PTPD) is given shown in equation in 4.31.

Unlike the case in Figure 27, the co-located overpass shown in Figure 28 between CALIPSO and S-NPP VIIRS is over land; the agreement between VIIRS ADP and CALIPSO VFM is about 86 % and 88%, respectively for Accuracy and PTPD.
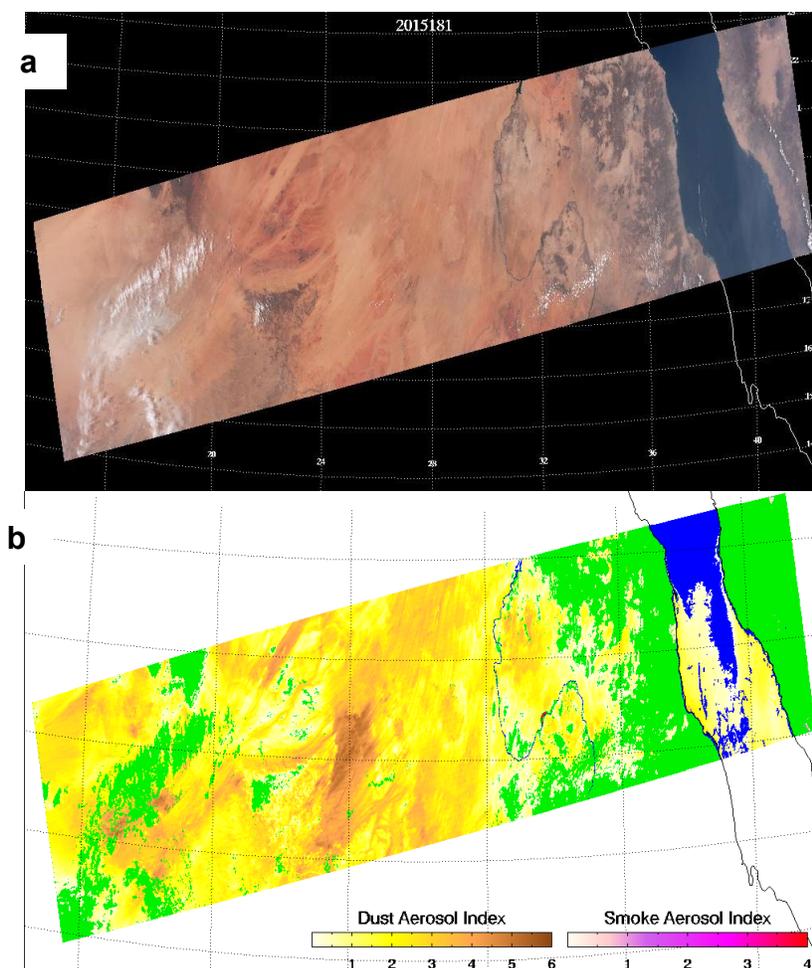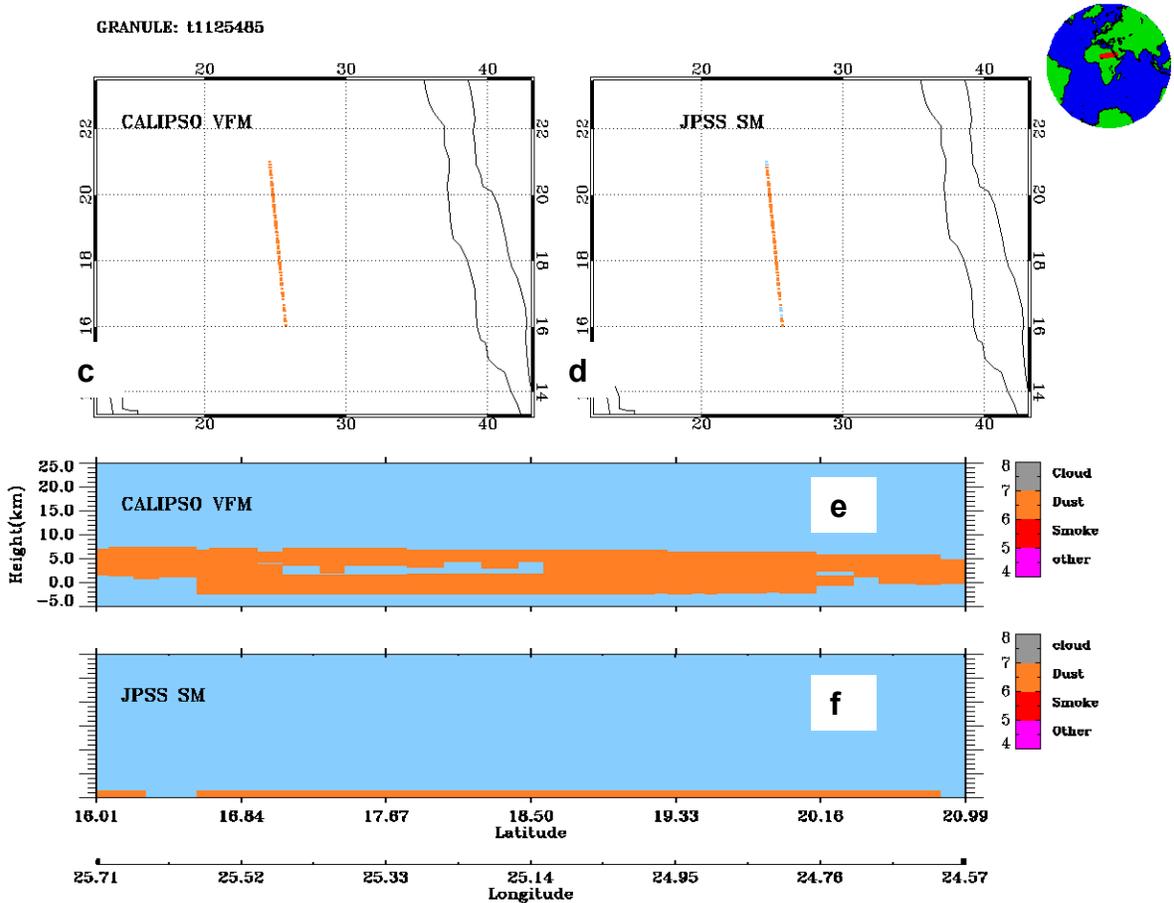
Figure 29: Comparison of dust detected (orange) using JPSS EPS ADP algorithm with dust (orange) in CALIPSO Vertical Feature Mask (VFM) on June 30, 2015 at UTC 11:25. a) S-NPP VIIRS RGB image, b) Smoke/dust mask from JPSS ADP, c) Dust (orange) on CALIPSO track, d) Dust (orange) detected with JPSS EPS ADP algorithm on CALIPSO track, e) Dust vertical distribution on the part of CALIPSO track collocated with JPSS ADP, f) Dust from VIIRS ADP on the same part of track as in b.

4.2.2 Output for Smoke Detection

4.2.2.1 Comparison with RGB imagery

Smoke is associated with fire events and the spatial distribution of smoke plumes is uniform and looks gray to a human eye compared to a cloud. This feature is useful in identifying smoke plumes in a RGB image without difficulty. Thus, RGB imagery can be used to validate ADP smoke detection. One example is shown in Figure 29 for forest fire events over the U.S. and Canada observed by S-NPP VIIRS on June 29, 2015. Qualitative comparison of smoke detection with the S-NPP VIIRS RGB image shows good agreement, especially for the thick smoke plumes over vegetated areas.
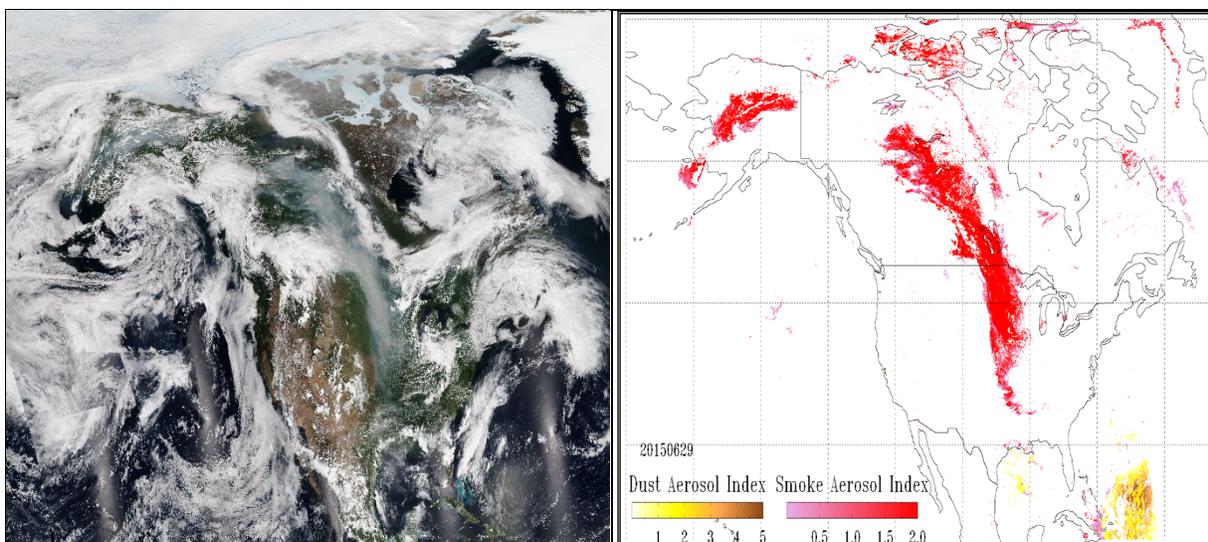
Figure 30: Left: S-NPP VIIRS RGB Image on June 29, 2015 over North America. Right: the results of the smoke detection (pixels flagged as smoky are in colored red) from JPSS ADP.

In general, the two smoke plumes, one stretching from Canada down to the Midwest in U.S. and another one over Alaska, identified by JPSS ADPs. i.e., pinkish to red color shown in the left image of Figure 29, are very consistent with the dark-gray area in the RGB image (right image in Figure 29) where the elevated smoke plumes are shown. It is also noted that patches of dust plumes, transported by crossing the Atlantic Ocean from West Africa, are also identified in JPSS ADP, i.e., yellow-brown color shown in the left image of Figure 29. Some false smoke was identified over the snow/ice edges; however, it is expected such false alarm will be eliminated after a better snow/ice mask is adopted.

4.2.2.2 Comparison with CALIPSO VFM

In Figure 30 and Figure 31, two cases of VIIRS smoke detection is shown for two different days in different years. For both examples shown, the VIIRS smoke detection mask agrees well with the MODIS RGB image and the matchups with CALIPSO tracks show that the agreement between what CALIPSO observed and what VIIRS is showing is good. In parts of the track where CALIPSO detects smoke, VIIRS identifies those pixels as clear-sky/clouds or vice-versa. It should be noted that we have not yet tested the sensitivity of our retrieval to the height of the aerosol layer and aerosol amount. Although, we can use CALIPSO to identify the height of the aerosol, we have not taken the validation efforts to the next level where we will be conducting "deep-dive" studies of individual case studies to understand the limitations of the algorithms.
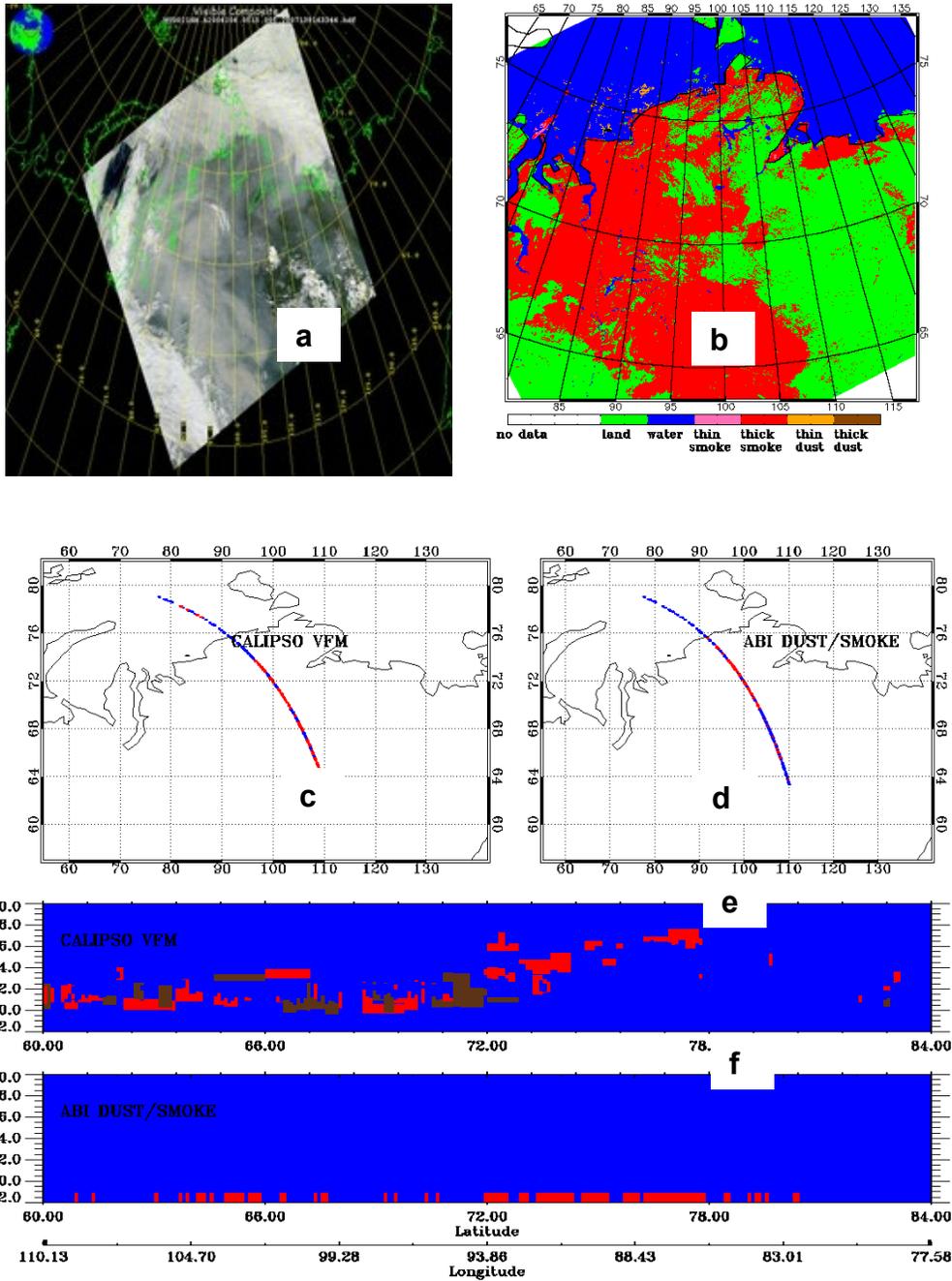
Figure 31: Comparison of smoke detected (red)) using VIIRS EPS ADP algorithm with smoke in CALIPSO Vertical Feature Mask (VFM) on July 25, 2006, UTC 05:15. a. RGB image b. Aerosol Optical depth from MODIS C5 aerosol Product. C. Smoke (red) on CALIPSO track.   d. Smoke detected with VIIRS EPS ADP algorithm on CALIPSO track. e. Smoke vertical distribution on the part of CALIPSO track collocated with VIIRS ADP d. smoke from VIIRS ADP on the same part of track as in b.
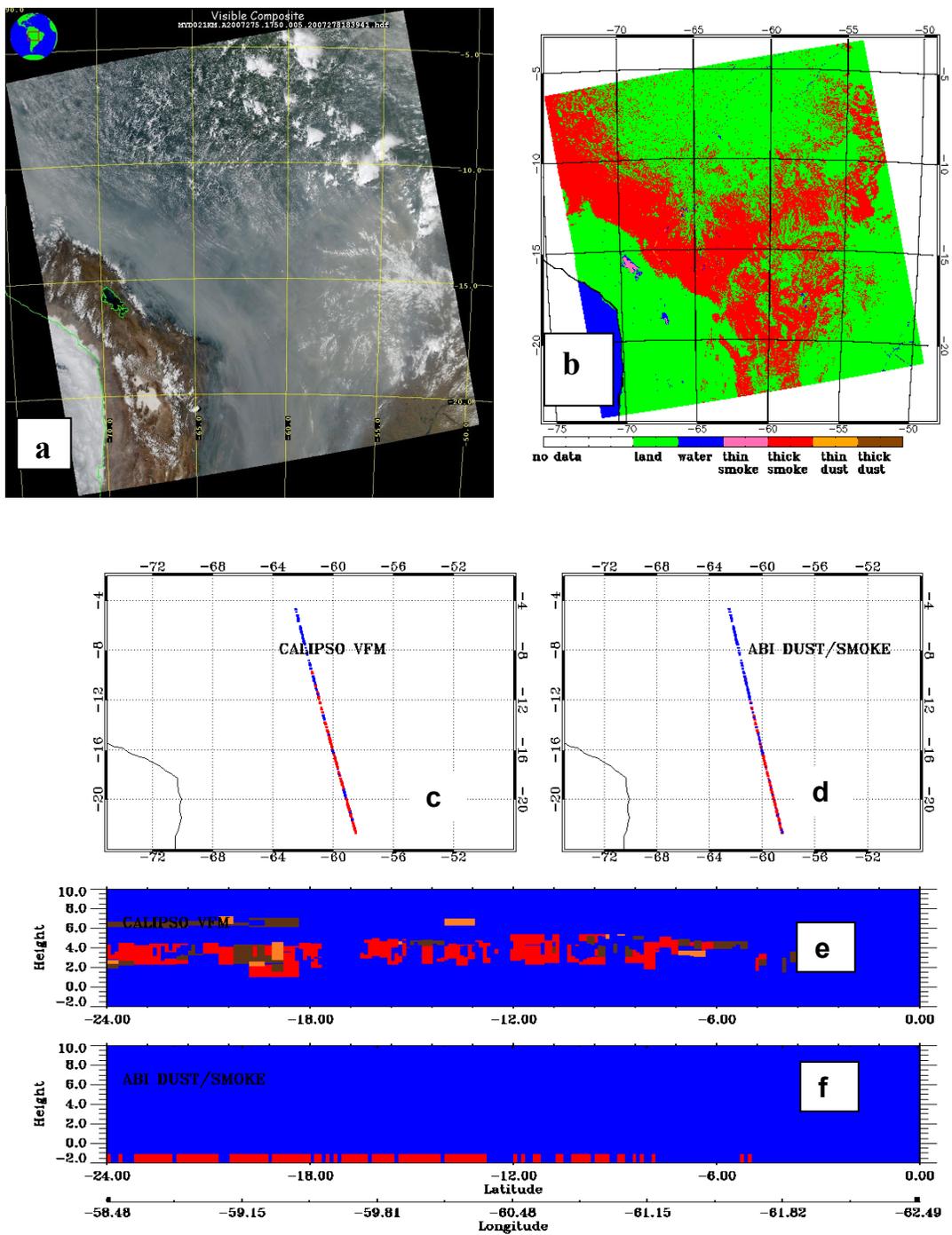
Figure 32: Comparison of smoke detected (red) using VIIRS EPS ADP algorithm with smoke in CALIPSO Vertical Feature Mask (VFM) on October 2, 2007 at 17:50 UTC. a) RGB image, b) Aerosol Optical depth from MODIS C5 aerosol Product, c) Smoke (red) on CALIPSO track, d) Smoke detected with VIIRS EPS ADP algorithm on CALIPSO track, e) Smoke vertical distribution on the part of CALIPSO track collocated with VIIRS ADP, d) smoke from VIIRS ADP on the same part of track as in b.

For smoke detection, two CALIPSO VFM vs. VIIRS ADP cases are presented. They are both over land on July 23, 2006 at 05:15 UTC and October 2, 2007 at 17:50 UTC (Figure 30and Figure 31). The agreement between the VIIRS ADP and CALIPSO VFM is 75% and 80% respectively. For a total of 22 smoke cases, the agreement between VIIRS ADP and CALIPSO VFM is about 80%.

4.2.2.3 Product Performance Evaluations

Due to lack of true ground truth for calculating accuracy estimates, the evaluation of ADP products is mainly based on the inter-comparison to other satellite-based smoke and dust products (such as RGB imagery, HMS smoke analysis, and CALIPSO VFM product) and aerosol types derived from AERONET measurements. The statistics matrix for evaluating ADP consists of three parameters. Among them, accuracy defined as the Probability of Correct Detection (PCD), is semi-quantitative and given as:

$$PCD = \frac{\text{TPD} + \text{TND}}{\text{TPD} + \text{FPD} + \text{TND} + \text{FND}} \times 100 \qquad (4.3.1)$$

In equation 4.3.1, TPD is true positive detection, TND is true negative detection, FPD is false positive detection, and FND is false negative detection. The primary validation approach will provide an overall performance of the algorithm but will not provide information on performance of the algorithm over different geographic regions. Therefore, additional spot checks and statistics will be carried out.

Because the accuracy of aerosol detection calculated using equation 4.3.1 will include true negative detections (clear sky pixels), it will not provide information on the true positive detections in which a user might be interested. Therefore, other two parameters, i.e., Probability of True Positive Detection (PTPD) and Probability of False Positive Detection (PFPD), are computed using equations 4.3.2 and 4.3.3:

$$PTPD = \frac{(TPD)}{(TPD+FND)} \times 100 \qquad (4.3.2)$$

$$PFPD = \frac{(FPD)}{(FPD+TPD)} \times 100 \qquad (4.3.3)$$

As discussed in section 4.2, two types of truth data are used for quantitative evaluations of JPSS ADP performance. One is AERONET observations and the other one is the CALIPSO VFM product. By collocating outputs from the JPSS VIIRS EPS ADP algorithm run with S-NPP VIIRS measured radiances as a proxy with these two types of truth data, statistics on accuracy, PTPD, and PFPD are calculated. The time period covers from January 1, 2013 to August 30, 2015. Details on the statics are given in the following two sections.

4.2.2.3.1　Against AERONET observations

Table 13 Accuracy, Probability of True Positive Detection, and Probability of False Positive Detection of JPSS ADP for Dust detection over AERONET Stations

Stations	Year	True positive	False positive	True negative	False negative	Accuracy (%)	PTPD (%)	PFPD (%)
Darkar	2013	63	1	106	10	93.9	86.3	0.2
	2014	74	3	45	10	90.1	88.1	0.4
Solar_Village	2013	81	26	59	30	71.4	73.0	24.3
	2014	11	4	65	5	89.4	68.8	26.7
Capo_Verde	2013	44	0	56	3	97.1	93.6	0.0
	2014	53	1	17	1	97.2	98.1	0.2

Table 14 Accuracy, Probability of True Positive Detection, and Probability of False Positive Detection of JPSS ADP for smoke detection over AERONET Stations

Stations (Biomass –burning)	True positive	False positive	True negative	False negative	Accuracy (%)	PTPD (%)	POFD (%)
Alta_Floresta	10	0	178	0	100.0	100.0	0.0
Bonanza_Creek	1	0	48	0	100.0	100.0	0.0
Jabiru	1	0	313	0	100.0	100.0	0.0
Moscow_MSU_MO	16	2	92	1	97.2	94.1	11.0
Tomsk_22	17	1	83	0	99.0	100.0	5.0
Yakutsk	22	1	88	1	98.2	95.6	4.3

Table 13 and Table 14 are the results of comparisons of JPSS ADP with AERONET Observations, respectively for smoke and dust, over stations with the corresponding prevailing aerosol type. It is clearly seen that, for dust prevailing stations (as shown in Table 13), the accuracy varies from 70 to 97%, PTPD is in the range from 73 to 98%, and PFPD can reach up to 27%. For smoke prevailing stations (as shown in Table 14), the number of true positive events is a lot smaller compared with dust, so accuracy, PTPD and PFPD are respectively about 97~100%, 94~100% and 0~11%.

To evaluate the overall performance of the JPSS ADP algorithm, ensemble values for accuracy, PTPD and PFPD were calculated with matchups between ADPs with observations over all the available AERONET stations during the 2.5 year. time period (about 400 stations). The results are given in Table 15. It is seen that the ensemble value of Accuracy (i.e., Probably of Correct Detection), POPD and PFPD is 99%, 70% and 21% for dust and 97%, 92% and 11% for smoke.

Therefore, based on these validation results, the JPSS VIIRS ADP meets the mission requirement as shown in Table 1.

Table 15 Ensemble Accuracy, Probability of True Positive Detection, and Probability of False Positive Detection of JPSS ADP for smoke and dust detection

Type	True positive	False positive	True negative	False negative	Accuracy	PTPD	PFPD
Dust	2028	549	149897	882	99.0	69.7	21.3
smoke	9324	1214	60397	799	97.2	92.1	11.5

4.2.2.3.2 Against CALIPSO VFM product

Performance evaluations of JPSS ADP were also carried out by comparing to the CALIPSO VFM product. The global coverage of CALIPSO VFM allows us to stratify the evaluation according to land type, i.e., over land and over water. The results for over land and over water are given respectively in Table 16 and Table 17.

It is seen that, for dust detection, the Accuracy and PTPD are 84 and 80% over land, while they can reach up 96 and 95% respectively, indicating more accurate dust detection can be obtained over water than over land. This is consistent with the results shown in Section 3.4.1., i.e., the surface reflectance is much smaller and more uniform over water than over land. As for smoke detection, the accuracy and PTPD are very similar over land and over water. They are about 99% and 95% over land and 94% and 97% over water. In addition, it is clear that PFPD for smoke detection is much larger than that for dust detection. PFPD for smoke detection can reach up to 45%, while it is less than 5% for smoke detection.

In general, comparisons with CALIPSO VFM products indicate that JPSS ADP meets the mission requirements as shown in Table 1.

Table 16. Accuracy, Probability of True Positive Detection, and Probability of False Positive Detection of JPSS ADP for smoke and dust detection over land

Type	True positive	False positive	True negative	False Negative	Accuracy (%)	PTPD (%)	PFPD (%)
DUST	10669	170	5676	2840	84.4	80.0	1.6
SMOKE	307	159	19534	14	99.1	96.7	34.1

Table 17. Accuracy, Probability of True Positive Detection, and Probability of False Positive Detection of JPSS ADP for smoke and detection over water

Type	True positive	False positive	True negative	False negative	Accuracy (%)	PTPD (%)	PFPD (%)
DUST	297	11	139	10	95.4	96.4	3.3
SMOKE	601	507	7605	15	94.0	97.5	45.7

4.3 Framework run and validation

4.3.1 Framework run

As shown in section 4.1, the EPS ADP algorithm was validated extensively. However, this validation work was done with offline runs, i.e., running the EPS ADP algorithm without integrating it into the JPSS Risk Reduction VIIRS product framework. Under the operational environment, the EPS ADP algorithm will be running in the framework. In general, the procedure for running the EPS ADP algorithm in the framework is as follows: first, common input radiance data are generated from a proxy data set; the common dataset includes both the required input and ancillary data in a common data format, i.e., netCDF. Second, the aerosol detection algorithm is called according to the order of precedence. Finally, results from each product are written to an output file in netCDF format.

4.3.2 Consistency tests with S-NPP VIIRS granules

To test the offline runs with runs through integration of the EPS ADP algorithm into the framework, comparisons were made between outputs from the offline run with outputs from the framework run

with common input data and using the EPS ADP algorithm. For the tests shown below, S-NPP VIIRS observations from several granules were used as proxy for JPSS VIIRS, i.e., 750 m radiances from S-NPP VIIRS bands corresponding to JPSS VIIRS channels required by the EPS ADP algorithm and the cloud mask from the S-NPP VIIRS cloud mask product. Figure 32 and Figure 33 show the comparisons of the offline smoke/dust mask with those from the framework run for two cases, one for a smoke event and one for a dust outbreak. It is seen that the Framework runs were able to reproduce the same results as those from offline run for both cases, with an agreement of about 99.5%.
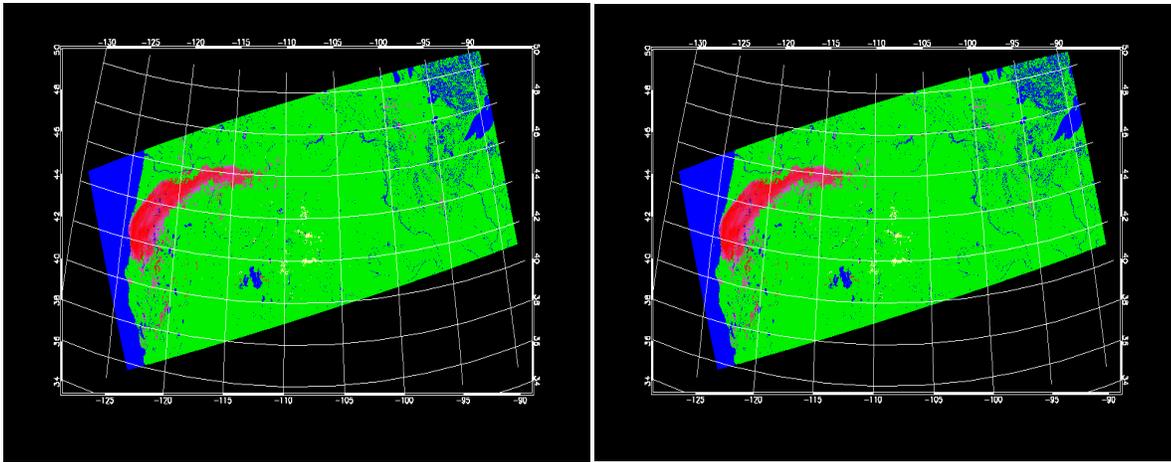
Figure 33: Comparison of offline run with framework run for S-NPP VIIRS observation on August 3, 2014, UTC13:20. a) smoke/dust mask from framework run, b) smoke/dust mask from offline run.
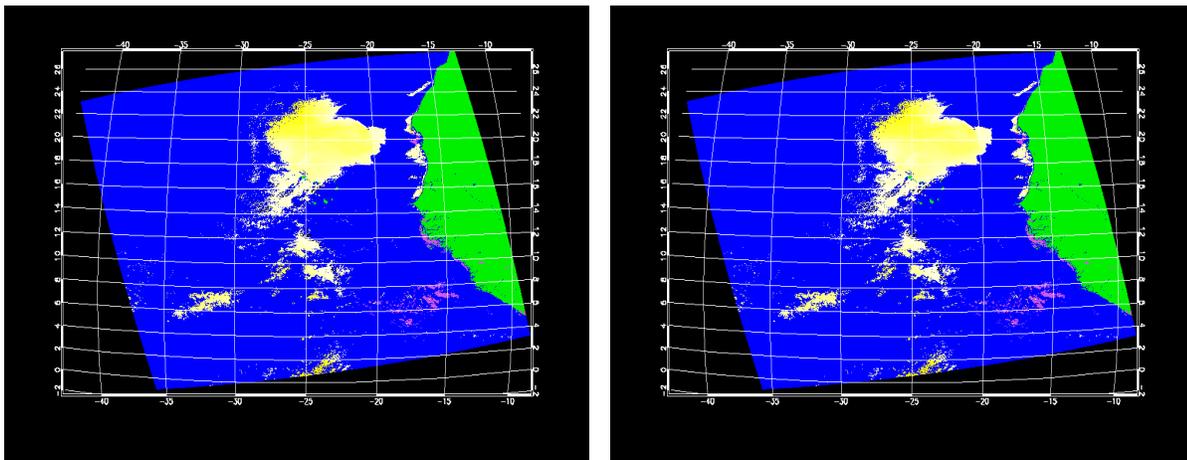
Figure 34: Comparison of offline run with framework run form S-NPP VIIRS observation on February 13, 2014, UTC 03:25. a) smoke/dust mask from framework run, b) smoke/dust mask from offline run.

4.3.3 Results from Framework run with global S-NPP VIIRS observation

To further test the framework run, global S-NPP VIIRS observations for July 15, 2014 and July 16, 2014 were selected as proxy input to run the EPS ADP algorithm in the framework. Figure 34a and b show

the global smoke/dust mask product from the framework run of the EPS ADP algorithm for these two consecutive days. For the purpose of comparison, OMPS Absorbing Aerosol Indexes for the corresponding two consecutive days are also shown in Figure 34b and c. In general, the framework run produced no abnormal smoke or dust patterns for each of these two days, and consistency is seen between results from these two consecutive days. Furthermore, large smoke plumes resulting from biomass burning were identified over North America and Russia, and dust from dust storms are shown over the Sahara Desert. Although the locations of the dust and smoke plumes are consistent between the two days, there are differences in the amount of smoke and dust present. This is very typical because while old fires die out, new fires form and dust transport occurs in the free troposphere moving it long distances over short time periods. In addition, the smoke/dust mask produced by ADP from the framework run has as pattern very similar to that of the OMPS Absorbing Aerosol Index (shown in Figure 34b and c), which is an indication of the presence of smoke/dust using UV observations, even though it cannot differentiate between smoke and dust.
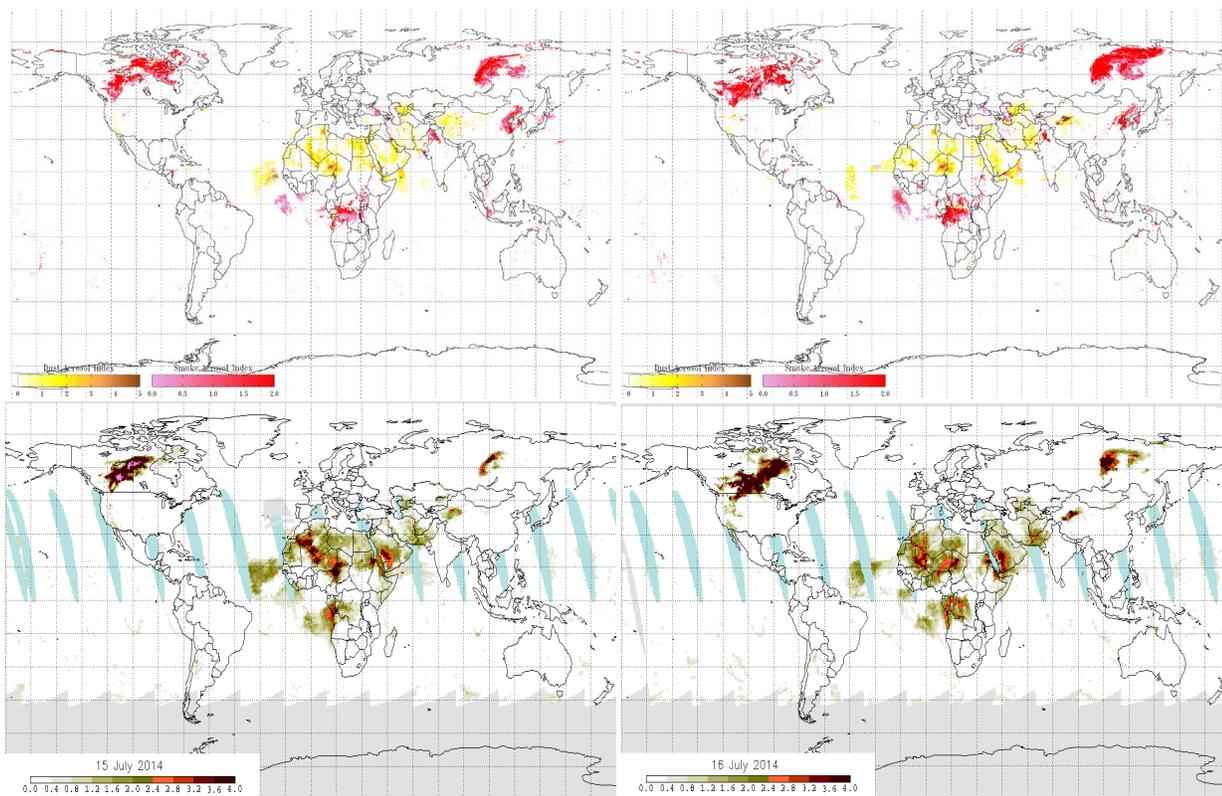

Figure 35: Global smoke/dust mask from EPS ADP algorithm run in the framework for S-NPP VIIRS observations. a) July 15, 2014, b) July 16, 2014. Absorbing Aerosol Indexes from OMPS for these two days are also shown in c) and d).

5 PRACTICAL CONSIDERATIONS

5.1 Numerical Computation Considerations

The EPS ADP algorithm is implemented sequentially. Because some tests require ancillary data, the ancillary data (e.g., day/night, snow/ice, sun glint, and cloud/clear) need to be input first. To balance the efficiency and memory requirements for the full disk processing, a block of scanning pixels are read into a RAM buffer together instead of reading data pixel by pixel.

5.2 Programming and Procedural Considerations

The ADP algorithm requires knowledge of spatial uniformity metrics that are computed for each pixel using pixels that surround it. Detection is performed separately for land and water.

In addition, future temporal tests require information from the previous image. Beyond this reliance, the ADP algorithm is a pixel by pixel algorithm.

5.3 Quality Assessment and Diagnostics

The following procedures are recommended for diagnosing the performance of the ADP algorithm.
- Monitor the percentage of pixels falling into each ADP aerosol bin values. These values should be quasi-constant over a large area.
- Monitor the frequency of false positives in regions to assess the need to have region specific thresholds developed and implemented.
- Periodically image the individual test results to look for artifacts or non-physical behaviors.
- Monitor retrievals over different surface (geographic) types for dependency of errors on surface brightness.
- Monitor spectral threshold values and provide a quality flag depending on how close the tests used in the EPS ADP algorithm are to specified thresholds.
- Monitor retrievals for temporal consistency. Are retrievals consistent from image to image?

A qualify flag with a value of 0/1/2 representing high/medium/low confidence is generated according to how far the actual value for each test is from the predefined threshold.

5.4 Exception Handling

The quality control flags for VIIRS ADP will be checked and inherited from the flagged Level 1b sensor input data, including bad sensor input data, missing sensor input data and validity of each channel used; and will also be checked and inherited from the VIIRS cloud mask at each pixel.

The ADP algorithm also expects the Level 1b processing to flag any pixels with missing geolocation or viewing geometry information.

The ADP algorithm does check for conditions where the ADP algorithm cannot be performed and generates quality control flags for snow/ice pixel, pixels with saturated channels; pixels missed geolocation or viewing geometry information.

5.5 Algorithm Validation

For pre-launch validation, the EPS ADP algorithm will be extensively validated by using S-NPP VIIRS RGB images, S-NPP VIIRS aerosol products, AERONET observations, and Vertical Feature Mask from CALIPSO. For post-launch validation, besides the above-mentioned approach, field campaigns will also be carried out. Details on Algorithm Validation are given separately in the VIIRS EPS ADP algorithm testing and validation plan document.

6 ASSUMPTIONS AND LIMITATIONS

The following assumptions have been made in the current algorithm:
- Calibrated and geo-located radiances in VIIRS channels as required by the VIIRS EPS ADP algorithm as shown in Table 2 are available
- VIIRS cloud mask is available and is adequate for the purpose of EPS ADP algorithm
- All the ancillary data are available.

Limitations applying to current algorithm are:
- Only for daytime
- Smoke detection over land is limited to dark surface
- Not optimal for optically thin smoke and dust
- No testing has been done to determine algorithm limitations if smoke and dust or other types of aerosols co-exist in the same pixel

6.1 Performance

The following assumptions are made in estimating the performance of EPS ADP algorithm:
- smoke/dust mask from CALIPSO VFM represents the truth;
- visual separation of smoke, dust and clear pixels from S-NPP VIIRS RGB image introduces negligible error;
- Thresholds used in the current algorithm are tailored for S-NPP VIIRS channel specifications. Post–launch tuning of these thresholds will not affect the estimate of algorithm performance.
- In case of VIIRS sensor degradation, product production might squeeze but studies will be carried out prior to the launch on the extent of the effect any changes to instrument characteristics will have on product quality.

6.2 Assumed Sensor Performance

The VIIRS EPS ADP algorithm assumes the sensor will meet its current specifications and produce calibrated quality radiance in the required channels (see Table 2). As shown in section 3.4.1., impacts from instrument noise and calibration error can be mitigated by adjusting threshold accordingly. However, the EPS ADP algorithm has low tolerance on missing channels. As discussed in the above sections, the EPS ADP algorithm selects the optimal channels or combination of channels to best separate the signal of smoke/dust from others. Therefore, any missing channels will definitely downgrade the performance of the algorithm and eventually lead to failure if crucial channels are missing.

In addition, the EPS ADP algorithm will be dependent on the following instrumental characteristics.

- The spatial uniformity tests in ADP will be critically dependent on the amount of striping in the data.
- Errors in navigation from image to image will affect the performance of the temporal tests.

7 Pre-Planned Product Improvement

7.1 Improvement 1

The spectral screening thresholds are currently not a function of viewing and solar geometry. Testing will be carried out to understand the dependencies of some of the smoke/dust tests on viewing and solar geometries. Additional testing will also be done using observations to determine VIIRS spectral thresholds and how robust these spectral thresholds are under different scenarios. Based on these tests, the algorithm could be improved.

7.2 Improvement 2

Validation of smoke/dust detection still remains a challenge at this stage. Besides the validation exercises that have already been completed, additional validation will be carried out. They include comparisons with the ground-based measurements and other satellite products. Validation with ground-based measurements will take advantage of measurements from aerosol samplers in the IMPROVE network and Angstrom exponent information from AERONET for any indications of smoke/dust particles in local and regional events. This, however, is not a direct comparison but an indirect subjective evaluation of the ADP smoke/dust product. For comparisons with other satellite products, the Aerosol Index from OMI will be fully used to quantify the accuracy of smoke/dust products.

8 REFERENCES

Ackerman, S. A., Using the radiative temperature difference at 3.7 and 11mm to track dust outbreaks, *Remote Sensing of Environment*, **27**: (2) 129-133, 1989.

Ackerman, S. A., and K. I. Strabala, Satellite remote sensing of H_2SO_4 aerosol using the 8-12μm window region: Application to Mount Pinatubo. *J. Geophys. Res.*, **99**, 18,639-18,649, 1994.

Ackerman, S. A., Remote sensing aerosols using satellite infrared observations. *J. Geophys., Res.*, **102**, 17069–17079, 1997.

Ackerman, Steven A.; Strabala, Kathleen I.; Menzel, W. Paul; Frey, Richard A.; Moeller, Christopher C. and Gumley, Liam E., Discriminating clear sky from clouds with MODIS, *J. Geophys. Res.*, **103**, 32,141-32,157, 1998.

Ackerman, S. A., R. E. Holz, R. Frey, E. W. Eloranta, B. Maddux, and M. McGill, Cloud Detection with MODIS: Part II Validation. Accepted with revision to *J. Tech.*, 2008.

Al-Saadi, J., et al., Improving national air quality forecasts with weather satellite aerosol observations, Bull. Am. Meteorol. Soc., 86, 1249– 1261, 2005

Ashpole, I.*, and* R. Washington *(*2012*),* An automated dust detection using SEVIRI: A multiyear climatology of summertime dustiness in the central and Western Sahara*,* J. Geophys. Res.*,* 117*, D08202, doi:10.1029/2011JD016845.*

Barton, I. J., A. J. Prata, I. G. Watterson and S. A. Young, Identification of the Mount Hudson volcanic cloud over SE Australia. *Geophy. Res. Lett.,* **19**(12), June 19, 1992, 1211-1214, 1992.

Bohren, C. F. and D. R. Huffman, "Absorption and scattering of light by small particles", Wiley, New York, 1983.

Burton, S. P.; Ferrare, R. A.; Vaughan, M. A.; Omar, A. H.; Rogers, R. R.; Hostetler, C. A.; Hair, J. W. (2013) , Aerosol classification from airborne HSRL and comparisons with the CALIPSO vertical feature mask, *Atmospheric Measurement Techniques Discussions*; Vol. 6 Issue 1, p1815.

Bullard, J. E., Baddock, M. C., McTainsh, G. H., & Leys, J. F. (2008). Sub-basin scale dust source geomorphology detected using MODIS. Geophysical Research Letters, 35 (15), L15404. doi:10.1029/2008GL033928.

Cho, H.-M., S. L. Nasiri, P. Yang, I. Laszlo, X. Zhao (2013), Detection of optically thin mineral dust aerosol layers over the ocean using MODIS. *J. Atmos. Ocean Tech.*, **30**, p. 896-916.

Ciren, Pubu and Kondragunta, Shobha, Dust aerosol index (DAI) algorithm for MODIS, Journal of Geophysical Research-Atmospheres Volume: 119 Issue: 8 Pages: 4770-4792, 2014. DOI: 10.1002/2013JD020855

Darmenov, A., and I. N. Sokolik (2005), Identifying the regional thermal-IR radiative signature of mineral dust with MODIS, Geophys. Res. Lett., 32, L16803, doi:10.1029/2005GL023092.

Darmenov, A., and I. N. Sokolik (2009), spatial variability of satellite visible radiances in dust and dust-cloud mixed conditions: Implications for dust detection, Geophys. Res. Lett., 36, L14811, doi:10.1029/2009GL038383.

Dubovik, O., Holben, B., Eck, T. F., Smirnov, A., Kaufman, Y. J., King, M. D., et al. (2002), Variability of absorption and optical properties of key aerosol types observed in worldwide locations. Journal of the Atmospheric Sciences, 59, 590–608.

Dubovik, O., et al. (2006), Application of light scattering by spheroids for accounting for particle nonsphericity in remote sensing of desert dust, J. Geophys. Res., 111, D11208, doi:10.1029/2005JD006619.

Dunion, J.P. and Velden, C.S., The Impact of the Saharan Air Layer on Atlantic Tropical Cyclone Activity, *Bulletin of the American Meteorological Society*, **90**, 353–365, 2004.

Eck, T. F*., B. N. Holben, J. S. Reid, O. Dubovik, A. Smirnov, N. T. O'Neill, I. Slutsker, and* S. Kinne *(*1999*)*, Wavelength dependence of the optical depth of biomass burning, urban, and desert dust aerosols*,* J. Geophys. Res*.,* 104*(*D24*),* 31333–31349*, doi:*10.1029/1999JD900923*.*

Evan, A. T., A. K. Heidinger, and M. J. Pavolonis (2006), Development of a new over-water advanced very high resolution radiometer dust detection algorithm, Int. J. Remote Sens., 27, 3903 – 3924, doi:10.1080/01431160600646359.

Frey, R. A., S. A. Ackerman, Y. Liu, K. I. Strabala, H. Zhang, J. R. Key, and X. Wang, Cloud detection with MODIS, Part I: Improvements in the MODIS cloud mask for collection 5. *Journal of Atmospheric and Wateric Technology*, **25**, 7, 1057-1072, 2008.

Hansell R.A., S.C. Ou, K.N. Liou, J.K. Roskovensky, S.C. Tsay, C. Hsu, and Q. Ji (2007), Simultaneous Detection/Separation of Mineral Dust and Cirrus Clouds Using MODIS Thermal Infrared Window Data, Geophys. Res. Lett, 34, L13802, doi:10.1029/2007GLO31035.

Herman, J. R., P. K. Bhartia, O. Torres, N. C. Hsu, C. J. Seftor, and E. Celarier (1997), Global distribution of UV-absorbing aerosols from Nimbus 7/TOMS data, J. Geophys. Res., 102, 16,911-16,921.

Holben B.N., T.F. Eck, I. Slutsker, D. Tanré, J.P. Buis, A. Setzer, E. Vermote, J.A. Reagan, Y. Kaufman, T. Nakajima, F. Lavenu, I. Jankowiak, and A. Smirnov, 1998: AERONET - A federated instrument network and data archive for aerosol characterization, Rem. Sens. Environ., 66, 1-16.

Holben, B.N., Tanré, D., Smirnov, A., Eck, T.F., Slutsker, I., Abuhassan, N., Newcomb, W.W., Schafer, J.S., Chatenet, B., Lavenu, F., Kaufman, Y.J., Castle, J.V., Setzer, A., Markham, B., Clark, D., Frouin, R., Halthore, R., Karneli, A., O'Neill, N.T., Pietras, C., Pinker, R.T., Voss, K. and Zibordi, G. (2001). An emerging ground-based aerosol climatology: Aerosol optical depth from AERONET. Journal of Geophysical Research 106: doi: 10.1029/2001JD900014. issn: 0148-0227.

Hsu, N. C*., J. R. Herman, O. Torres, B. N. Holben, D. Tanre, T. F. Eck, A. Smirnov, B. Chatenet, and* F. Lavenu *(*1999*),* Comparisons of the TOMS aerosol index with Sun-photometer aerosol optical thickness: Results and applications*,* J. Geophys. Res*.,* 104*(*D6*),* 6269–6279*, doi:*10.1029/1998JD200086*.*

Hsu N.C., W. D. Robinson, S. W. Bailey, and P. J. Werdell (2000). The description of the SeaWiFS absorbing aerosol index *SeaWiFS NASA Technical Memorandum 2000-206892, 10*, 3-5

Hsu, N.C., S.-C. Tsay, M. D. King, and J. R. Herman (2004), Aerosol *properties over bright reflecting source regions*, IEEE Trans. Geosci. Remote Sens., 42 (3), 557-569, doi: 10.1109/TGRS.2004.824067.

Hsu, N.C., S.-C. Tsay, M. D. King, and J. R. Herman (2006), Deep Blue *retrievals of Asian* aerosol *properties during ACE-Asia*, IEEE Trans. Geosci. Remote Sens., 44 (11), 3180-3195, doi: 10.1109/TGRS.2006.879540.

Hu, X. Q., Lu, N. M., Niu, T., and Zhang, P. (2008), Operational retrieval of Asian sand and dust storm from FY-2C geostationary meteorological satellite and its application to real time forecast in Asia, Atmos. Chem. Phys., 8, 1649–1659.

IPCC, 2007: Climate Change 2007: The Physical Science Basis. Contribution of Working Group I to the Fourth Assessment Report of the Intergovernmental Panel on Climate Change [Solomon, S., D. Qin, M. Manning, Z. Chen, M. Marquis, K.B. Averyt, M.Tignor and H.L. Miller (eds.)]. Cambridge University Press, Cambridge, United Kingdom and New York, NY, USA.

Jankowiak, I., D. Tanré (1992), Satellite Climatology of Saharan Dust Outbreaks: Method and Preliminary Results. *J. Climate*, **5**, 646–656.

Kaufman, Y. J., et al., Operational remote sensing of tropospheric aerosol over land from EOS moderate resolution imaging spectroradiometer, *J. Geophys. Res.*, **102**, 16,971-16,988, 1997.

Kaufman, Y. J. , D. Tanré, L. Remer, E. Vermote, A. Chu, and B. N. Holben (1997), Remote sensing of tropospheric aerosol from EOS-MODIS over the land using dark targets and dynamic aerosol models, JGR-Atmosphere, special issue on Remote Sensing of Aerosol and Atmospheric Corrections, 102,17051-17067.

Kaufman, Y. J., Arnon Karnieli, Didier Tanré (2000), Detection of dust over deserts using satellite data in the solar wavelengths. IEEE T. Geoscience and Remote Sensing (TGRS) 38(1):525-531.

Kim, K. M., Lau, W. K.-M., Sud, Y. C., and Walker, G. K. (2010), Influence of aerosol-radiative forcings on the diurnal and seasonal cycles of rainfall over West Africa and Eastern Atlantic Ocean using GCM simulations, Clim. Dynam., 26, doi:10.1007/s00382-010-0750-1.

King, M. D., Menzel, W. Paul, Y. Kaufmann, Didier T., B.-C. Gao, S. Platnick, S. Ackerman, L. Remer, R. Pincus, and P. A. Hubanks, Cloud and aerosol properties, precipitable water, and profiles of temperature and water vapor from MODIS. *IEEE Transactions on Geoscience and Remote Sensing*, **41**, 442-458, 2003.

Klüser, L., and K. Schepanski (2009), Remote sensing of mineral dust over land with MSG infrared channels: A new Bitemporal Mineral Dust index, Remote Sens. Environ., 113, 1853–1867, doi:10.1016/j.rse.2009.04.012.

Kotchenova, S.Y., E.F. Vermote, R. Matarrese, & F.J. Klemm, Jr. (2006), Validation of a vector version of the 6S radiative transfer code for atmospheric correction of satellite data. Part I: Path Radiance, Applied Optics, 45(26), 6726-6774.

Kwiatkowska, E. J. , Bryan A. Franz, Gerhard Meister, Charles R. McClain, and Xiaoxiong Xiong (2008), Cross calibration of ocean-color bands from Moderate Resolution Imaging Spectroradiometer on Terra platform, Applied Optics, Vol. 47, Issue 36, pp. 6796-6810.

Legrand, M., G. Cautenet, and J.-C. Buriez, Thermal impact of Saharan dust over land, Part II: application to satellite IR remote sensing, *J. Appl. Meteorol.*, **31**, 181-193, 1992.

Legrand, M., A. Plana-Fattori, and C. N'Doume, Satellite detection of dust using IR imagery of Meteosat 1. Infrared difference dust index, *J. Geophys. Res.*, **106**, 18,251-18,274, 2001.

Liu, Z., et al. (2008), CALIPSO lidar observations of the optical properties of Saharan dust: A case study of long-range transport, *J. Geophys. Res.*, 113, D07207, doi:10.1029/2007JD008878.

Liu, Z., M. A. Vaughan, D. M. Winker, C. Kittaka, R. E. Kuehn, B. J. Getzewich, C. R. Trepte, and C. A. Hostetler, 2009: The CALIPSO lidar cloud and aerosol discrimination: Version 2 algorithm and initial assessment of performance. J. Atmos. Oceanic Technol., 26, 1198–1213.

Nicholson, S. E. (2000), Land surface processes and Sahel climate, Rev. Geophys., 38, 117–139.

Martins, J.V., D. Tanré, L. Remer, Y. Kaufman, S. Mattoo, R. Levy (2002), *MODIS Cloud screening for remote sensing of aerosol over oceans using spatial variability.* Geophys. Res. Lett.,29(12),10.1029/2001GL013252.

Mielonen, T., Arola, A., Komppula, M., Kukkonen, J., Koskinen, J., de Leeuw, G., and Lehtinen, K. E. J. (2009), Comparison of CALIOP level 2 aerosol subtypes to aerosol types derived from AERONET inversion data, Geophys. Res. Lett., 36, L18804, doi:10.1029/2009gl039609.

Miller, S. D. (2003), A consolidated technique for enhancing desert dust storms with MODIS, Geophys. Res. Lett., 30(20), 2071, doi:10.1029/2003GL018279.

Platnick,   S., M. King, S. A. Ackerman, P. W. Menzel, B. A. Baum, J. C. Riédi, R. A. Frey, The MODIS Cloud Products: Algorithms and Examples from Terra, *IEEE Transactions on Geoscience and Remote Sensing*, **41**, 459-???, 2003

Prata, A. J., Observations of volcanic ash clouds in the 10-12-MU-M window using AVHRR/2 data. *International Journal of Remote Sensing* **10**(4-5), 751-761, 1989.

Prospero, J. M. and Lamb, P. J.(2003), African droughts and dust transport to the Caribbean: Climate change implications, Science, 302, 1024–1027.

Rember, L., Y. J. Kaufman, D. Tanré, D., S. Mattoo, D. A. Chu, J. V. Martins, R-R. Li, C. Ichoku, R. C. Levy, R. G. Kleidman, T. F. Eck, E. Vermote, and B. N. Holben, The MODIS aerosol algorithm, products, and validation. *J. Atmos. Sci.*, **62**, 947–973, 2005.

Remer, L. A., D. Tanre, Y.J. Kaufman, R. Levy and S. Mattoo, Algorithm for Remote Sensing of Tropospheric aerosol from MODIS: Collection 5, Product ID MOD04/MYD04, 2006.

Ramirez-Beltran, ND., R. Kuligowski and E. Harmsen (2008),Validation and Strategies to Improve the Hydro-Estimator and NEXRAD over Puerto Rico, 12th WSEAS International Conference on SYSTEMS, Heraklion, Greece, July 22-24.

Schepanski, K., Tegen, I., Laurent, B., Heinold, B., & Macke, A. (2007), A new Saharan dust source activation frequency map derived from MSG–SEVIRI IR-channels. Geophysical Research Letters, 34, L18803. doi:10.1029/2007GL030168.

Smirnov, A., BN Holben, TF Eck, O Dubovik, I Slutsker (2000), Cloud-screening and quality control algorithms for the AERONET database, Remote Sensing of Environment,   73 (3), 337-349

Sokolik, I. N. (2002), The spectral radiative signature of wind-blown mineral dust: Implications for remote sensing in the thermal IR region, Geophys. Res. Lett., 29(24), 2154, doi:10.1029/2002GL015910.

Tan, S.-C., G.-Y. Shi, J.-H. Shi, H.-W. Gao, and X. Yao (2011), Correlation of Asian dust with chlorophyll and primary productivity in the coastal seas of China during the period from 1998 to 2008, *J. Geophys. Res.*, 116, G02029, doi:10.1029/2010JG001456.

Tanre, D., and M. Legrand, On the Satellite Retrieval of Saharan Dust Optical Thickness Over Land: Two Different Approaches, *J. Geophys. Res.*, **96**, 5221–5227, 1991.

Torres, O., Bhartia, P.K., Herman, J.R., Sinyuk, A. (2002), "Aerosol properties *from* EP-TOMS near UV observations", Adv Space Res., 29, 1771-1780.

Vaughan, M., and Coauthors, 2009: Fully automated detection of cloud and aerosol layers in the CALIPSO lidar measurements. J. Atmos. Oceanic Technol., 26,2034–2050Wilks, D.S. (1995), Statistical Methods in the Atmospheric Sciences: An Introduction. Academic Press, San Diego, 467 pp.

Verge-Depre, G., M. Legrand, C. Moulin, A. Alias, and P. Francois, Improvement of the detection of desert dust over the Sahel using METEOSAT IR imagery, *Ann. Geophys.,* **24**, 2065-2073, 2006.

Winker, D. M., M. A. Vaughan, A. Omar, Y. X. Hu, K. A. Powell, Z. Y. Liu, W. H. Hunt, and S. A. Young (2009), Overview of the CALIPSO mission and CALIOP data processing algorithms, J. Atmos. Oceanic Technol., 26, 2310–2323, doi:10.1175/2009JTECHA1281.1.

Winker, D. M., et al. (2010), The CALIPSO mission: A global 3D view of aerosols and clouds, Bull. Am. Meteorol. Soc.,91, 1211–1229, doi:10.1175/2010BAMS3009.

Xie, Y., (2009), Detection of smoke and dust aerosols using Multi-Sensor Satellite remote sensing measurements. Department of Geography and Geoinformation Science, George Manson University, Doctor of Philosphy.

Yoshioka, M. and Mahowald, N. M. (2007), Impact of desert dust radiative forcing on Sahel precipitation: Relative importance of dust compared to sea surface temperature variations, vegetation changes, and greenhouse gas warming, J. Climate, 20, 1445–1467.

Zhao, C., Liu, X., Ruby Leung, L., and Hagos, S. (2011), Radiative impact of mineral dust on monsoon precipitation variability over West Africa, Atmos. Chem. Phys., 11, 1879–1893, doi:10.5194/acp-11-1879-2011.

Zhao, T. X.-P., S. Ackerman, and W. Guo (2010), Dust and smoke detection for multi-channel imagers. Remote Sens., 2, 2347–2368, doi:10.3390/rs2102347.